UNIVERSITÀ DEGLI STUDI DI PADOVA
Sede Amministrativa: Università degli Studi di Padova
Dipartimento di Fisica "G.Galilei"
Via Marzolo, 8 35131 Padova

SCUOLA DI DOTTORATO DI RICERCA IN FISICA
CICLO XXII

SPECTRAL AND TIMING PROPERTIES OF TRANSIENT ANOMALOUS X-RAY PULSARS

Direttore della Scuola: **Ch.mo Prof. Attilio Stella**
Supervisor: **Ch.mo Prof. Roberto Turolla**
Co-supervisor: **Ch.mo Prof. Gian Luca Israel**

Dottoranda: **Dott. Alessandra Albano**

Ai miei genitori e a Mario

Contents

Preface

In the last years, thanks to new generation satellites (mostly *Chandra* and *XMM-Newton*), an increasing number of high resolution spectral and timing observations of X-ray emitting isolated neutron stars (INS) has become available. Several new classes of X-ray emitting INSs have been discovered, all of them radio silent or with radio properties much at variance with those of Pulsar Radio (PSRs): X-ray Dim Isolated Neutron Stars (XDINSs), Anomalous X-ray Pulsars (AXPs) and Soft Gamma-ray Repeaters (SGRs), Central Compact Objects (CCOs), Rotating Radio Transient (RRATs, in one case).
AXPs and SGRs represent two peculiar groups of INSs, totalling 15 objects (6 SGRs and 9 AXPs plus one candidate). Although much less noumerous than PSRs, these objects have been extensively studied because of their peculiar and extreme properties. SGRs exhibit bursts and flares with intensity between $\sim 10^2$ and $\sim 10^{11}$ times their quiescent X-ray luminosity ($10^{34} - 10^{36}$ erg/s). In the last decade transient phenomena have been observed from few AXPs, with luminosity increases between few 10 and few 100 times the X-ray quiescent values. The many similarities in the timing and spectral properties among SGRs and AXPs led to the suggestion that they could be two different manifestations of the same phenomenon. These objects are believed to host a *Magnetar*, an ultra-magnetized neutron star with magnetic field $\sim 10^{14} - 10^{15}$ G.
In the *Magnetar* model emission from SGRs and AXPs comes to the expanse of the ultra strong magnetic field rather than of the rotational, gravitational or thermal energy. In *Magnetars* the external magnetic field can acquire a toroidal component as a consequence of the deformation of the star crust induced by the super-strong internal field. As a result the star magnetosphere twists up and the currents required to support the non-potential field may provide a large enough optical depth to resonant cyclotron scattering (RCS). As a consequence a distortion in the thermal spectra emitting by the star surface is expected, because primary photons gain energy in the repeated scattering with the magnetospheric charges. Spectra emerging from a twisted magnetosphere

in presence of RCS has been investigated by several authors (Lyutikov, & Gavriil, 2006; Fernandez, & Thompson, 2007; Nobili, Turolla, & Zane, 2008) and applied to SGRs and AXPs spectra by Rea et al. (2008) and Zane et al. (2008). The NTZ model 3D montecarlo simulation is the more advanced tool to compute both lightcurves and spectra. Resulting spectra are described in terms of 5 parameters: the twist angle $\Delta\phi$, the electron bulk velocity β, the surface temperature T and the two geometrical anglesξ and χ(ξ is the misalignement between spin and magnetic axis while χ is the line of sight inclination with respect to the spin axis).

In this thesis the application of NTZ model to two Transient AXPs XTE J1810-197 and CXOU J164710.2-455216 is discussed. XTE J1810-197 exhibited an outburst in late 2002 - early 2003, increasing its luminosity by two orders of magnitude. After the outburst onset the source has been monitored by *XMM-Newton* between September 2003 and September 2007, showing a decrease in flux until the pre-outburst value has been reached. CXOU J164710.2-455216 exhibited an outburst on 21 September 2006, when it was observed at a luminosity 300 times greater than that measured just five days before. The source has been observed by *XMM-Newton* 6 times after the outburst onset, between September 2006 and August 2009.

In this work, adapted from Albano et al. (2010) paper, a comprehensive study of the pulse profile and spectral evolution of the two TAXPs following their outbursts onsets is presented. By confronting timing data with synthetic lightcurves obtained from the twisted magnetosphere model (Nobili, Turolla, & Zane, 2008), we were able to estimate how the physical parameters of the source (surface temperature and emitting area, electron energy, twist angle) evolve in time. The fits of the pulse profiles also allowed us to infer the geometry of the two systems, i.e. the angles between the magnetic and rotational axes and the line of sight. Spectral models, obtained with the parameter values derived for the timing analysis, provide acceptable fits to *XMM-Newton* data.

This thesis is organized as follows: in Chapter 1 a brief introduction on Isolated Neutron stars major characteristics is presented. Chapter 2 deals with the *Magnetar* model and the NTZ montecarlo code. In Chapter 3 the application of the resonant cyclotron scattering model to the Transient AXP XTE J1810-197 is extensively discussed. Chapter 4 describes the application of the same model to the Transient AXP CXOU J164710.2-455216. Finally, in Chapter 5 our conclusions and further perspectives are presented.

Prefazione

Negli ultimi anni, grazie alla nuova generazione di satelliti (in particolare *Chandra* e *XMM-Newton*), è divenuto possibile osservare, con alta risoluzione, un crescente numero di stelle di neutroni isolate (INSs) che emettono raggi X. Molte nuove classi di INSs che emettono raggi X sono state scoperte, nessuna delle quali emette nel radio, o con proprietà nel radio in disaccordo con quelle delle PSRs: X-ray Dim Isolated Neutron Stars (XDINSs), Anomalous X-ray Pulsars (AXPs) e Soft Gamma-ray Repeaters (SGRs), Central Compact Objects (CCOs), Rotating Radio Transient (RRATs, in un caso).

AXPs e SGRs sono due gruppi di INSs con caratteristiche peculiari, formati in tutto da 15 oggetti (6 SGRs e 9 AXPs più una candidata). Anche se meno numerose delle PSRs, questi oggetti sono stati ampiamente studiati proprio in virtù delle loro proprietà peculiari ed estreme.

Gli SGRs mostrano bursts e flares con intensità tra le $\sim 10^2$ e le $\sim 10^{11}$ volte la loro luminosità quiescente in banda X ($10^{34} - 10^{36}$ erg/s). Nell'ultima decade fenomeni spettrali transienti sono stati osservati in alcune AXPs, con un aumento di luminosità compreso tra alcune decine e alcune centinaia di volte la luminosità di quiescenza. Le molte similarità nelle proprietà spettrali e di timing di SGRs e AXPs portano a suggerire che questi ogetti possano essere nient'altro che differenti manifestazioni dello stesso fenomeno. Si ritiene che queste sorgenti ospitino una *Magnetar*, una stella di neutroni ultra magnetizzata con campo magnetico pari a $\sim 10^{14} - 10^{15}$ G.

Nel modello *Magnetar* l'emissione da SGRs e AXPs proviene dall'espansione del campo magnetico ultra intenso piuttosto che ad energie di tipo rotazionale, gravitazionale o termico. Nelle *Magnetars* il campo magnetico esterno potrebbe acquisire una componente di tipo toroidale, come conseguenza della deformazione della crosta della stella indotta dall'intensissimo campo magnetico interno. Il risultato netto è un twist della magnetosfera della stella; inoltre le correnti richieste per supportare il campo non potenziale potrebbero dar luogo ad una profondità ottica sufficientemente spessa per il resonant cyclotron scattering (RCS). Di conseguenza ci si aspetta una distorsione negli spettri termici, dato che i fotoni primari guadagnano energia nei ripetuti urti con le particelle cariche presenti nella magnetosfera. Gli spettri all'uscita della magnetosfera twistata in presenza di RCS sono stati studiati da svariati autori (Lyutikov, & Gavriil, 2006; Fernandez, & Thompson, 2007; Nobili, Turolla, & Zane, 2008) e questo modello è stato applicato agli spettri di SGRs e AXPs da Rea et al. (2008) e Zane et al. (2008). Il codice montecarlo 3D creato da Nobili, Turolla, & Zane (2008) è lo strumento più avanzato per calcolare curve di luce e spettri. Gli spettri così ottenuti possono essere descritti in termini di 5 parametri: l'angolo di twist $\Delta\phi$, la velocità di bulk degli elettroni β, la temperatura superficiale T e i due angoli geometrici χ e ξ (ξ è il disassamento tra campo magnetico e asse di rotazione mentre χ è l'inclinazione della linea di vista rispetto all'asse di rotazione).

In questa tesi viene discussa l'applicazione del modello NTZ alle due sorgenti AXP transienti: XTE J1810-197 e CXOU J164710.2-455216. La prima ha mostrato un outburst tra la fine del 2002 e l'inizio del 2003, con un aumento della sua luminosità di due ordini di grandezza. Dopo l'inizio dell'outburst la sorgente è stata monitorata da *XMM-Newton* tra Settembre 2003 e Settembre 2007, mostrando una decrescita del flusso fino al raggiungimento del livello antecedente l'outburst. CXOU J164710.2-455216 ha mostrato un outburst il 21 Settembre 2006, e in quell'occasione è stata osservata ad una luminosità 300 volte maggiore rispetto a quella di quiescenza misurata solo 5 giorni prima. La sorgente è stata osservata 6 volte da *XMM-Newton* dopo l'inizio dell'outburst, tra Settembre 2006 e Agosto 2009.

In questo lavoro, riadattato dall'articolo Albano et al. (2010), viene presentato un ampio studio dei profili pulsati e dell'evoluzione spettrale delle due TAXPs a partire dall'inizio dell'outburst. Confrontando i dati di timing con le curve di luce sintentiche ottenute con il modello di magnetosfera twistata (Nobili, Turolla, & Zane, 2008), siamo stati in grado di stimare l'evoluzione temporale del parametri fisici della sorgente (temperatura superficiale e area emittente, energia degli elettroni, angolo di twist). I fit del profilo pulsato ci permettono anche di asserire la geometria del sistema, e cioè l'angolo fra campo magnetico e asse di rotazione e quello tra asse di rotazione e linea di vista. I modelli spettrali, ottenuti dai valori dei parametri derivati dall'analisi di timing, danno dei fit accettabili dei dati di *XMM-Newton*.

Questa tesi organizzata nel seguente modo: nel Capitolo 1 si riporta una breve discussione sulle maggiori caratteristiche delle stelle di neutroni isolate. Il Capitolo 2 tratta del modello *Magnetar* e del montecarlo NTZ. Nel Capitolo 3 si discute approfonditamente l'applicazione del modello RCS alla AXP transiente XTE J1810-197. Il Capitolo 4 descrive l'applicazione dello stesso modello alla AXP transiente CXOU J164710.2-455216. Infine, nel Capitolo 5 sono presentate le nostre conclusioni e le prospettive future.

Chapter 1

Neutron Stars

In 1934, only two years after the discovery of the neutron, the existence of neutron stars was proposed by astrophysicists Baade and Zwicky (Baade & Zwicky 1934). They suggested that neutron stars would be about 10 km in diameter and would be formed in a supernova explosion. Then, in 1967, Pacini proposed that the Crab Nebula was powered by such a star which was highly magnetised, rotating and emitting electromagnetic radiation, what we now know to be a pulsar. These theories were soon confirmed by Jocelyn Bell, Antony Hewish and colleagues in 1968 when they discovered the first pulsar (Hewish, Bell et al. 1968). At the time they were working on a large radio telescope, observing interplanetary scintillation and they noticed that, aside from the usual scintillation and man-made interference, there was some highly periodic signal. Further observations and analysis showed that this signal kept sidereal time which suggested that it was of extra-terrestrial origin. Several possible explanations were offered, including that the signal was generated by another civilisation, but it is now almost universally agreed that pulsars are rotating neutron stars which appear to pulsate as their radiation beams sweep the earth.

Neutron stars are the end points of the evolution of massive stars, with initial mass in the range $\sim 10 - 30\ M_\odot$ ($M_\odot = 1.989 \times 10^{33}$ g is the solar mass). Recently stars with initial masses $> 40\ M_\odot$ have been proposed as progenitors of highly magnetized neutron stars (Muno et al., 2007). These are compact objects containing, in their interior, matter at supranuclear density. These objects have typical masses $M \sim 1.44 M_\odot$, and radii ~ 10 km. Neutron stars possess an enormous gravitational energy $E_{grav} \simeq GM^2/R \simeq 5 \times 10^{53}$ erg $\sim 0.2Mc^2$ and a surface gravity $g \sim GM/R^2 \simeq 2 \times 10^{14}$ cm/s^2, where G is the gravitational constant and c is the speed of light. These are very dense objects, with $\rho \simeq 3M/(4\pi R^3) \sim 7 \times 10^{14}\text{g/cm}^3 \sim (2-3)\rho_0$, where ρ_0 is the normal nuclear density. Densities in the neutron star core can reach values of $(10-20)\rho_0$.

1.1 Neutron stars formation

A star in the main sequence, with an interior temperature of $1 - 3 \times 10^7$ K, uses hydrogen as nuclear fuel producting helium. After hydrogen exhaustion in the core, the star moves into the red-giant phase and helium starts to be burned, at a temperature of $\sim 10^8$ K. The burning helium results in carbon and oxygen (or both). The star continues to burn heavier elements, increasing its internal temperature, until elements of the iron group are synthesized. Iron burning is an endothermic process, and therefore can not take place in the stellar core. At this stage nuclear reactions in the core stop and the star can not balance its own gravity. The core density increases and electrons degeneracy becomes responsible for the pressure that balances the gravitational force. When the core mass exceeds the Chandrasekar limit ($M_{ch} \sim 1.44 M_\odot$), the degeneracy pressure can no longer support the star. As a consequence the core implodes and its temperature drastically increases till $\sim 7 \times 10^9\ K$, producing γ-rays. At this point equilibrium shifts from iron to helium, and the photondisintegration of ^{56}Fe into ^{4}He become the trigger mechanism of collapse

$$
\begin{aligned}
&^{56}Fe + \gamma \rightarrow 13\ ^4He + 4n \\
&^{4}He + \gamma \rightarrow 2p + 2n
\end{aligned}
$$

These reactions cause the core to becomes rich in free neutron number. The collapse increases the star density, and when $\rho \sim 10^7$ g/cm^2 inverse β-decay

$$
e^- + p \rightarrow n + \nu_e
$$

becomes energetic favorable. Free neutrons become stable and their degeneracy pressure balances the gravitational force.

The newborn neutron star is constituted by neutrons, protons and leptons (particularly e^- and ν_e). Neutrinos play a crucial role in Type II Supernova explosion, since they carry away a substantial fraction of the released energy. One important aspect in the very first phases of the proto neutron star is that neutrinos become temporary trapped. The core collapse stops at central density $\approx n_0$ ($n_0 \simeq 0.16$ fm^{-3} is the nuclear density in number), and at this point a shock wave at the core outer boundary develops. The shock wave propagates for about $100 - 200$ km, losing energy neutrinos and slowing down the free falling matter. It is possible that neutrinos from the core are able to ”resuscitate” the shock wave, maybe with the aid of convection, rotation, or magnetic fields; if this happens the removal of the star envelope becomes possible.

In ≈ 50 seconds the neutron star dimensions become smaller than the neutrino mean free path λ, and the compact object become transparent to the ν-radiation. Once the star has became transparent to neutrinos, the cooling rate increases, and in $\approx 10^3$ years νs subtract an energy sufficient to reduce the neutron star temperature from $\approx 10^{11}$ K to $\approx 10^6$ K. In this phase the neutron star cools itself also by photon emission, and after $\approx 10^5$ years, photons become the only source of the star cooling (see Fig. 1.1).

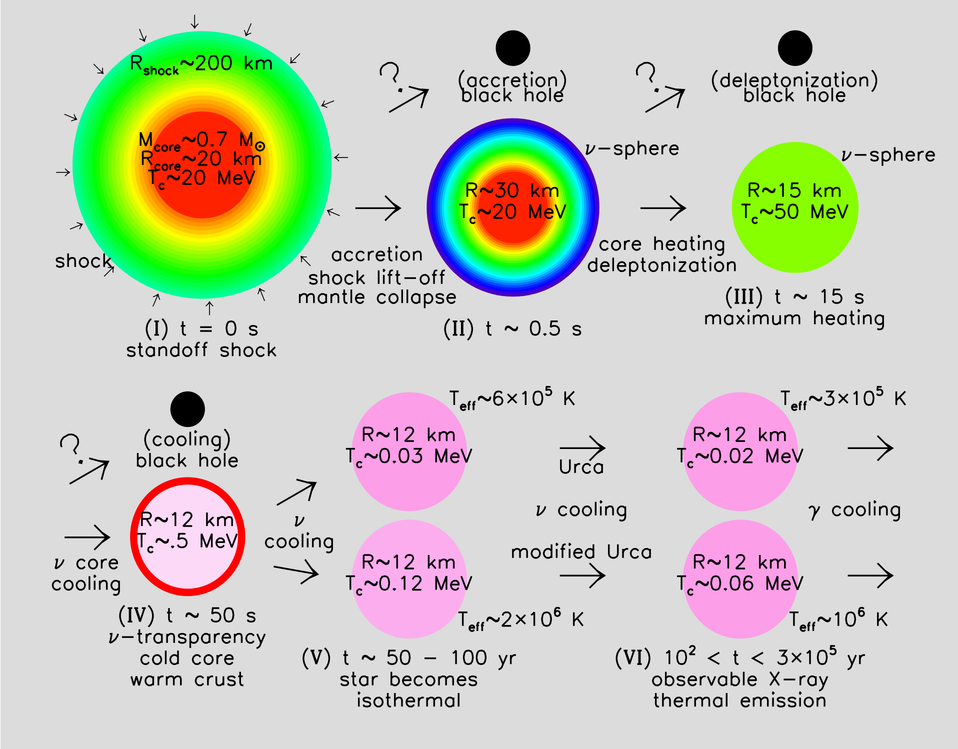

Figure 1.1: *Main evolutionary stages of a neutron star (Lattimer & Prakash 2004)*

1.2 Isolated Neutron Stars

Neutron stars can be isolated or be part of binary sistem. In the latter case the source is often powered by accretion of material lost from the companion, giving rise to an X-ray binary, while in the former emission is generally sustained by rotational energy losses.

An isolated neutron star is sketched as an oblique rotator in vacuum, with a magnetic field that can be approximated, to first order, as a pure dipole (Pacini 1967, see Fig. 1.2). The rotating dipole produces emission of electromagnetic waves according to the formula

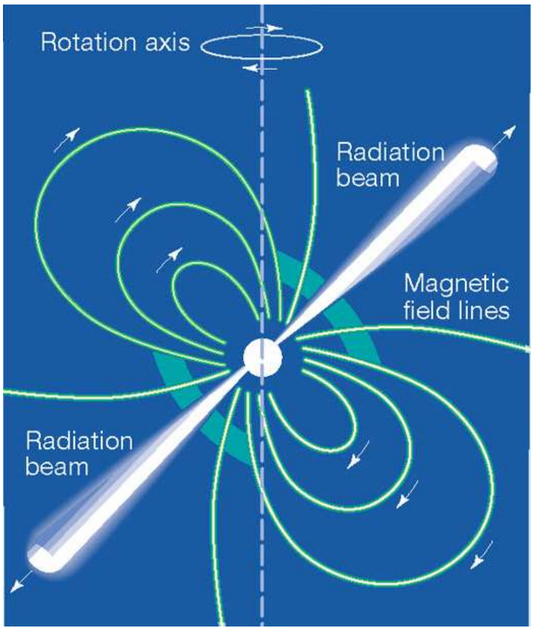

Figure 1.2: *Schematic representation of the dipole pulsar model.*

$$\dot{E} = \frac{2\Omega^4 |m|^2 \sin^2 \alpha}{3c^3} \mathrm{erg/s} \tag{1.1}$$

where Ω is the rotational velocity, α is the angle between spin and magnetic axis, m is the magnetic dipole moment $|\vec{m}| = Br^2/2$ (with B the field intensity).

The total spin luminosity in a rotation-powered pulsar, is given by the loss rate of rotational kinetic energy

$$\dot{E} = I\omega\dot{\omega} = \frac{4\pi^2 I\dot{P}}{P^3} \tag{1.2}$$

where I is the stellar moment of inertia, $\omega = 2\pi/P$ is the angular frequency, and P the spin period. Considering standard values for a neutron star, mass $M = 1.4M_\odot$, radius $R = 10$ km, and assuming $I = kMR^2 = 10^{45}$ g cm^2, measurement of P and $\dot{P}$ for a rotation-powered pulsar allows us to determine $\dot{E}$. Using Eqs. 1.1 and 1.2 it is possible to derive a value for the magnetic field and also for the source age, simply considering that: $B = 3.2 \times 10^{19}(P\dot{P})^{1/2}\ G$ (for B at the equator), and $\tau_c = P/2\dot{P}$ years.

Even if information on age and magnetic field are model dependent (B is assumed to be a rotating magnetic dipole in vacuum), the important point is that P and $\dot{P}$, together with $\dot{E}$, give estimates of other important physical properties. A graphic summary of this is given in the $P - \dot{P}$ diagram, showed in Fig. 1.3.

Generally X-ray spectra of rotation-powered pulsars show a superposition of thermal and non-thermal components. Often several thermal components and sometimes even several non-thermal components can be identified. Disentangling a non-thermal, typically power-law, component from the thermal one can be difficult, especially in sources were thermal components dominate (e.g. B1055-52, Geminga, PSRs 0656+14; Halpern & Wang 1997, Greiveldinger et al. 1996).

In the last years, a rich phenomenology emerged for isolated neutron stars (INSs), endorsing the classification of these objects into different classes. While Rotating Radio Transients (RRATs) and Rotation-Powered Radio Pulsars are radio loud emitters, Anomalous X-ray Pulsars (AXPs), Soft Gamma-Ray Repeters (SGRs), Central Compact Objects (CCOs) and X-ray Dim Isolated Neutron Stars (XDINSs) are generally radio-quiet (even if with some exceptions, that will be described in the following).
In next sections the principal characteristics of these classes of Isolated Neutron Stars are summarized.

1.2.1 X-Ray Dim Isolated Neutron Stars

X-ray Dim Isolated Neutron Stars (XDINSs) are a group of seven objects discovered by ROSAT, with low luminosity ($10^{30} - 10^{31}$ erg s^{-1}), not associated with supernova remnants. Except recent candidates, the number of confirmed XDINSs remained the same since 2001, so they are named “Magnificent Seven”.
These objects exhibit very soft purely thermal X-ray spectra, and a high X-ray to optical flux ratios ($f_X/f_V > 10^4$).
The low values of column density ($n_H \sim 10^{20} - 10^{21}$ cm^{-2}) indicate distances of $\simeq$ few hundred pc (Posselt et al. 2006). In the case of RX J1856 this is confirmed by the parallax measurement corrisponding to a distance of 161^{+18}_{-14} pc (Van Kerkwjik & Kaplan 2006). Also for RX J0720.4-3125 a value for the parallax has been calculated by Kaplan et. al (2007) and Van Kerkwjik & Kaplan (2007) giving a distance of 360^{+170}_{-90} pc.
Thanks to the proper motion measurements faint optical counterparts have been certified for three XDINSs: RX J1856 (Walter & Matthews, 1997; Walter, 2001), RX J0720 (Motch & Haberl, 1998; Kulkarni & van Kerkwijk, 1998; Motch et al., 2003) and RX

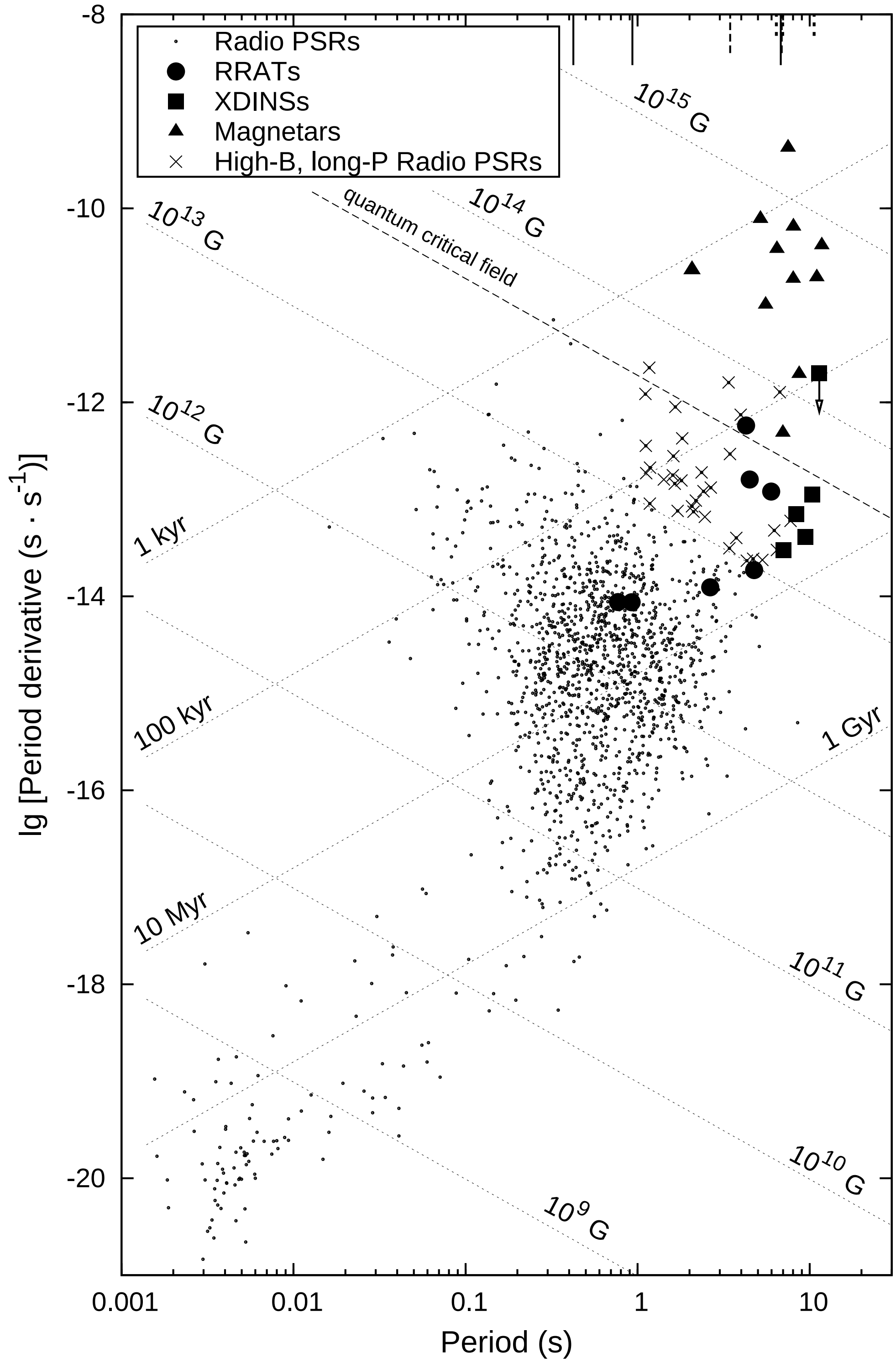

Figure 1.3: *$P - \dot{P}$ diagram for Isolated Neutron Stars. Lines of costant B and ages are indicated (Kondratiev et al., 2009)*

J1605 (Kaplan, et al., 2003; Motch et al., 2005; Zane et al., 2006). Moreover likely candidates have been proposed for other two sources: RX J1308 (Kaplan, et al., 2002) and RBS 1774 (Zane et al., 2008; Schwope et al., 2009), based on positional coincidence with the X-ray positions.

At least six sources exhibit pulsation in the X-ray flux, with periods in the range $3-12$ s. Emission in the radio waveband has been searched for six of the seven XDINSs by Kondratiev et al. (2009). These authors have found no transient or pulsed emission using the Robert C. Vyrd Green Bank Radio Telescope. However for RBS 1223 and RBS 1774 detection of weak radio emission at low frequencies ($\sim 150-200$ MHz) has been claimed (Malofeev et al 2006a, Malofeev et al 2006b).

Haberl et al. (2003) discovered in *XMM-Newton* EPIC spectra of RBS 1223, the first significant deviation from a pure blackbody. A broad absorption feature around 300 eV was interpreted as a proton cyclotron resonance line. Apart from RX J1856, for which however possible broadband deviations from purely thermal spectrum have been proposed (Burwitz et al. 2003), for all the other XDINSs at least one spectral feature has been discovered. Recently the presence of a second, harmonically spaced feature has been proposed for RX J1308 (Schwope et al., 2007), while Haberl (2007) reported the possibility of up to three lines in RX J1605. All these lines are supposed to be cyclotron resonance absorption features. In the $0.1-10$ keV band, cyclotron resonances absorption features are expected from strongly magnetized neutron stars, with magnetic field in the range $10^{10}-10^{11}$ G if caused by electrons, or with B in the range $2\times10^{13}-2\times10^{14}$ G if caused by protons (see Zane et al. 2001, Zavlin & Pavlov 2002 for details).

The constant X-ray flux on timescale of years, no obviously association with supernova remnants and the relatively high proper motion measurements for the three brightest sources, are all indications that XDINSs are a group of cooling neutron stars with ages $\simeq 10^6$ years.

The long periods sudgest the presence of a strong magnetic field. Infact, if XDINSs are born with millisecond spin periods ($10^{-3}-10^{-2}$ s) and their age is $\approx 10^6$ years, a magnetic field $\simeq 10^{13}$ G is required to decelerate the rotation of the star to the actual periods. This result has been confirmed by the determination of the pulse period derivatives in the range $0.698\times10^{-13}-4.1\times10^{-14}$ ss^{-1} for four XDINSs: RX J0720, RBS 1223, RX J1856 and RBS 1774 (Kaplan & van Kerkwijk, 2005a,b, 2008, 2009a). From the magnetic dipole braking model the characteristic ages are 1.9×10^6 years, 1.5×10^6 years, 3.8×10^6 years and 3.7×10^6 years and the magnetic field strength

2.4×10^{13} G, 3.4×10^{13} G, 1.5×10^{13} G and 2×10^{13} G. Such strong fields support the idea that the broad absorption lines are caused by protons cyclotron resonances.
Recently a limit on the spin down rate for the XDINSs RX J0806.4-4123 of $\simeq 10^{-16}$ ss^{-1} has been obtained by Kaplan & van Kerkwijk (2009b).
In the last four years XMM-Newton observations of RX J0720 revealed a substantial change in the spectral shape and pulse profile for this source, over a timescale of ~ 2 years. These variations are possibly caused by the precession of the star with a period of $\simeq 7$ years (Haberl et al. 2006). Similar variations in pulse profile of RX J0420 over a timescale $\simeq 0.5$ years have also been reported, although only at a low significant level (Haberl et al., 2004; de Vries et al., 2004; Vink et al., 2004, 2005).

1.2.2 Rotating Radio Transients

Rotating Radio Transients (RRATs) are a group of twenty sources, discovered for the first time in 2005 in the Parkes Multibeam Survey (Mclaughlin et al. 2006, Deneva et al. 2008, Keane et al. 2009). These objects are characterized by erratic brief radio bursts ($2 - 30$ ms) with average intervals between bursts ranging from 4 minutes to 3 hours. RRATs are concentrated at low Galactic latitudes, and with estimate distances of $\simeq 2 - 7$ kpc.
Periodicities in the range $0.4 - 7$ s have been found. For few sources a $\dot{P}$ measurement has been obtained too. In these cases it is possible to give an estimate of the lifetime in the range $0.1 - 4$ Myr, and of the magnetic field in the range $2 \times 10^{12} - 5 \times 10^{13}$ G. In the $P - \dot{P}$ diagram RRATs occupy an extensive region (see Fig. 1.3). In fact:

- RRAT J1913+3333 has the same spin properties of the bulk of radio pulsars
- RRAT J1317-5759 even if has a long spin period, it has properties typical of Radio Pulsars
- RRAT J1819-1485 is a very young object, with high magnetic field ($B = 5 \times 10^{13}\ G$), and is located in the *Magnetar* and high-field radio pulsars region

The last source, RRAT J1819, is the only one for which an X-ray counterpart has been found (Reynolds et al. 2006,Mclaughlin et al. 2007). X-ray spectrum can be easly modeled by an absorbed blackbody at $kT = 0.14 \pm 0.01$ keV and a hint of a power law component with $\Gamma \sim 2$ (Rea et al., 2009). Moreover a broad spectral absorption line has been detected.

In the last few years several models have been presented in order to explain the properties of these peculiar objects. Most of these models consider RRATs as normal Radio Pulsars. Zhang et al. (2006) describe RRATs as no longer active pulsars, for which a temporary "star spot" with multipole field components emerges above the surface. The magnetic field component reactivates, for a brief time, the radio beaming mechanism, producing the observed bursting. This model, however, is not supported by the position of RRATs in the $P - \dot{P}$ diagram, since no one of these sources is near the "death line". To account for this, Zhang et al. (2006) proposed that RRATs have dipole fields offset from their centers, causing their magnetic field to be overstimated by the magnetic dipolar braking model.

These authors also considered another possibility to justify RRATs properties. They suppose that RRATs emission is caused by a brief reversal in the beam direction. As postulated by Gil et al. (2004) for PSR B1822-09, they invoke an emitting geometry in which the main pulse is never seen, and the RRAT-like emission is due to the interpulse alone, appearing only when the unseen main pulse nulls. Drawbacks in this scenario are in the reversal time, that is a few minutes for PSR B1822-09, while has not been observed yet for RRATs.

A further mechanism proposed to explain these peculiar sources postulates that the RRAT behaviour may be produced by the interaction of the neutron star with an equatorial fallback disk, or with orbiting circumpolar debris. Accretion from a disk should usually quench the radio emission mechanism, but sporadic drops in the accretion rate could allow the radio beam to turn on for a fraction of second, producing RRAT phenomena (Li et al. 2006).

1.2.3 Central Compact Objects

Central Compact Objects (CCOs) are a group of seven (plus several candidates) soft X-ray sources characterized by constant unpulsed X-ray emission ($L_X \simeq 10^{33}$ erg s^{-1}) with high temperature thermal-like spectra ($\sim 0.2 - 0.4$ keV) and very small emitting areas (few % of the total neutron star surface). These sources are located in the center of young supernova remnants, and lack IR/optical/radio counterparts, as well as non-thermal nebule and surrounding diffuse emission (Pavlov et al. 2002, Pavlov et al. 2004).

Different models have been proposed to account for the CCOs peculiar properties. At least two of these sources, infact, seem to be neutron stars with weak magnetic field.

One source could be a very peculiar *Magnetar*, and for another one a *Magnetar* in a long-lasting quiescence phase scenario has been proposed.

It is possible that CCOs includes both weakly magnetized and *Magnetar* models.

Weakly magnetized scenario is based on the link between slow rotation of the proto-neutron star, inefficient magnetic field generation and accretion of fallback material (Gotthelf, & Halpern 2008). The greatest problem for this scenario is accounting for the details of X-ray emission.

On the other side the "dormant" *Magnetar* scenario can partially account for high field CCOs behaviour. A confirmation for this model would have important consequences on our estimate of the Galactic population of *Magnetars*, and on the birth rate of these objects.

1.2.4 AXPs and SGRs

Soft γ-ray Repeaters (SGRs; 6 objects) and Anomalous X-ray Pulsars (AXPs; 9 objects plus 1 candidate) are two peculiar groups of isolated neutron stars which stand apart from other known classes of X-ray sources. Both groups exhibit X-ray pulsations with periods in the range $2 - 12$ s. Period derivatives have been measured for all the confirmed AXPs and SGRs, finding values between 10^{-10} ss^{-1} and 10^{-13} ss^{-1} (Woods & Thompson, 2004; Mereghetti, 2008). Their X-ray luminosity is too high ($L_X \simeq 10^{34} - 10^{36}$ erg s^{-1}) to be powered by rotational energy losses. Moreover, searching for a companion for AXPs and SGRs gave no result, and this strongly argues against accretion as the mechanism powering these sources. Simultaneous P and $\dot{P}$ measurements give values of $\tau \sim 10^3 - 10^5$ years for characteristic age and of $B \sim 10^{14} - 10^{15}$ G for the magnetic field. Magnetic fields are always greater than the QED critical value ($B_{QED} = \frac{m^2c^3}{\hbar e} = 4.4 \times 10^{13}$ G).

Because of their great magnetic field, these objects are usually referred to as *Magnetars* (MAGNETic stARS; see Chap. 2 for details).

SGRs were discovered for the first time in January 1979, when SGR 1806-20 emitted a burst of soft γ-rays lasting a quarter of a second. Originally the burst was classified as a peculiar Gamma-Ray Burst (Mazets and Golenetskii 1981), with a soft spectrum and a short duration. A second burst of the same type, but more intense than the first one, was observed some months later from SGR 0526-66. This was a burst of extraordinary brightness, with a luminosity peak of $\approx 10^{45}$ erg s^{-1}, followed by a train of coherent 8 s pulsations, lasting about 3 minutes and with a quasi-exponential flux decay. The high luminosity, strong pulsations and apparent association with a supernova remnant strongly suggested that this source could be a young ($\approx 10^3$ years), magnetized neutron star with a spin period of 8 s. The correct origin of these bursts was not clear until 1983, when SGR 1806 showed an intense reactivation, providing pellucid evidence that these sources do repeat.

AXPs were first observed in 1981, when Fahlman and Gregory (1981) discovered pulsations in the X-ray source 1E 2259+586. At the beginning this source was identified as a peculiar X-ray binary, but 1E 2259 showed no optical counterpart, and its spectrum was much softer than that of an accreting pulsar. New observations of this source revealed a secular spin down. In the following years other sources like this have been discovered.

Spectral properties

AXPs spectra in the $0.1 - 10$ keV range show two components and are usually fitted with a blackbody plus power law model ($T \sim 0.5$ keV and $\Gamma \sim 3 - 4$) or with two BBs (see Halpern et al. 2005). Recently spectra components in the $20 - 150$ keV range have been revealed with the INTEGRAL satellite (Molkov et al. 2004, Kuiper et al. 2006, den Hartog et al. 2006). This was an unexpected result, especially considering the soft spectral index below 10 keV. This hard tail can be fitted with a $\Gamma \sim 1 - 2$ power-law (see Fig. 1.4).

SGRs, on the contrary, have harder spectra, that are usually fitted with a BB+PL ($\Gamma \sim 2$) under 10 keV, and are subjected to large interstellar absorption, so that for the majority of these sources thermal blackbody-like component is difficult to reveal. A hard tail between 20 and 150 keV was already present in earlier data, and has been confirmed by INTEGRAL observations (Mereghetti et al. 2005a, Göts et al. 2006; see again Fig. 1.4).

Variability properties

Soft Gamma-ray repeters have been discovered thanks to their recurrent activity, during which a large number of bursts in the hard X-ray/soft γ-ray bands are emitted. These are quite energetic events, with peak luminosity up to $\sim 10^{42}$ erg/s lasting approximately $0.01 - 1$ s. Most of the bursts consist of a single or few peaks with fast rise time, usually shorter than the decay times.

Few years ago RXTE revealed a similar burst activity from Anomalous X-ray Pulsars

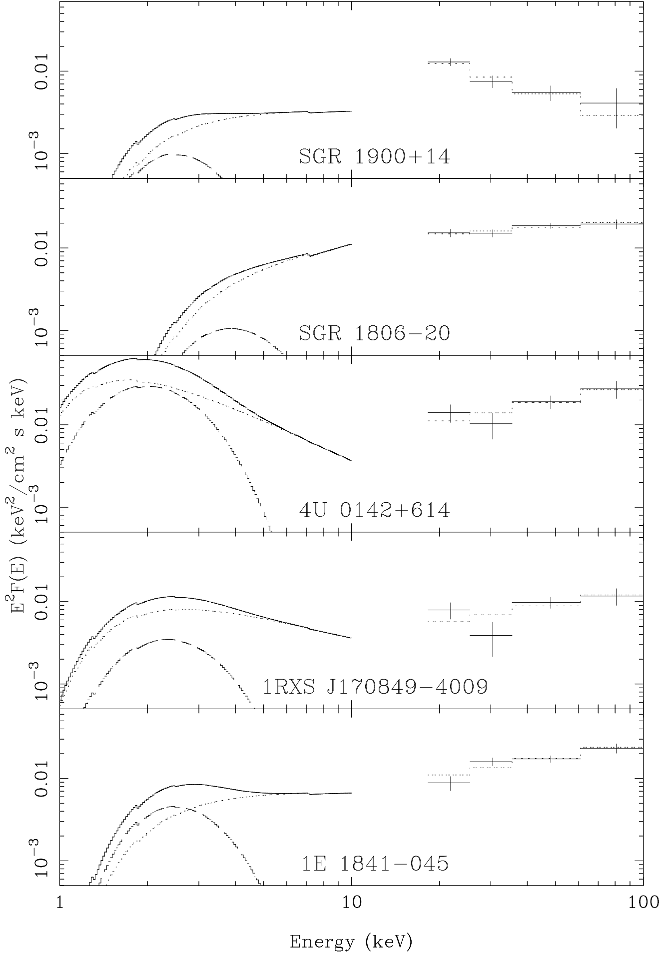

Figure 1.4: *XMM-Newton and INTEGRAL spectra of magnetars (Göts et al. 2006)*

(Kaspi et al. 2000, Kaspi et al. 2003) sudgesting the idea that SGRs and AXPs are two different manifestations of the same class of objects. At present bursts with extended tails lasting tens to hundreds seconds have been observed in several AXPs. AXP 1E 2259+586 showed also SGRs-like bursts. Woods et al. (2005) suggest the idea that SGR-like bursts are caused by crustal fractures, while AXPs-like bursts are caused by magnetic reconnection.

SGRs are characterized by extremely rare and energetic events, during which enormous amounts of energy are released ($\sim 10^{44} - 10^{47}$ erg/s). Actually three of these events have been observed by three SGRs: 0526-66 (March 5, 1979), 1900+14 (August 27, 1998) and 1806-20 (December 27, 2004; see Fig. 1.5). A fraction of this energy escapes directly during the electron/positron plasma expansion, while the remaining part is radiated by the fireball trapped into the magnetosphere. Giant flares light curves are characterized by a short hard spike followed by a longer pulsating tail. Temperatures of $\sim$ few 100 keV are derived for initial spikes, with spectra harder than those of nor-

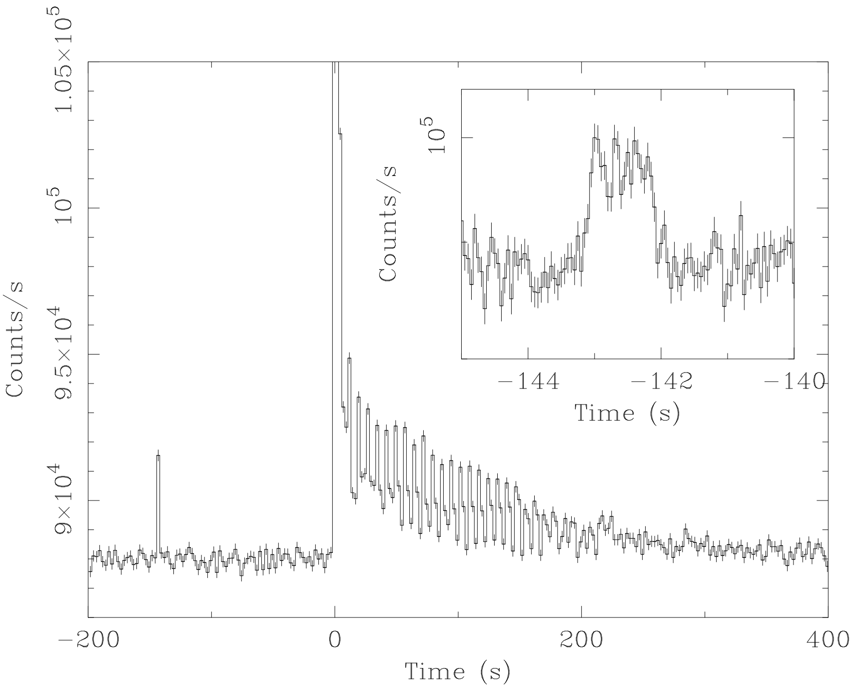

Figure 1.5: *INTEGRAL lightcurve of SGR 1806-20 Giant Flare (Mereghetti et al. 2005b)*

mal SGRs bursts. The pulsating tails are characterized by a strong evolution in flux, spectra and timing properties. Spectra are softer than initial spikes, with temperature of $\sim$ few 10 keV. Analysis of energy trapped in the neutron star magnetosphere and released after the initial spike, allow to estimate magnetic field for these sources. With this method values of $\sim$ several 10^{14} G have been found for the three SGRs for which giant flares have been observed, in agreement with estimates obtained from the spin-down measures.

In the last years transient phenomena have been observed from a few AXPs, consisting in a rapid increase in flux, followed by a decay lasting some year, and characterized by a variation in spectral and timing properties.

The first case of AXP flux variability was observed in 2002, when 1E 2259+586 showed an increase in the persistent flux of a factor $\sim$ 10 with respect to the quiescent level, followed by the emission of $\sim$ 80 short bursts with luminosity $L_X \sim 10^{36} - 10^{38}$ erg s^{-1}. In early 2003 the 5.54 s AXP XTE J1810-197 was discovered at a luminosity $\sim$ 100 greater than its quiescent value (10^{33} erg s^{-1}; Ibrahim et al. 2004). Analysis of archival data revealed that the outburst started between November 2002 and January 2003 (see section. 1.3.1 for details).

On September 21st 2006 an outburst was observed from the AXP CXOU J164710.2-

455216 ($P = 10.61$ s). The flux level was ~ 300 times higher than that measured only 5 days before by *XMM-Newton* (Muno et al., 2006b; Campana, & Israel, 2006; Israel, & Campana, 2006) (see section. 1.3.2 for details). Recently the AXP 1E 1547.0-5408 showed a series of short bursts of soft γ-rays which have been detected by different satellites (Mereghetti et al., 2009).

Transient behaviour has been observed also for SGR 1627-41 (Woods et al. 1999), discovered in 1998 thanks to an intense burst activity (~ 100 bursts in about six weeks), accompaning by an increase in the X-ray luminosity of a factor ~ 100, from the quiescence value of $\sim 4 \times 10^{33}$erg/s to the revealed value of $\sim 10^{35}$ erg/s.

The existence of transient *Magnetars*, with quiescent luminosity too small to be revealed with present generation of telescopes, has direct implications on the total number of *Magnetars* in the Galaxy, and also on their inferred birthrate. Infact it is possible that a large number of these sources have not been revealed yet because of their low quiescent luminosity.

1.3 Transient Magnetar Sources

1.3.1 XTE J1810-197

The Transient AXP (TAXP) XTE J1810-197 was serendipitously discovered in 2003 with the Rossi X-Ray Timing Explorer (*RXTE*) at an absorbed flux level of $\sim 5.5 \times 10^{-11}$ ergs cm^{-2} s^{-1} (Ibrahim et al. 2004). The source was readily identified as a X-ray pulsar and, soon after, a search in archival *RXTE* data showed that the source was already detected in February 2003 at a flux level of $\sim 8.64 \times 10^{-11}$ ergs cm^{-2} s^{-1} and that it produced an outburst between 2002 November 17 and 2003 January 23, followed by a monotonic decline of the X-ray flux (see Fig 1.6). Further research in *ROSAT* archival data revealed that the source have been observed in the '90s while in quiescence at a temperature of 0.15 keV. The X-ray pulsar spin period has been found to be 5.54 s, with a spin-down rate $\sim 1.8 \times 10^{-11}$ s s^{-1}. Using the standard expression for magneto-rotational losses, the inferred value of the (dipolar) magnetic field is $B \sim 3 \times 10^{14}$ G, with a characteristic age $\tau \lesssim 7600$ years (Ibrahim et al., 2004). The source was classified as the first transient *Magnetar*. The TAXP XTE J1810-197 was then studied by *Chandra* and *XMM-Newton* (Gotthelf et al., 2004; Israel et al., 2004; Rea et al., 2004a; Gotthelf, & Halpern, 2005, 2007), in order to monitor its evolution in the post-outburst phase.

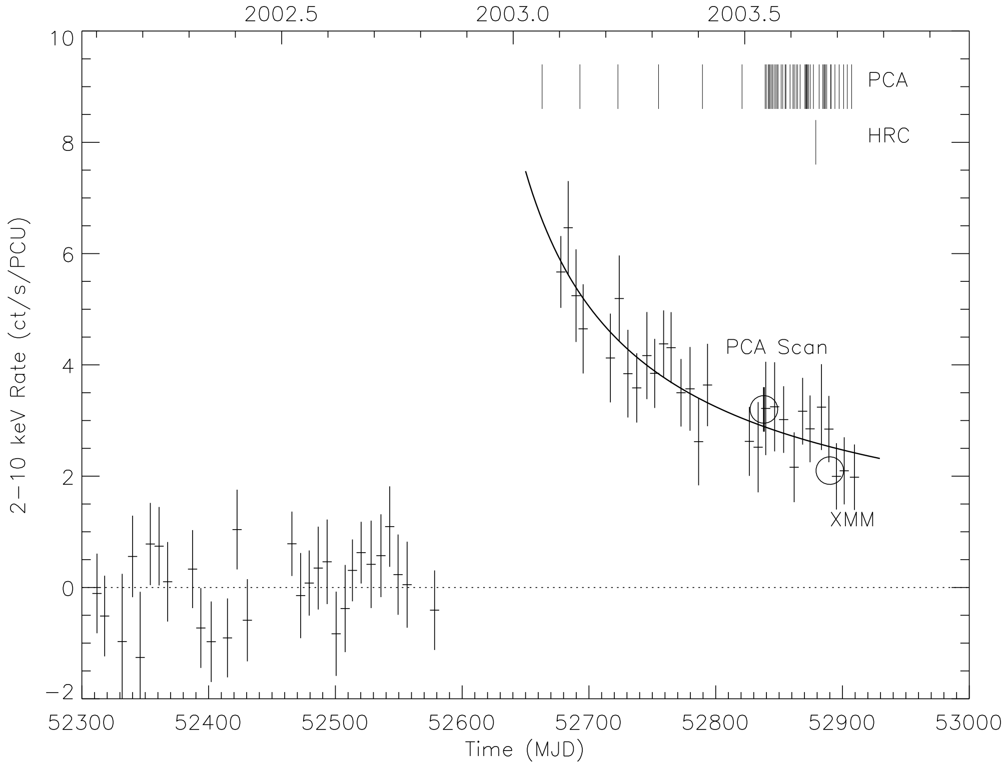

Figure 1.6: *Monitoring lightcurve of XTE J1810-197 showing the transient outburst beginning in the early 2003 (Ibrahim et al. 2004)*

XTE J1810-197 has been observed 9 times by *XMM-Newton*, between September 2003 and September 2007, two times every year. Given the smooth and nearly sinusoidal pulse shape, the pulsed fraction can be determined with resonable accuracy, simply as $PF = (A_{max} - A_{min})/(A_{max} + A_{min})$ where A_{max} and A_{min} are the maximum and minimum count rate during a cycle. During these four years the pulsed fraction decreased by a factor of ~ 2, from $\sim 50\%$ to $\sim 25\%$ in the $0.5-10$ keV energy band. In particular, the PF decreased until March 2005, and then remained constant at $\sim 25\%$. This value is very close to the PF upper limit inferred from ROSAT archival data between 1992 and 1993. XTE J1810-197 pulsed fraction is characterized by an increase as a function of energy within the same observation, and by a decrease as a function of time in the same energy band.

By using archival Very Large Array (*VLA*) data a transient radio emission with a flux of ~ 4.5 mJy at 1.4 GHz was discovered at the *Chandra* X-ray position of XTE J1810-197 (Halpern et al., 2005). Only later on it has been discovered that this radio emission was pulsed, highly polarized and with large flux variability even on very short timescales (Camilo et al. 2006). The X-ray and the radio pulsations are at the same rotational phase. Since accretion is expected to quench radio emission, this is further proof against the source being accretion-powered.

Deep IR observations have been performed for this source, revealing a weak ($K_s = 20.8$ mag) counterpart, with $F_X/F_{IR} > 10^3$, and with characteristics similar to those of other AXPs (Israel et al., 2004). The IR emission is variable (Rea et al., 2004b), but no correlations between the IR and X-ray changes have been found up to now. The existence of a correlation at IR/radio wavelengths is uncertain (Camilo et al., 2006, 2007a).

The uninterrupted coverage of the source during 4 years provides an unique opportunity to understand the phenomenology of TAXPs. Earlier observations of XTE J1810-197 showed that the source spectrum is well reproduced by a two blackbody model, likely indicating that (thermal) emission occurs in two regions of the star surface of different size and temperature: a hot one ($kT = 0.70$ keV) and a warm one ($kT = 0.30$ keV; Gotthelf, & Halpern 2005).

Perna & Gotthelf (2008) discussed the post-outburst spectral evolution of XTE J1810-197 from 2003 to 2005 in terms of two blackbody components arising from a hot spot and a warm concentric ring. By varying the area and temperature of the two regions, this (geometric) model can reproduce the observed spectra, accounts for the decline of the pulsed fraction with time and allows to place a strong constrain on the geometry of the source, i.e. on the angles between the line of sight and the hot spot axis with respect to the spin axis.

Recently, Bernardini et al. (2009) by re-examining all available *XMM-Newton* data found that the addition of a third spectral component, a blackbody at ~ 0.15 keV, improved the fits and caused the hot component to monotonically decrease in time, both in area and temperature, while the warm component decreases in area but stays at constant temperature. The coolest blackbody, which appears not to change in time, is associated to emission from the (large) part of the surface which has not been affected by the energy release which triggered the outburst, and is consistent with the spectral properties of the source as derived from a *ROSAT* detection before the outburst onset.

Finally, an interpretation of XTE J1810-197 spectra in terms of a resonant compton scattering model (RCS; see Chap. 2) has been presented by Rea et al. (2008).

1.3.2 CXOUJ 164710.2-455216

The TAXP CXOU J164710.2-455216 was discovered in two *Chandra* pointings of the young Galactic star cluster Westerlund 1 in May/June 2005. The period of the X-ray pulsar has been found to be $P = 10.61$ s (Muno et al., 2006), with a period derivative $\dot{P} = 9 \times 10^{-13}$ s s^{-1} (Israel et al., 2007). The implied magnetic field is $B \sim 10^{14}$ G. In 2006 November, an intense burst was detected by the *Swift* Burst Alert Telescope (BAT) in the open cluster Westerlund 1 (Krimm et al., 2006; Muno et al., 2006). Its short duration (20 ms) suggested that its origin was the candidate AXP. However the event was initially attributed to a nearby Galactic source, so the AXP was not promptly re-observed by *Swift*. A ToO observation program with *Swift* was started 13 hrs after the burst, displaying a persistent flux level 300 times higher than the quiescent one. Also CXOU J164710.2-455216 has been observed in radio, with the Parkes Telescope. The observation was carried out a week after the outburst onset, with the intent of searching for pulsed emission similar to that of XTE J1810-197. In this case, however, only a (tight) upper limit to the radio flux (40 μJy) was placed (Burgay et al., 2006). *XMM-Newton* observations carried out across the outburst onset show a complex pulse profile evolution. Just before the event the pulsed fraction was $\sim 65\%$, while soon after it the pulsed fraction became $\sim 11\%$ (Muno et al., 2007). Moreover, the pulse profile changed from being single-peaked just before the burst, to showing three peaks soon after it. CXOU J164710.2-455216 spectra in the outburst state have been fitted either with a two blackbody model ($kT_1 \sim 0.7$ keV, $kT_2 \sim 1.7$ keV), or by a blackbody plus power-law model ($kT \sim 0.65$ keV, $\Gamma \sim 2.3$; Muno et al., 2007; Israel et al., 2007). Rea et al. (2008) found that a RCS model also provides a good fit to the data.

Chapter 2

The Model

Anomalous X-Ray Pulsars (AXPs) and Soft Gamma-Ray Repeaters (SGRs) are actually referred to as *Magnetars* (MAGNETic stARS). *Magnetars* are isolated neutron stars for which rotating energy loss can not account for the observed luminosity. For these peculiar objects the magnetic energy is the dominant source for radiative emissions. The *Magnetar* model (see Duncan & Thompson 1992, Thompson & Duncan 1992) requires a very high magnetic field, $B > B_{QED} = 4.4 \times 10^{13}$ G, where B_{QED} is the critical magnetic field at which cyclotron energy and electron mass energy have the same value. Every time magnetic field is higher than B_{QED} plasma properties are strongly modified. In particular, as predicted by the quantum electrodynamics, in presence of a sufficiently strong magnetic field the vacuum around the neutron star may become birefringent.

Starting from P and $\dot{P}$ measurements it is possible to evaluate the magnetic field values for *Magnetars*, finding $B \simeq 5 \times 10^{13} - 2 \times 10^{15}$ G. Moreover persistent luminosity can be easily described with this model, since such a magnetic field is surely sufficient to sustain a luminosity of $10^{33} - 10^{35}$ erg s^{-1} for, at least, 10^4 years.

The *Magnetar* model allows us to justify the great deceleration that affect these objects during their first phases. Infact *Magnetars* are supposed to born as millisecond rotators, with a magnetic braking index sufficiently high to permit such a deceleration in 10^4 years. In order to obtain a $B \simeq 10^{14} - 10^{15}$ G for an object $\sim 10^4 - 10^5$ years old, an initial field strenght of $\simeq 3 \times 10^{17}(1\text{ms}/P_0)$ G is required. Such a field is hardly justifiable simply by invoching the flux conservation during the collapse phase preceding the proto-Neutron star formation.

Thompson & Duncan postulate that an internal field with a strength of 10^{17} G should be generate with the participation, during the first seconds of the neutron star formation, of a turbolent dynamo amplification ($\alpha\Omega$ Dynamo).

2.1 Internal field geometry

Thompson & Duncan (2001) suppose that, as a result of the postcollapse $\alpha\Omega$ Dynamo action, a strong toroidal component in the deep crust and core can compare. In such a case the magnetic energy of the neutron star is dominated by the internal field.
These authors assume that *Magnetar* crust is subjected to intense, evolving magnetic stresses. Before crust formation the star relaxes itself to an equilibrium configuration; then, when crust formation has taken place, core, crust and magnetic field evolve to a sequence of equilibrium states in which magnetic stresses are balanced by both elastic stresses in the crust and hydrostatic forces. Internal toroidal magnetic field, that is anchored to the crust, twists itself more and more. As a consequence internal crust is subjected to a magnetic force that increase with time. Since the neutron star crust has a finite shear strength, starquakes involve the object every time the torsion stress do to the magnetic field becomes higher than the crust breaking point.
In order to better understand *Magnetars* internal behaviour Tompson & Duncan (2001) focussed on a toy model. The *Magnetar* is described as a cylindrically symmetric star

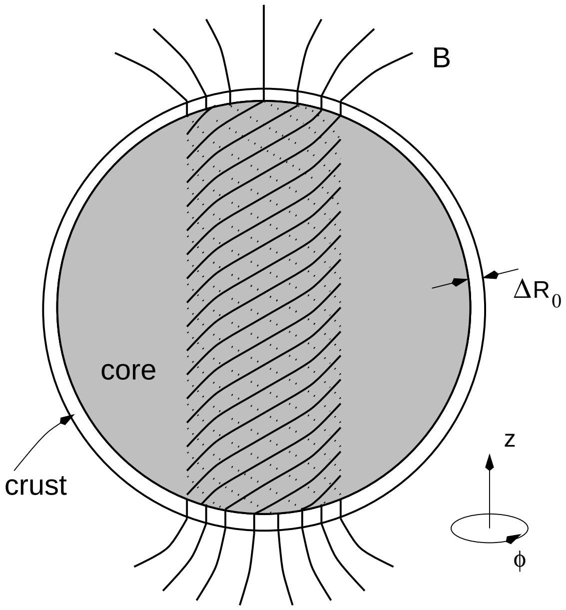

Figure 2.1: *Spherical star threated by uniform poloidal magnetic field. The magnetic field in the core is twisted, creating a toroidal component (Thompson & Duncan 2001)*

with an internal poloidal magnetic field $B_z < B_\mu$, where B_μ is the characteristic magnetic field above which the crust is able to respond plastically to applied magnetic stresses. Core magnetic field is assumed to be twisted along the magnetic dipolar axis (that is also the symmetry axis), and, as a result, a toroidal component B_ϕ generate itself (see Fig 2.1). When the star interior is in equilibrium, that is before the critical point is reached, the crust is affected by a stress $B_z B_\phi / 4\pi$, that is applied to the lower base of the crust, and is balanced by the elastic stress $\sigma_{\omega\phi}$ that is proportional, via the shear modulus μ, to the equilibrium strain $\psi(\omega)$, that depends only on the cylindrical radius.

The equilibrium strain ψ is simply proportional to the cylindrical radius, via the toroidal magnetic field strength B_ϕ. This means that there is a cylindrical radius r_{frac} at which we expect the first break in the neutron star crust. Before the crust break, the twisted magnetic field stored an amounth of energy δE_{mag} that depends only on the squared cilyndrical radius and on the squared toroidal magnetic field strength $\delta E_{mag} \propto r_{frac}^2 \times B_\phi^2$. δE_{mag} is released during the starquake, and it is the energy observed during AXPs and SGRs drammatic flaring events.

2.2 External field geometry

Usually external fields are modeled with a simple dipole magnetic field. Thompson, Lyutikov, & Kulkarni (2002) generalize this model by adding an electrical current flowing continuously across the entire neutron star surface. They initially consider a no rotating object, with close field lines expanding in an infinite volume outside the star.

In such a condition the standard MHD equation

$$\rho \frac{\partial v}{\partial t} + \rho(\mathbf{v} \cdot \nabla)\mathbf{v} = -\nabla p + \rho \mathbf{g} + \mathbf{j} \times \mathbf{B} \tag{2.1}$$

(ρ and $\mathbf{v}$ are the plasma density and velocity) can be reduced to:

$$\nabla p = \mathbf{j} \times \mathbf{B} \tag{2.2}$$

With the further hypotesis that the plasma pressure force is small with respect to the Lorenz force $\mathbf{j} \times \mathbf{B}$, the equation can be written as

$$\mathbf{j} \times \mathbf{B} = 0 \tag{2.3}$$

In the stationary configuration, the Ampére-Maxwell equation is simply

$$\nabla \times \mathbf{B} = (4\pi/c)\mathbf{j} \tag{2.4}$$

Equations 2.3 and 2.4, combined togheter, return the force free equation $(\nabla \times \mathbf{B}) \times \mathbf{B} = 0$. Solving this equation gives us the possibility to determine the structure of $\mathbf{B}$ around a highly conducting spherical mass of radius R_{NS}. The solution of this equation can be formally written as:

$$\nabla \times \mathbf{B} = \alpha(\wp)\mathbf{B} \tag{2.5}$$

If the magnetoshpere is axisymmetric then the magnetic field lines can be described as 1-dimensional and are labelled by the flux parameter $\wp = \wp(R, \theta)$.
The poloidal magnetic field will simply be:

$$\mathbf{B_z} = \frac{\nabla\wp\times\hat{\phi}}{R\sin\theta} \Rightarrow \begin{cases} B_\theta = -(R\sin\theta)^{-1}\frac{\partial\wp}{\partial R} \\ B_R = -R^{-2}\frac{\partial\wp}{\partial\cos\theta} \end{cases} \tag{2.6}$$

As in Lynden-Bell & Boily (1994) we can write $\wp = \wp_0 r^{-p} F(\cos\theta)$, where $r = R/R_{NS}$, θ is the magnetic colatitude and $\wp_0 = 1/2 B_{pole} R_{NS}^2$.
From Eq. 2.5 we can conclude that $\alpha(\wp) \propto \wp^{1/p}$; in particular

$$\alpha(\wp) = \frac{C^{1/2}}{R_{NS}}\left(\frac{p+1}{p}\right)^{1/2}\left(\frac{\wp}{\wp_0}\right)^{1/p} \tag{2.7}$$

The field line shape depends only on C parameter, which is related to the current strength.
With simple mathematical steps it is possible to obtain

$$p(p+1)F + (1-\mu^2)\frac{\partial^2 F}{\partial\mu^2} = -CF^{1+2/p} \tag{2.8}$$

where F is a function only of $\mu = \cos\theta$.
The solution of this equation is uniquely determined by the parameter C and by the boundary conditions:

- At the magnetic equator ($\mu = 0$) $B_R \propto F'$
- If $\mu = 1$, that correspond to a fixed flux density B_{pole} at the magnetic pole, $F' = const = -2$
- $B_\phi(\mu = 1) \propto F(1) = 0$

Solutions obtained are symmetric for $\mu \leftrightarrow -\mu$, and $F(\mu) = 1-\mu^2$ represent the solution for the pure dipole.
The twist force free magnetosphere has a finite toroidal field: $\frac{B_\phi(\theta)}{B_\theta(\theta)} = \sqrt{\left[\frac{c}{p(1+p)}\right]F(\theta)}$.

It is possible to describe the net twist angle of a magnetic field line anchored at the polar angle θ as

$$\Delta\phi(\theta) = \int_0^{\pi/2} \frac{B_\phi(\theta)}{B_\theta(\theta)} \frac{d\theta}{\sin\theta} \tag{2.9}$$

In the case of modest twist angles, $\Delta\phi_{N-S} \lesssim 1$ the integral of Eq. 2.9 can be approximated with

$$\Delta\phi_{N-S} \simeq 2 \frac{B_\phi(\theta)}{B_\theta(\theta)}_{\theta=\pi/2} \tag{2.10}$$

The p parameter is a monotonically function of the twist angle $\Delta\phi_{N-S}$. See Fig 2.2 for an example of a twisted self-similar magnetosphere.

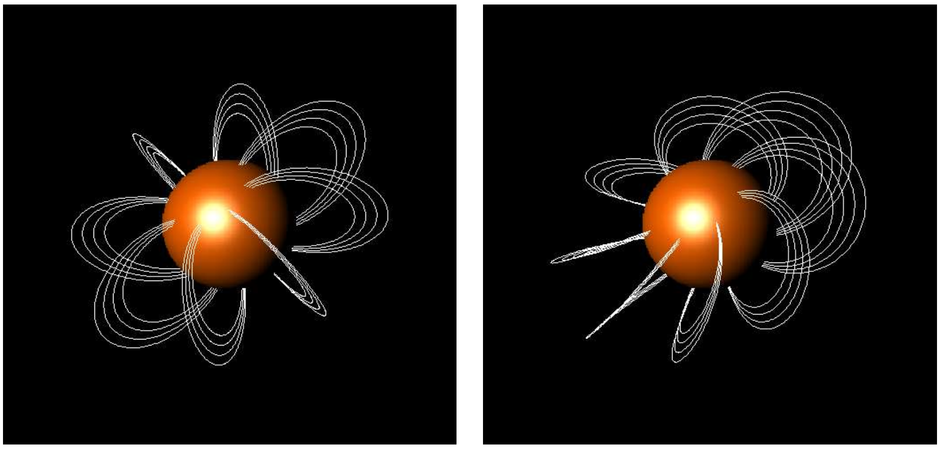

Figure 2.2: *Comparison between a twist self-similar magnetosphere with* $\Delta\phi_{N-S} \neq 0$ *(right panel) and a pure blackbody* $\Delta\phi_{N-S} = 0$ *(left panel)*

2.3 The resonant cyclotron scattering

In a twisted force free equilibria model, current-carrying charges play a significant role in increasing the optical depth thanks to resonant cyclotron scattering.

Let us consider a charge particle with mass M and charge Ze, with a resonant frequency $\omega_c = \frac{ZeB}{Mc}$. This particle scatters a photon of frequency ω, with a cross section

$$\sigma_{res}(\omega) = \pi^2 \frac{Z^2 e^2}{Mc} \delta(\omega - \omega_c)(1 + \cos^2\theta_{kB}) \tag{2.11}$$

where θ_{kB} is the angle of incidence with respect to the magnetic field **B** (Canuto, Lodenquai, & Ruderman 1971).

Thermal photons leaving the *Magnetar* surface are strongly scattered at the cyclotron resonance, while they remain almost unscattered near the poles.

For the resonant optical depth along a ray Thompson, Lyutikov, & Kulkarni (2002) found a value inversely proportional to the gradient of magnetic field parallel to the ray

$$\tau_{res} = \pi^2 (Ze) n_Z (1 + \cos^2\theta_{kB}) \left| \frac{dl}{dB} \right| \tag{2.12}$$

Such a model accurately describes the magnetospheric structure and behaviour of a *Magnetar* starting from a distance where magnetic field lines are anchored in a small portion of the surface. This means that the scattering surface better approximate the axisymmetric model at lower frequency and for electron cyclotron resonances than for ion resonances.

With this modellization it is possible to define the magnetospheric electron density as:

$$n_e(\mathbf{r}, \beta) = \frac{p+1}{4\pi e} \left(\frac{B_\phi}{B_\theta} \right) \frac{B}{r| < \beta > |} \tag{2.13}$$

where $< \beta >$ is the average electron velocity (in units of c).

Electrons moving along the magnetic field lines have a well defined direction which is the same from north to south. This involves a break in the two star hemispheres symmetry, with the consequence that observed spectra will be different when viewed from the south pole or the north one. Charge neutrality assures electrons to be balanced by ions moving in the opposite direction. As already said, ions used to move very close to the neutron star surface, so in the following their contribution will be neglected.

Charge particles velocity distribution can be described with a 1-D Maxwellian distribution at a given temperature T_e, to which is superimposed a bulk motion with velocity v_{bulk}. This choise appears to be a good one if we consider that electrons are dipped into a strong magnetic field, i.e. their distribution is strongly anisotropic. Particles are, infact, free to move along the magnetic field lines, but they are confined in a set of Landau levels in the plane perpendicular to $\mathbf{B}$.

2.4 The Montecarlo Code

In the last years an increasing number of models able to describe X-ray spectra emerging from twisted magnetospheres has been computed. In this section the Nobili, Turolla, & Zane (2008) (NTZ) one is analysed. In Chapeters 3 and 4 the application of this model to the two *Magnetar* candidates XTE J1810-197 and CXOU J164710.2-455216 will be described in details.

These authors create a 3-D montecarlo code in the case of resonant cyclotron scatter-

ing. Starting from the configuration previously described, they studied the motion of thermal photons emitting from the neutron star surface.
Since *Magnetars* have magnetic field appreciably greater than B_{QED}, photon polarization has been include in the model. As a consequence photons have different cross sections according to their initial polarization. In particular:

$$\begin{aligned} \sigma_{1-1} &= \tfrac{\pi^2 r_0 c}{2}\delta(\omega-\omega_D)\cos^2\theta \\ \sigma_{2-2} &= \tfrac{3\pi^2 r_0 c}{2}\delta(\omega-\omega_D) \end{aligned} \tag{2.14}$$

where $\omega_D = \frac{\omega_B}{\gamma(1-\beta\mu)}$, θ is the angle between the particle velocity (in ERF) and photon particle direction, μ is the cosine of the same angle but measured in the stellar rest frame. With simple matematical steps these authors obtain the total scattering depth for the two polarization modes:

$$\begin{aligned} d\tau_1 &= 2\pi^2 r_0 c\tfrac{n_e\omega_B}{\omega^2}dl\textstyle\sum_{k=1,2}\tfrac{|\mu-\beta_k|}{(1-\mu\beta_k)}f_e(\mathbf{r},\beta_k) \\ d\tau_2 &= 2\pi^2 r_0 c\tfrac{n_e\omega_B}{\omega^2}dl\textstyle\sum_{k=1,2}\tfrac{(1-\mu\beta_k)}{|\mu-\beta_k|}f_e(\mathbf{r},\beta_k) \end{aligned} \tag{2.15}$$

where $f_e(\mathbf{r},\beta_k) = ne^{-1}\frac{dn_e}{d\beta}$. In order to simplify the montecarlo code all calculations have been done neglecting the relativistic effects, and considering that photons move along straight lines between one scattering and the next. Moreover electrons are assumed to move isothermically along the field lines and to receive the same boost from the electric field.

The montecarlo code procedure can be described as follow. First of all primary thermal photons are emitted from the *Magnetar* surface. Since temperature distribution can be anisotropic, the neutron star surface has been divided into $N_\Theta \times N_\Phi$ regions, using an equally spaced $(\cos\Theta, \Phi)$ grid (Θ is the magnetic colatitude, Φ is the magnetic longitude). With such a geometrical structure all patches have the same area, and as a result the number of emitting photons depends only on the patch temperature.
Photons so generated produce resonant cyclotron scattering with electrons moving along the magnetic field lines. The mean distance between two successive interactions is defined as l, and can be directly estimated by the scattering depth $\tau_s = \int_0^l d\tau_s = -\ln U$, where the indices s represent the photon polarization state ($s = 1$ for ordinary mode, and $s = 2$ for extraordinary mode), while U is the uniform deviate.
In order to solve the kinematics of the scattering, the knowledge of the resonant electron velocity β_k is required.

It is possible that some photons rich the surface again after a certain number of interactions. The number of these photons is, however, very poor with respect to the total of the emitting photons, so their loss has be neglected.

Each scattering modifies the photon energy, so that, when escaping photons are collected, their spectra result harded than a pure thermal one.

The photon collection take place on a spherical surface located sufficently far away to consider the star as point-like. Photons escaping from the magnetosphere are collected on a spherical surface (the "sky") which is divided into $N_{\Theta_s} \times N_{\Phi_s}$ patches, similarly to what has been done done for the star surface.

Counts are stored in a 3-D array (first two indices labelled the position in the sky, while the third identify the photon energy). Each model obtained is also characterized by the magnetospheric twist $\Delta\phi_{N-S}$, the electron (constant) bulk velocity β, and the seed photon temperature kT. Montecarlo models are computed (and stored) for the simplest geometrical case, in which the spin and the magnetic axes are aligned.

As discussed in NTZ, the most general situation in which the spin and magnetic axes are at an arbitrary angle ξ can be treated at the post-production level. If χ is the inclination of the line-of-sight (LOS) with respect to the star spin axis and α the rotational phase angle, the co-ordinates of the points where the LOS intersects the sky can be found in terms of ξ, χ and α (see Fig 2.3). Starting from the stored montecarlo models, it is possible to draw the pulse profile in any given energy band, simply by integrating over the selected range the energy-dependent counts at these positions as

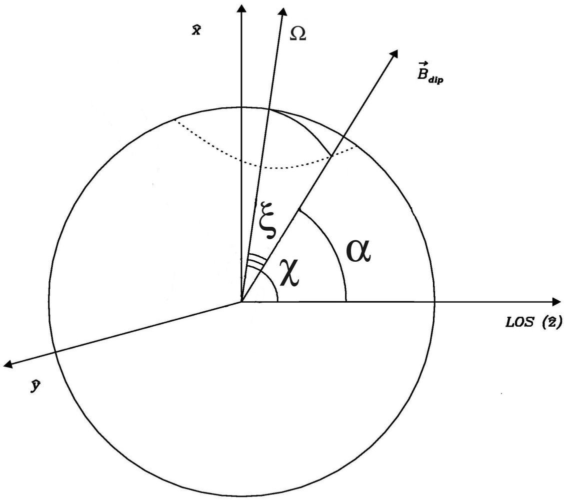

Figure 2.3: *General configuration for χ, ξ and α .*

the star rotates (see again NTZ for details). In order to compare model lightcurves with observations, integration over energy is performed accounting for both interstellar absorption and the detector response function. Actually, the interstellar absorption cross-section σ and the response function A depend on the photon energy at infinity $\bar{E} = E\sqrt{1 - R_S/R_{NS}}$, where E is the energy in the star frame (which is used in the Montecarlo calculation) and R_S is the Schwarzschild radius ($R_{NS} = 10$ km and $M_{NS} = 1.44\ M_\odot$). The pulse profile in the $[\bar{E}_1,\ \bar{E}_2]$ energy band is then

$$\propto \int_{\bar{E}_1}^{\bar{E}_2} d\bar{E}\ \exp\left[-N_H\sigma(\bar{E})\right]A(\bar{E})N(\alpha, E) \tag{2.16}$$

where N_H is the hydrogen column density and $N(\alpha, E)$ is the energy-dependent count rate. Also phase-averaged spectra can be computed, starting from montecarlo models, by summing over all phases the energy-dependent counts. Note that it is $0 \leq \xi \leq \pi/2$, while χ is in the range $[0, \pi]$ because of the asymmetry between the north and south magnetic poles introduced by the current flow.

In the applications below Morrison, & McCammon (1983) model for interstellar absorption was used and since we deal with *XMM-Newton* observations, the EPIC-pn response function was adopted. A part from gravitational redshift, no general-relativistic correction was included (see Zane & Turolla, 2006, for a more detailed discussion).

Chapter 3

XTE J1810-197

In the previous chapter the NTZ montecarlo model has been briefly described. Here and in the next chapter, adapted from Albano et al. (2010), the resonant compton scattering model has been applied to reproduce the pulse profiles and the phase-averaged spectra (and their time evolution) of the two Transient AXPs XTE J1810-197 and CXOU J164710.2-455216. The choice to analyze both pulse profiles and spectra has several motivations. The main one (see also Zane et al., 2009) is that spectral fitting alone is unable to constrain the two geometrical angles χ and ξ. Moreover, lightcurve fitting allows for a better control in the case in which the surface thermal map is complex and changes in time (see below).
We started by fitting the observed pulse profiles in different energy bands (total: 0.5 keV $\leq E \leq$ 10 keV, soft: 0.5 keV $\leq E \leq$ 2 keV, hard: 2 keV $\leq E \leq$ 10 keV) with the synthetic ones calculated as discussed in Sect 2.4. The procedure provides an estimate of the model parameters ($\Delta\phi$, β and T), including the two geometrical angles ξ and χ. While the twist angle, electron velocity and surface temperature may vary in the different observations (although they must be the same in the different energy bands for a given observation), the fits have to produce values of ξ and χ which are at all epochs compatible within the errors in order to be satisfactory. Afterwards the phase-averaged spectra for the two sources at the various epochs for the same sets of parameters have been computed and compared with the observed ones.

For the present investigation, a model archive has been generated beforehand. Each model has been computed by evolving $N_{patch} = 225,000$ photons for $N_\Theta \times N_\Phi = 8 \times 4 = 32$ surface patches ($N_{tot} = 7.2 \times 10^6$ photons). The magnetic field has been fixed at the value of 10^{14} G. The parameter grids are: $0.1 \leq kT \leq 0.9$ keV (step 0.05 keV),

$0.1 \leq \beta \leq 0.9$ (step 0.1) and $0.2 \leq \Delta\phi \leq 1.2$ rad (step 0.1 rad). Photons are collected on a $N_{\Theta_s} \times N_{\Phi_s} = 10 \times 10 = 100$ angular grid on the sky, and in $N_E = 50$ energy bins equally spaced in $\log E$ in the range $0.1 - 100$ keV.

In the following sections the application of the model to the TAXP XTE J1810-197 will be presented. To do this eight *XMM-Newton* EPIC-PN observations have been considered, covering the period September 2003 - September 2007 (see Table 3.1 for the observation log). The procedure can be summarized as follows: first of all the principal component analysis (PCA) has been used to explore the properties of the lightcurves as a population and to select the model pulse profile within the archive that is closest to the observed one at a given epoch. This serves as the starting point for the pulse profile fitting procedure, which has been performed assuming that the whole star surface is at the same temperature. The fitting is then repeated first for the case in which the surface thermal distribution consists of a hot spot and a cooler region, and then by generating a new archive with a finer surface gridding, and applying it in the case of a surface thermal map consisting of a hot spot, a warm corona and a cooler region. Finally, the source parameters derived from the lightcurve fitting are used to confront the model and observed spectra.

Label	OBS ID	Epoch	Exposure time (s)
Sep03	0161360301	2003-09-08	1.2113E+04
Sep04	0164560601	2004-09-18	2.8913E+04
Mar05	0301270501	2005-03-18	4.2213E+04
Sep05	0301270401	2005-09-20	4.2252E+04
Mar06	0301270301	2006-03-12	5.1398E+04
Sep06	0406800601	2006-09-24	5.0303E+04
Mar07	0406800701	2007-03-06	6.8308E+04
Sep07	0504650201	2007-09-16	7.4938E+04

Table 3.1: *XMM-Newton EPIC-PN instrument observation log for XTE J1810-197*

3.1 Principal Component Analysis

The principal component analysis is a method of multivariate statistics that allows to reduce the number of variables X_i needed to describe a data set by introducing a new set variables, the principal components (PCs) Z_i. The PCs are linear combinations of the original variables and are such that Z_1 displays the largest variance, Z_2 the second

largest, and so on. By using the PCs it is possible to describe the data set in terms of a limited number of variables, which however, carry most of the information contained in the original sample (see e.g. Zane & Turolla, 2006, and references therein).
Synthetic lightcurves have been generated for 32 phases in the range $[0, 2\pi]$ and for a 9×9 angular grid, $0° \leq \xi \leq 90°$ (step 10°), $0° \leq \chi \leq 180°$ (step 20°); the archive contains a total of 136323 models. Once the PCA has been applied to the lightcurve set, it has been found that the first three PCs (Z_1, Z_2, Z_3) accounts for as much as $\sim 90\%$ of the sample variance. This means that the entire set is satisfactory described in terms of just three variables instead of the original 32 (see Zane & Turolla, 2006, for an interpretation of Z_1, Z_2, Z_3).
First of all it has been verified if there is a combination of the parameters for which synthetic pulse profiles reproduce the data. In Fig. 3.1 a graphic representation of all the lightcurves in the archive in terms of the first three PCs is shown, togheter with the PC representation of XTE J1810-197 pulse profiles at the various epochs. The source PCs fall within the volume occupied by models.
A search for the minimum of the Euclidean distance $\sum_{i=1}^{32}(Z_i - Z_i^{obs})^2$ between the model and the observed pulse profile has been performed for every observation, enabling us to identify the model in the archive which is closest to a given observed lightcurve.

3.2 Emission from all the surface

Once the model closest to each observation (and in each band) has been found through the PCA, a fit was performed using an IDL script based on the minimization routine `mpcurvefit.pro`. In this preliminarly analysis the simplest assumption about the star surface thermal map has been done, i.e. an uniform distribution at temperature T. Lightcurves were then computed in the total $(0.5 - 10$ keV), soft $(0.5 - 2$ keV) and hard $(2 - 10$ keV) energy bands for all the models in the archive. The minimization involves a total of six free parameters: the temperature T, the electron bulk velocity β, the twist angle $\Delta\phi$, the misalignement between magnetic and spin axes ξ, the LOS direction χ, and the initial phase. The last parameter has been added to account for the indetermination in the position of the pulse peak. Lightcurves were normalized to the phase averaged count rate. Since it is not possible to compute "on the fly" the pulse profile for a set of parameters different from those contained in the archive, in the minimization process lightcurves were obtained from those in the archive using a

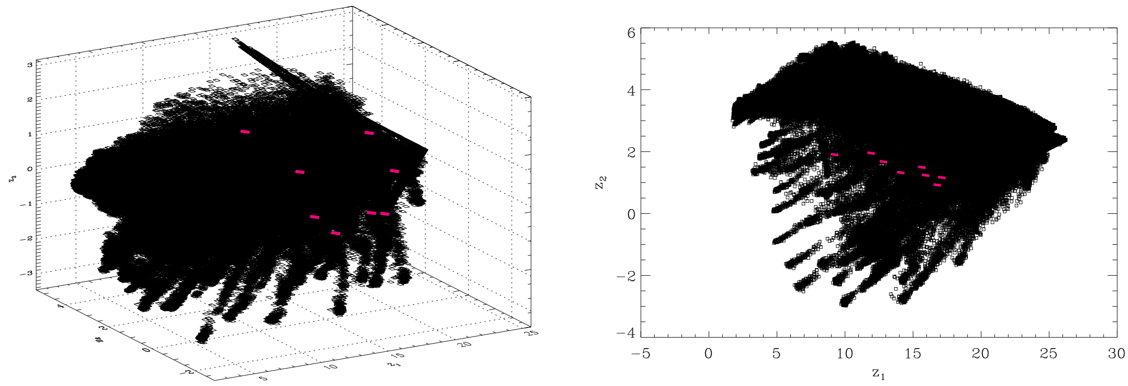

(a) Z1-Z2-Z3 (b) Z1-Z2

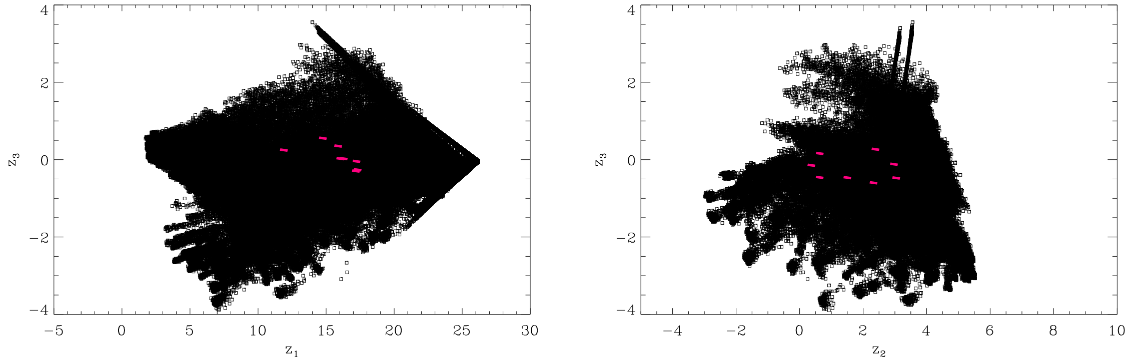

(c) Z1-Z3 (d) Z2-Z3

Figure 3.1: *Principal component representation of the simulated lightcurves in our archive (black dots) together with the observed lightcurves of XTE J1810-197 (red dots). All the pulse profiles refer to the 0.5-10 keV band.*

linear interpolation in the parameter space.
The best-fitting parameters for all XTE J1810-197 observations in the three energy bands are listed in Tabs. 3.2, 3.3 and 3.4, and the parameters evolution for all the energy bands is plotted in Fig. 3.2. 1σ errors for all parameters are obtained from the minimization routine. Note that for the hard band the analysis stops after the September 2006 observation. This is because in both 2007 observations photons with energy greater than 2 keV are very few and, as a consequence, lightcurves are affected by large incertainities.

Note that for both 2007 observations the temperature is compatible, within the errors, with the ROSAT quiescent temperature of XTE J1810-197 (0.15 keV; see sect. 1.3.1 for details). Fig. 3.2 shows that the values of the physical parameters ($\Delta\phi$, β, T) turn out to be the same (within the errors) for a given epoch among the different energy bands, as it needs to be. Moreover, the evolution of the twist angle and of the

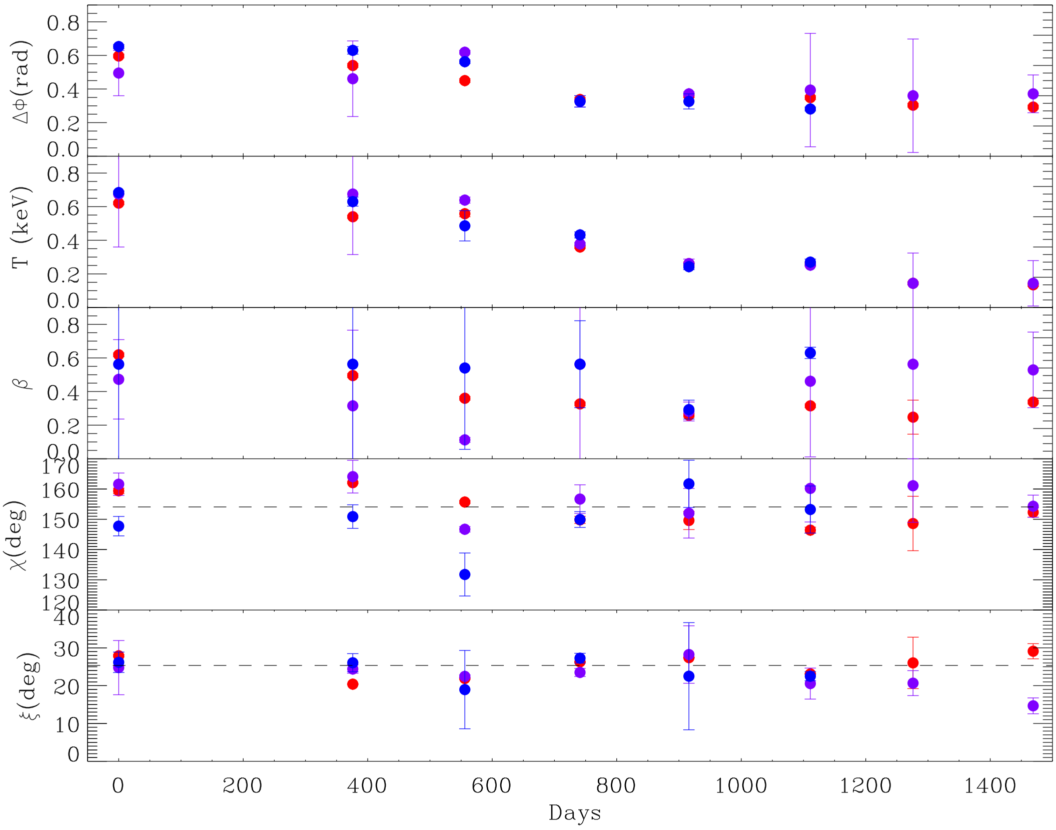

Figure 3.2: *Parameters evolution for XTE J1810-197 (uniform surface temperature); results refer to the three energy bands: red dots are for the total, liliac dots for the soft and blue dots for the hard. Time is computed starting from the September 2003 observation.*

Label	$\Delta\phi$ (rad)	T (keV)	β	ξ(deg)	χ (deg)
Sep03	0.73 ± 0.01	0.69 ± 0.01	0.75 ± 0.01	27.9 ± 0.3	159.4 ± 0.9
Sep04	0.68 ± 0.01	0.60 ± 0.01	0.64 ± 0.01	20.4 ± 0.1	162.1 ± 0.3
Mar05	0.60 ± 0.01	0.62 ± 0.02	0.52 ± 0.01	21.9 ± 0.2	155.7 ± 0.5
Sep05	0.50 ± 0.01	0.40 ± 0.01	0.49 ± 0.01	26.3 ± 0.1	149.8 ± 1.2
Mar06	0.52 ± 0.01	0.29 ± 0.01	0.43 ± 0.01	27.4 ± 0.1	149.6 ± 3.0
Sep06	0.51 ± 0.01	0.29 ± 0.01	0.48 ± 0.01	23.1 ± 0.1	146.4 ± 1.0
Mar07	0.47 ± 0.01	0.16 ± 0.01	0.42 ± 0.09	26.0 ± 6.8	148.6 ± 9.0
Sep07	0.46 ± 0.01	0.15 ± 0.01	0.50 ± 0.01	29.1 ± 2.0	152.3 ± 1.6

Table 3.2: *Parameters set for the total band with uniform temperature*

Label	$\Delta\phi$ (rad)	T (keV)	β	ξ(deg)	χ (deg)
Sep03	0.64 ± 0.12	0.75 ± 0.35	0.62 ± 0.21	24.8 ± 7.2	161.6 ± 3.7
Sep04	0.61 ± 0.20	0.75 ± 0.40	0.48 ± 0.40	24.4 ± 1.1	164.1 ± 5.4
Mar05	0.75 ± 0.01	0.71 ± 0.02	0.30 ± 0.01	22.5 ± 0.4	146.7 ± 0.9
Sep05	0.49 ± 0.03	0.42 ± 0.01	0.70 ± 0.67	23.5 ± 1.1	156.7 ± 4.7
Mar06	0.53 ± 0.01	0.29 ± 0.03	0.45 ± 0.05	28.2 ± 7.6	152.0 ± 8.2
Sep06	0.55 ± 0.30	0.28 ± 0.01	0.61 ± 0.40	20.6 ± 4.1	160.2 ± 11.1
Mar07	0.52 ± 0.30	0.16 ± 0.20	0.70 ± 0.50	20.7 ± 3.3	161.1 ± 12.1
Sep07	0.53 ± 0.10	0.16 ± 0.15	0.67 ± 0.20	14.7 ± 2.1	154.3 ± 3.7

Table 3.3: *Parameters set for soft band with uniform temperature*

Label	$\Delta\phi$ (rad)	T (keV)	β	ξ(deg)	χ (deg)
Sep03	0.78 ± 0.01	0.76 ± 0.01	0.70 ± 0.61	26.2 ± 2.7	147.7 ± 3.2
Sep04	0.76 ± 0.02	0.70 ± 0.03	0.70 ± 0.60	26.1 ± 2.4	150.9 ± 3.9
Mar05	0.70 ± 0.01	0.54 ± 0.10	0.68 ± 0.43	19.0 ± 10.4	131.7 ± 7.1
Sep05	0.49 ± 0.03	0.48 ± 0.02	0.70 ± 0.23	27.3 ± 1.3	149.9 ± 2.6
Mar06	0.49 ± 0.04	0.27 ± 0.02	0.46 ± 0.05	22.5 ± 14.2	161.7 ± 7.8
Sep06	0.45 ± 0.01	0.30 ± 0.02	0.76 ± 0.03	22.5 ± 1.2	153.2 ± 7.8

Table 3.4: *Parameters set for hard band with uniform temperature*

surface temperature follows a quite reasonable trend, with both quantities decreasing in time during the outburst decline. This is expected if the outburst is a consequence of a sudden change in the NS magnetic structure, producing both a heating of the star surface layers and a twisting of the magnetosphere which then dies away (Thompson, Lyutikov, & Kulkarni, 2002; Beloborodov, 2009). However, the model is not satisfactory since the geometrical angles χ and ξ change significantly from one observation to another, and even for the same observation in the different energy bands. This is most probably due to the oversimplifying assumption about the neutron star thermal map.

3.3 Emission from two regions

Starting from results obtained assuming emission from all the surface at the same temperature, and considering models proposed by other authors (Perna & Gotthelf 2008, Bernardini et al. 2009, see again sect. 1.3.1 for details), a different configurations has been investigated, characterized by a more complex thermal distribution: a two temperature map with a hot cap centered on one magnetic pole while the rest of the surface is cooler.

In this picture both temperatures may vary with time, as well as the emitting areas. In order to avoid complicating too much the minimization routine, one temperature has been let free to vary while the other one was freezed. Minimizations for each observation and energy band have been repeated for ten times, everytime with a different hot spot area value: $A_h = 0.78\%$, 1.56%, 3.12%, 6.25%, 9.37%, 12.5%, 15.62%, 18.75%, 21.87%, 25% (in terms of the total surface). The emitting area size has been chosen in order to minimize the reduced χ^2 value. Moreover it has been imposed that, for every observation, the emitting area chosen has to be the same in the three energy bands.

From experimenting with the one temperature model we know that, in both 2007 observations, all the star radiates at the same (constant) temperature ($T_c \sim 0.15$ keV), comparable to the quiescent one. So we started from the September 2007 observation, freezing the colder temperature at $T_c = 0.15$ keV, and letting free to vary the hot spot temperature T_h. Independently on the emitting area chosen, we always found for T_h a value compatible with ~ 0.15 keV for both the September and March 2007 observations. One can then conclude that for these two cases all the star is radiating at the same temperature, or if a hot cap exists, its area is smaller than 1.56% of the star surface (the smallest surface grid resolution). For the other six observations (from September 2003 till September 2006), as well as described for areas, different fits have been tried, changing both the emitting areas (as previously discussed) and the temperature of the cold region. For the latter four values have been used: 0.15, 0.20, 0.25, 0.30 keV. We required that T_c remains the same for each observation in the three energy bands.

The two temperature model improves the fit reduced χ^2 (see Tab. 3.17), but the variations of the geometric angles, albeit reduced, are still present. Results for the fits are reported in Tabs. 3.5, 3.6, 3.7, 3.8, 3.9 and 3.10 and showed in Figs. 3.3, 3.4. Again, 1 σ errors for all parameters are obtained from the minimization routine. On the contrary 1 σ errors for the emitting area size have been chosen as two times the smallest surface grid resolution.

Label	$\Delta\phi$ (rad)	β	ξ(deg)	χ (deg)
Sep03	0.70 ± 0.01	0.80 ± 0.01	22.7 ± 0.5	144.2 ± 0.6
Sep04	0.67 ± 0.01	0.62 ± 0.02	20.7 ± 1.0	158.2 ± 0.2
Mar05	0.61 ± 0.01	0.49 ± 0.01	21.6 ± 0.4	147.1 ± 0.6
Sep05	0.47 ± 0.01	0.53 ± 0.05	23.0 ± 0.1	159.0 ± 1.1
Mar06	0.49 ± 0.01	0.50 ± 0.11	23.5 ± 0.4	149.4 ± 3.5
Sep06	0.43 ± 0.01	0.71 ± 0.16	21.4 ± 0.3	155.7 ± 1.7
Mar07	0.45 ± 0.01	0.6 ± 0.01	29.8 ± 0.1	162.8 ± 0.1
Sep07	0.48 ± 0.01	0.70 ± 0.08	22.4 ± 0.1	163.0 ± 1.7

Table 3.5: *Parameters set for the total band, two temperature model.*

Label	$T_h(keV)$	$A_h(\%)$	$T_w(keV)$	$A_w(\%)$
Sep03	0.71 ± 0.01	6.25 ± 1.56	0.30	93.75 ± 1.56
Sep04	0.55 ± 0.01	4.69 ± 1.56	0.30	95.31 ± 1.56
Mar05	0.67 ± 0.01	3.12 ± 1.56	0.25	96.88 ± 1.56
Sep05	0.42 ± 0.01	1.56 ± 1.56	0.25	98.44 ± 1.56
Mar06	0.28 ± 0.01	0.78 ± 1.56	0.15	99.22 ± 1.56
Sep06	0.28 ± 0.01	0.78 ± 1.56	0.15	99.22 ± 1.56
Mar07	–	–	0.16 ± 0.01	100
Sep07	–	–	0.15 ± 0.01	100

Table 3.6: *Thermal map for the total band, two temperature model. Where no error was reported the temperature was kept fixed.*

Label	$\Delta\phi$ (rad)	β	ξ(deg)	χ (deg)
Sep03	0.78 ± 0.17	0.76 ± 0.03	19.5 ± 4.7	155.3 ± 6.8
Sep04	0.72 ± 0.16	0.57 ± 0.04	11.3 ± 4.3	152.1 ± 8.5
Mar05	0.89 ± 0.17	0.78 ± 0.11	19.1 ± 1.1	144.8 ± 0.7
Sep05	0.46 ± 0.04	0.44 ± 0.23	22.7 ± 6.7	146.8 ± 0.9
Mar06	0.48 ± 0.01	0.50 ± 0.08	17.2 ± 1.2	146.8 ± 1.0
Sep06	0.48 ± 0.21	0.53 ± 0.14	19.5 ± 3.1	159.1 ± 13.0
Mar07	0.52 ± 0.03	0.70 ± 0.58	20.7 ± 3.4	161.1 ± 20.0
Sep07	0.53 ± 0.24	0.67 ± 0.18	14.7 ± 1.1	154.3 ± 6.6

Table 3.7: *Parameters set for soft band, two temperature model.*

3.4 Emission from three regions

Following the suggestion by Bernardini et al. 2009 (see sect.1.3.1 for details), according to whom the star surface comprises three regions at different temperatures, we decided to introduce a three temperature surface thermal map.

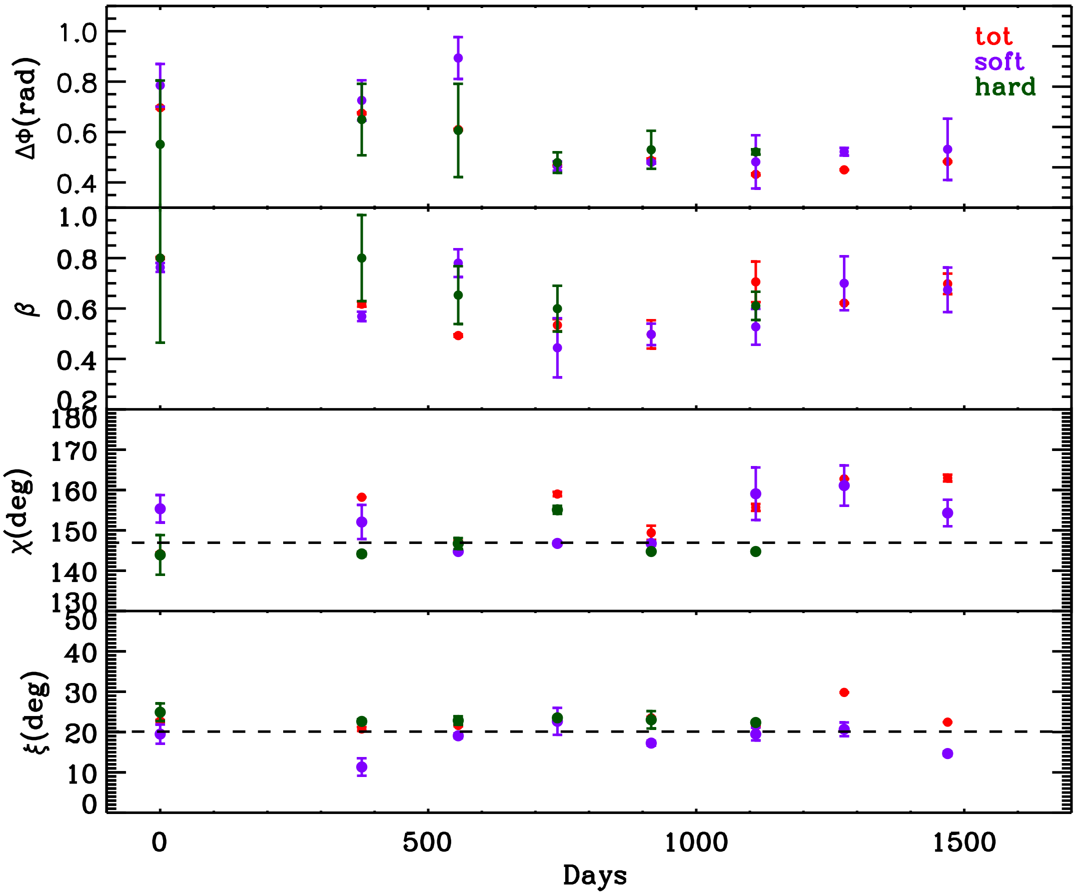

Figure 3.3: *Parameters evolution with time. Results refer to the three energy bands: red dots are for the total band, liliac dots are for the soft band and blue dots are for the hard band. Time is in days from the September 2003 observation.*

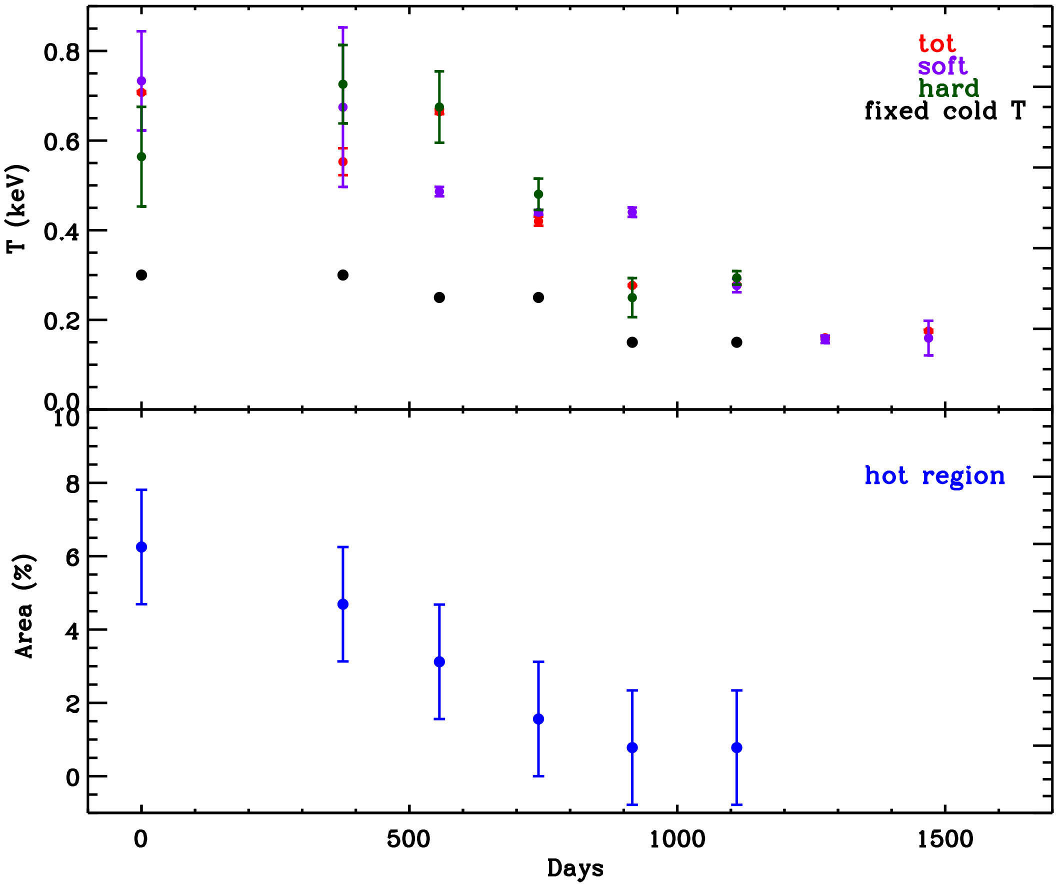

Figure 3.4: *Same as in Fig. 3.3 for the thermal map evolution with time.*

Label	$T_h(keV)$	$A_h(\%)$	$T_w(keV)$	$A_w(\%)$
Sep03	0.73 ± 0.22	6.25 ± 1.56	0.30	93.75 ± 1.56
Sep04	0.67 ± 0.36	4.69 ± 1.56	0.30	95.31 ± 1.56
Mar05	0.49 ± 0.02	3.12 ± 1.56	0.25	96.88 ± 1.56
Sep05	0.44 ± 0.01	1.56 ± 1.56	0.25	98.44 ± 1.56
Mar06	0.44 ± 0.02	0.78 ± 1.56	0.15	99.22 ± 1.56
Sep06	0.28 ± 0.03	0.78 ± 1.56	0.15	99.22 ± 1.56
Mar07	–	–	0.16 ± 0.20	100
Sep07	–	–	0.16 ± 0.15	100

Table 3.8: *Thermal map for the soft band, two temperature model. Where no error was reported the temperature was kept fixed.*

Label	$\Delta\phi$ (rad)	β	ξ(deg)	χ (deg)
Sep03	0.55 ± 0.51	0.80 ± 0.67	24.9 ± 4.4	143.9 ± 9.8
Sep04	0.65 ± 0.28	0.80 ± 0.34	22.6 ± 1.1	144.2 ± 1.1
Mar05	0.61 ± 0.37	0.65 ± 0.23	22.9 ± 2.1	146.7 ± 2.7
Sep05	0.48 ± 0.08	0.60 ± 0.18	23.5 ± 0.8	155.1 ± 2.0
Mar06	0.53 ± 0.08	0.10 ± 0.02	23.0 ± 4.3	144.8 ± 0.2
Sep06	0.52 ± 0.02	0.61 ± 0.11	22.4 ± 0.9	144.8 ± 0.2

Table 3.9: *Parameters set for hard band, two temperature model.*

Label	$T_h(keV)$	$A_h(\%)$	$T_w(keV)$	$A_w(\%)$
Sep03	0.56 ± 0.22	6.25 ± 1.56	0.30	93.75 ± 1.56
Sep04	0.73 ± 0.17	4.69 ± 1.56	0.30	95.31 ± 1.56
Mar05	0.67 ± 0.16	3.12 ± 1.56	0.25	96.88 ± 1.56
Sep05	0.48 ± 0.07	1.56 ± 1.56	0.25	98.44 ± 1.56
Mar06	0.25 ± 0.09	0.78 ± 1.56	0.15	99.22 ± 1.56
Sep06	0.29 ± 0.03	0.78 ± 1.56	0.15	99.22 ± 1.56

Table 3.10: *Thermal map for the hard band, two temperature model.*

Since the montecarlo archive used for the first analysis has a limit in the area resolution, a new model archive has been generated, increasing the number of surface patches to $N_\Theta \times N_\Phi = 50 \times 4 = 200$. Every patch emits $150,000$ photons, so that all the neutron star is actually emitting 3×10^7 photons. The temperature, electron velocity and twist angle are in the range 0.15 keV $\leq T \leq 0.9$ keV (step 0.15 keV), $0.1 \leq \beta \leq 0.9$ (step 0.2) and $0.4 \leq \Delta\phi \leq 1.2$ rad (step 0.2 rad), respectively.

The neutron star surface has been divided into three zones: a hot spot centered on the magnetic axis at temperature T_h, a concentric warm corona at T_w and the remaining part of the neutron star surface at T_c. Again, information from the previous modellization (one and two-temperature cases) are used as a starting point for the analysis. In both one and two-temperature models the last two observations are characterized by emission at the same (constant) temperature ($T_c \sim 0.15$ keV), comparable to the quiescent one. As previously done for the two temperature model, this new analysis starts from 2007 observations, fixing $T_c = 0.15$ keV, and searching for the value of the warm temperature T_w. Every fit has been repeated for twelve values of the emitting area: A_w = 0.5%, 1%, 2%, 4%, 6%, 8%, 10%, 12%, 14%, 16%, 18%, 20% (in terms of the total surface). Since with the new montecarlo archive the area resolution has increased, the lightcurve reduced χ^2 improves with the addition of a warm spot at the temperature $T_w \sim 0.3$ keV, accounting for 0.5% of the neutron star surface (see Tab. 3.17).

From the two temperature model we also know that in both 2006 observations T_c is fixed to the value of 0.15 keV while $T_w \sim 0.3$ keV. So also for these two observations $T_c = 0.15$ keV is fixed and T_w is let free to vary. The size of the emitting area was estimated following the same procedure discussed above. As a result an almost constant value, $T_w \sim 0.3$ keV has been found, between March 2006 and September 2007, with an emitting area that decreases with time. The previous modelization shows that the hotter temperature in the period between September 2003 and Semptember 2005 is greater than 0.3 keV, while the colder one varies between 0.25 and 0.30 keV. In order to obtain the parameters set for these first four observations the coldest temperature has been fixed to $T_c = 0.15$ keV while the warmer one has been fixed to $T_w = 0.3$ keV, so that the hotter temperature was the only one to vary. For every observation fits are repeated for twelve values of the hot spot area: A_h = 0.5%, 1%, 2%, 4%, 6%, 8%, 10%, 12%, 14%, 16%, 18%, 20% (in terms of the total surface) and for the same values of the warm corona area.

Results for lightcurves fitting at different epochs are reported in Tabs. 3.11, 3.12, 3.13, 3.14, 3.15 and 3.16 and shown in Figs. 3.5 and 3.6.

Parameter errors, in this case, have been estimated using the costant reduced χ^2 boundaries method, according to which, if k_0 is a minimization parameter and χ^2_{min} is the minimum value for the chi-squared, then reduced χ^2 increase every time k_0 is perturbed. The region within which reduced χ^2 increases by no more than a given amount $\Delta\chi^2$ defines some closed M-dimentional confidence region around k_0 (M is the number of free parameters). There are three $\Delta\chi^2$ values for which the probability to find the true value in a region around χ^2_{min} is, respectively, 68%, 95.54% and 99.97%. Parameter

Epoch	$\Delta\phi(rad)$	β	$\chi(^\circ)$	$\xi\ (^\circ)$
Sep 03	$0.80^{+0.05}_{-0.11}$	$0.70^{+0.08}_{-0.06}$	$27.8^{+4.6}_{-3.1}$	$145.3^{+4.7}_{-2.5}$
Sep 04	$0.79^{+0.07}_{-0.08}$	$0.78^{+0.09}_{-0.23}$	$16.2^{+4.2}_{-5.9}$	$140.8^{+5.8}_{-2.6}$
Mar 05	$0.62^{+0.03}_{-0.03}$	$0.51^{+0.07}_{-0.09}$	$22.2^{+5.4}_{-13.1}$	$146.9^{+7.9}_{-1.8}$
Sep 05	$0.53^{+0.10}_{-0.09}$	$0.50^{+0.11}_{-0.19}$	$21.4^{+10.3}_{-20.0}$	$154.4^{+13.9}_{-9.5}$
Mar 06	$0.46^{+0.08}_{-0.04}$	$0.73^{+0.20}_{0.20}$	$18.5^{18.0}_{-17.2}$	$143.0^{+7.9}_{-7.5}$
Sep 06	$0.54^{+0.04}_{-0.03}$	$0.42^{+0.13}_{-0.12}$	$22.4^{+12.3}_{-20.0}$	$150.2^{+14.3}_{-9.5}$
Mar 07	$0.49^{+0.20}_{-0.05}$	$0.43^{+0.13}_{-0.12}$	$30.0^{+12.3}_{-20.0}$	$153.9^{+19.6}_{-16.0}$
Sep 07	$0.47^{+0.07}_{-0.04}$	$0.50^{+0.09}_{-0.15}$	$22.7^{+16.4}_{-20.0}$	$145.8^{+16.4}_{-9.5}$

Table 3.11: *XTE J1810-197 parameters for total band, three temperature model.*

Epoch	$T_h(keV)$	$T_w(keV)$	$T_c(keV)$	$A_h(\%)$	$A_w(\%)$
Sep 03	$0.62^{+0.14}_{-0.14}$	0.30	0.15	$8. \pm 1.$	$16. \pm 1.$
Sep 04	$0.49^{+0.03}_{-0.22}$	0.30	0.15	$6. \pm 1.$	$14. \pm 1.$
Mar 05	$0.49^{+0.01}_{-0.04}$	0.30	0.15	$4. \pm 1.$	$14. \pm 1.$
Sep 05	0.52^{---}_{---}	0.30	0.15	$2. \pm 1.$	$10. \pm 1.$
Mar 06	-	$0.29^{+0.17}_{-0.03}$	0.15	-	$6. \pm 1.$
Sep 06	-	0.27^{---}_{---}	0.15	-	$2. \pm 1.$
Mar 07	-	0.30	$0.19^{+0.27}_{---}$	-	$0.5 \pm 1.$
Sep 07	-	0.30	$0.18^{+0.23}_{---}$	-	$0.5 \pm 1.$

Table 3.12: *XTE J1810-197 thermal map parameters for total band, three temperature model (hot temperature value for Sep 05 and warm temperature value for Sep 06 observations come from the spectral analysis).*

values for these particular $\Delta\chi^2$ represent $1, 2, 3$ σ errors (in general lower and higher values for every confidence level may be different). This new thermal map strongly improves the lightcurve reduced χ^2 (see Tab. 3.17). Most importantly of all, the ge-

Epoch	$\Delta\phi(rad)$	β	$\chi(^\circ)$	$\xi\ (^\circ)$
Sep 03	$0.80^{+0.06}_{-0.10}$	$0.70^{+0.05}_{-0.08}$	$26.9^{+4.2}_{-6.7}$	$147.2^{+0.8}_{-6.8}$
Sep 04	$0.77^{+0.11}_{-0.08}$	$0.70^{+0.08}_{-0.26}$	$17.9^{+5.4}_{-6.3}$	$150.2^{+4.4}_{-4.8}$
Mar 05	$0.59^{+0.15}_{-0.11}$	$0.45^{+0.10}_{-0.10}$	$21.3^{+11.5}_{-11.5}$	$148.7^{+5.4}_{-7.5}$
Sep 05	$0.50^{+0.05}_{-0.01}$	$0.52^{+0.08}_{-0.11}$	$22.3^{+6.9}_{-23.0}$	$154.9^{+19.6}_{-8.3}$
Mar 06	$0.5^{+0.04}_{-0.01}$	$0.45^{+0.22}_{-0.16}$	$28.3^{+6.3}_{-26.9}$	$151.8^{+15.4}_{-10.9}$
Sep 06	$0.52^{+0.09}_{-0.07}$	$0.70^{+0.12}_{-0.10}$	$16.9^{+6.7}_{-13.5}$	$156.6^{+7.5}_{-5.9}$
Mar 07	$0.0.53^{+0.09}_{-0.06}$	$0.49^{+0.19}_{-0.16}$	$18.0^{+10.3}_{-20.0}$	$152.5^{+13.5}_{-7.9}$
Sep 07	$0.0.51^{+0.05}_{-0.05}$	$0.47^{+0.17}_{-0.14}$	$20.5^{+19.6}_{-13.9}$	$141.6^{+11.1}_{-8.7}$

Table 3.13: *XTE J1810-197 parameters for soft band, three temperature model.*

Epo	$T_h(keV)$	$T_w(keV)$	$T_c(keV)$	$A_h(\%)$	$A_w(\%)$
Sep03	$0.58^{+0.06}_{-0.20}$	0.30	0.15	$8. \pm 1.$	$16. \pm 1.$
Sep04	$0.52^{+0.24}_{-0.25}$	0.30	0.15	$6. \pm 1.$	$14. \pm 1.$
Mar05	0.50^{---}_{---}	0.30	0.15	$4. \pm 1.$	$14. \pm 1.$
Sep05	0.52^{---}_{---}	0.30	0.15	$2. \pm 1.$	$10. \pm 1.$
Mar06	-	$0.30^{+0.09}_{-0.11}$	0.15	-	$6. \pm 1.$
Sep06	-	0.27^{---}_{---}	0.15	-	$2. \pm 1.$
Mar07	-	0.30	$0.19^{+0.01}_{---}$	-	$0.5 \pm 1.$
Sep 07	-	0.30	$0.18^{+0.02}_{---}$	-	$0.5 \pm 1.$

Table 3.14: *XTE J1810-197 thermal map parameters for soft band, three temperature model (hot temperature value for Sep 05 and warm temperature value for Sep 06 observations come from the spectral analysis)*

ometrical angles χ and ξ remain constant, within 1σ errors, both in different energy bands and during time. 1σ errors for the size of the emitting area are, again, defined as two times the smallest surface grid resolution.

Epoch	$\Delta\phi(rad)$	β	$\chi(°)$	ξ (°)
Sep 03	$0.80^{+0.07}_{-0.11}$	$0.71^{+0.05}_{-0.04}$	$30.0^{+4.6}_{-5.0}$	$141.1^{+3.0}_{-4.2}$
Sep 04	$0.78^{+0.08}_{-0.09}$	$0.71^{+0.06}_{-0.04}$	$23.9^{+4.2}_{-5.9}$	$142.1^{+4.8}_{-3.4}$
Mar 05	$0.63^{+0.04}_{-0.02}$	$0.58^{+0.10}_{-0.04}$	$26.1^{+5.6}_{-21.1}$	$142.8^{+8.6}_{-2.7}$
Sep 05	$0.45^{+0.09}_{-0.01}$	$0.70^{+0.08}_{-0.08}$	$18.4^{+6.7}_{-20.0}$	$155.5^{+11.1}_{-6.3}$
Mar 06	$0.49^{+0.12}_{-0.07}$	$0.52^{+0.02}_{-0.02}$	$22.4^{+18.8}_{-20.0}$	$143.1^{+24.6}_{-9.3}$
Sep 06	$0.58^{+0.08}_{-0.08}$	$0.58^{+0.01}_{-0.03}$	$22.4^{+15.6}_{-20.0}$	$150.4^{+14.7}_{-13.5}$

Table 3.15: *XTE J1810-197 parameters for hard band, three temperature model*

Epo	$T_h(keV)$	$T_w(keV)$	$T_c(keV)$	$A_h(\%)$	$A_w(\%)$
Sep03	$0.57^{+0.20}_{-0.15}$	0.30	0.15	8. ± 1.	16. ± 1.
Sep04	$0.50^{+0.09}_{-0.08}$	0.30	0.15	6. ± 1.	14. ± 1.
Mar05	$0.50^{+0.14}_{-0.15}$	0.30	0.15	4. ± 1.	14. ± 1.
Sep05	0.52^{---}_{----}	0.30	0.15	2. ± 1.	10. ± 1.
Mar06	-	0.28^{---}_{---}	0.15	-	6. ± 1.
Sep06	-	0.27^{---}_{---}	0.15	-	2. ± 1.

Table 3.16: *XTE J1810-197 thermal map parameters for hard band, three temperature model (hot temperature value for Sep 05 and warm temperature value for Sep 06 observations come from the spectral analysis)*

Results obtained for the TAXP XTE J1810-197 can be summarized as follows: according to our model the AXP is seen at an angle $\chi = 148^{+7\circ}_{-9}$ with respect to the spin axis. The misalignment between the spin axis and the magnetic axis is $\xi = 23^{+15\circ}_{-11}$. We calculated the probability that values for the two geometrical angles χ and ξ were not costant during time, finding a value of 0.19% for ξ and 0.63% for χ.

Before the outburst the NS surface radiates uniformly at a temperature $T_c \sim 0.15$ keV. Soon after the outburst onset the thermal map of XTE J1810-197 substantially changes. The region around the magnetic north pole is heated, reaches a temperature of $\sim$

Epoch	1T model reduced χ^2	2T model reduced χ^2	3T model reduced χ^2
TOTAL BAND			
Sep 03	1.72	1.58	0.12
Sep 04	0.66	0.42	0.36
Mar 05	1.02	0.98	0.79
Sep 05	1.06	0.40	0.39
Mar 06	2.94	1.70	1.25
Sep 06	0.94	0.38	0.35
Mar 07	2.88	2.88	2.37
Sep 07	1.12	1.12	0.96
HARD BAND			
Sep 03	1.12	1.00	0.73
Sep 04	0.45	0.39	0.37
Mar 05	2.23	2.14	0.95
Sep 05	1.18	0.58	0.54
Mar 06	0.85	0.82	0.77
Sep 06	0.22	0.21	0.20
Mar 07	0.99	0.99	0.93
Sep 07	1.18	1.18	1.06
HARD BAND			
Sep 03	2.16	0.48	0.19
Sep 04	2.41	1.58	0.98
Mar 05	0.34	0.25	0.21
Sep 05	0.59	0.42	0.39
Mar 06	0.34	0.31	0.19
Sep 06	0.98	0.80	0.76

Table 3.17: *reduced χ^2 for different thermal maps.*

0.7 keV and covers an area ~ 0.08 of the total star surface. This hot spot decreases in size and temperature until the March 2006 observation, when it becomes too small and cold to be distinguished from the surrounding warm corona. The warm region starts at a temperature ~ 0.3 keV, which remains constant during the subsequent evolution, and with an area ~ 0.16 of the total. The corona then decreases in size, and becomes a cap in March 2006, following the hot spot disappearance. In September 2007 (our last XTE J1810-197 observation) the warm cap is still visible, even if its area is down to only ~ 0.005 of the total (that is our resolution limit). The twist angle is highest at the beginning of the outburst (September 2003) and then steadily decreases until it reaches a more or less constant value around September 2005. The electron velocity does not show large variations in time and stays about constant around $\beta \sim 0.5$.

Synthetic and observed lightcurves (in the total band) are shown in Fig 3.7, together with the fit residuals. Since XTE J1810-197 pulse profiles are sinusoidal, we can com-

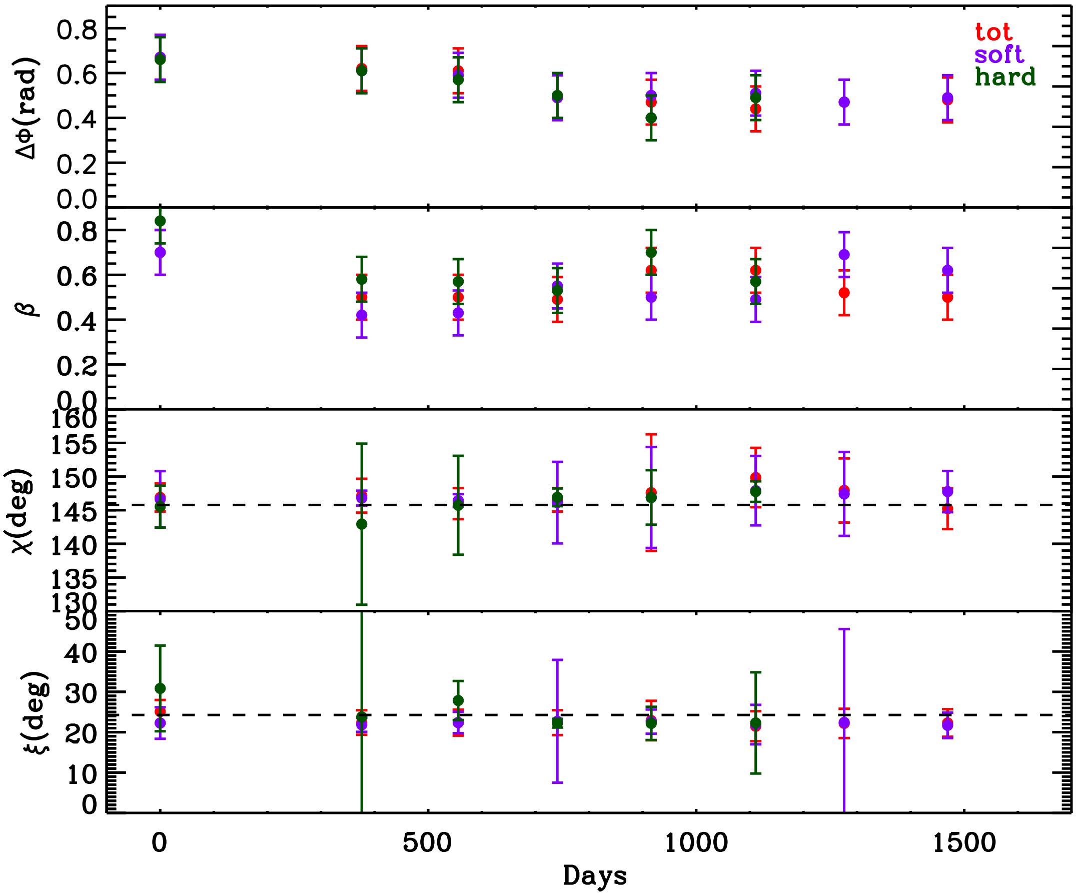

Figure 3.5: *Parameters evolutions for XTE J1810-197 for the three temperature model (results for all the three energy bands are shown). Time is in days from September 2003 observation.*

pute the pulsed fraction and its evolution in time at different energies. The comparison of model results with data is shown in Fig 3.8.

Before analysing the spectral behaviour for this source, as a further check, we verified that values obtained from the minimization routine indeed correspond to minima of the reduced χ^2. To do this five of the six parameters have been frozen to the value obtained with the `mpcurvefit.pro` minimization routine, and the reduced χ^2 is calculated for 100 values of the free parameter, around its minimum. If x_{min} is the value of the parameter obtained from the fit, then the reduced χ^2 curve should exhibit a

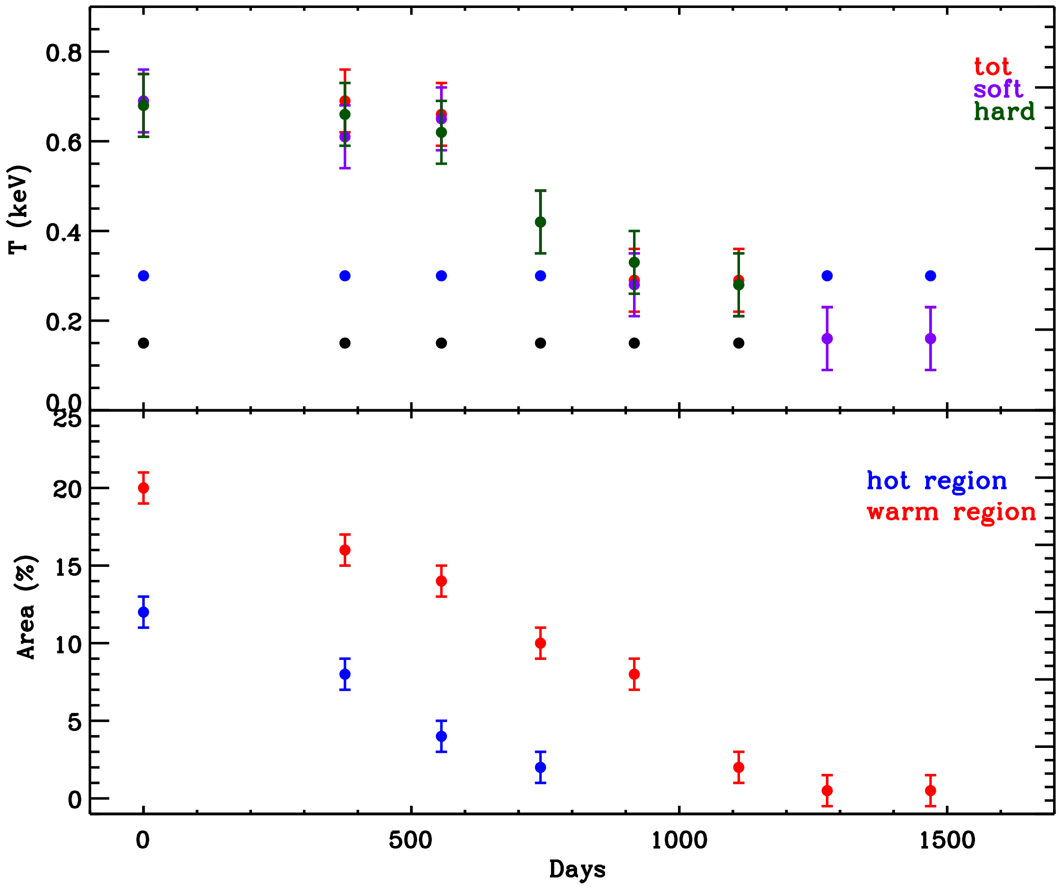

Figure 3.6: *On the top temperature trend (blue and black dots represent the fixed temperatures). On the bottom area of the different emitting regions (for the three energy band).. Time is in days from September 2003 observation.*

minimum in correspondance of x_{min}. This procedure has been repeated for all parameters in the three energy bands. Apart from temperature, all parameters obtained with the `mpcurvefit.pro` routine indeed correspond to minima of the reduced χ^2 curve (all reduced χ^2 plots are shown in the appendix A). The case of temperature, however, is more complex, since there are observations or energy bands for which the reduced χ^2 curves are very flat. In particular, for the September 2005 observation the reduced χ^2 curve obtained varying the hotter temperature is flat in all the three energy bands. Also the reduced χ^2 curve for the September 2006 observation relative to the warm temperature has the same problem. A deeper analysis of these two observations revealed that in both cases the size of the emitting area (respectively the hot and the

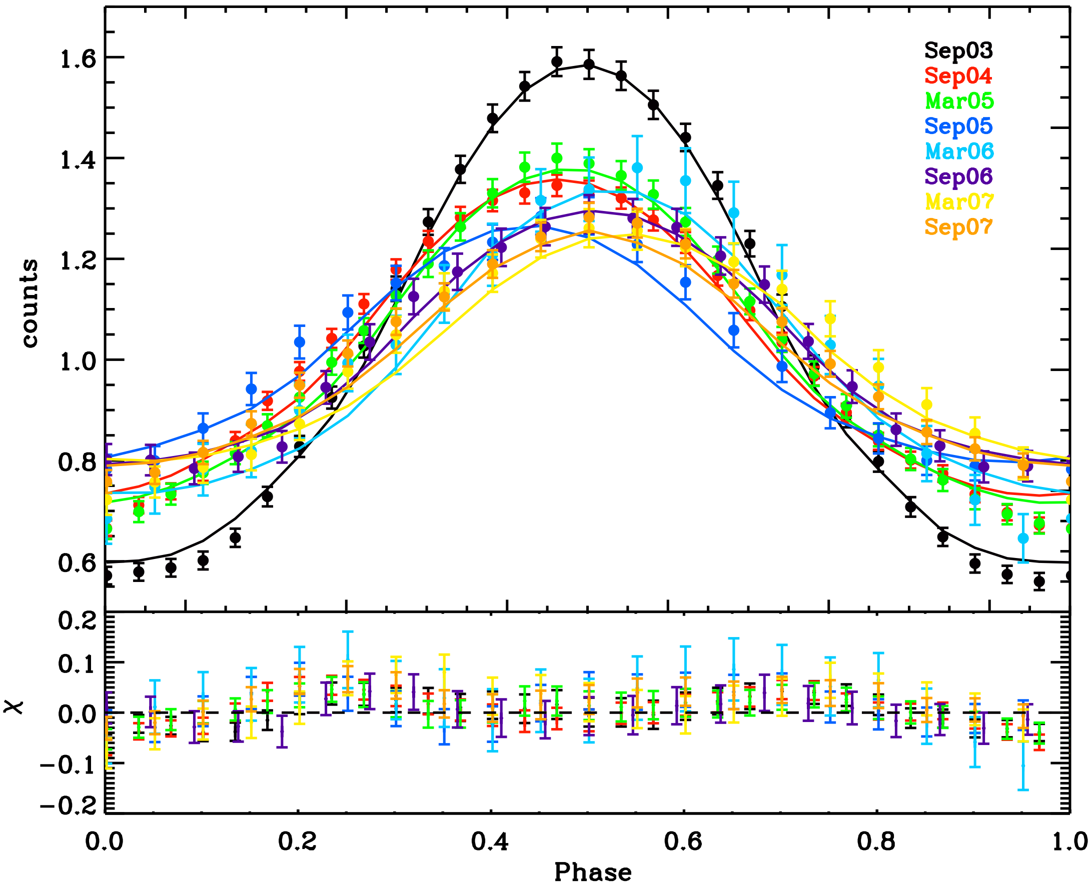

Figure 3.7: *Synthetic and observed pulse profiles for XTE J1810-197 in the total energy band. Iniatial phases are arbitrary.*

warm one) accounts for just 2% of the total neutron star surface. One may then conclude that the fit is not very sensible to temperature variation for too small emitting areas. In addition, there are two other cases in which for one of the three energy bands the reduced χ^2 curve obtained varying the temperature is flat. These are the March 2005 and the March 2006 observations. In the first case the reduced χ^2 curve refers to the hot temperature and the soft band. This can be understood considering that the hot temperature accounts for the hard band. On the contrary in the second case the reduced χ^2 curve refers to the warm temperature and the hard band. It is possible to justify this case considering that warm best fit temperature accounts principally for soft band.

Lightcurve analysis is unable, alone, to yield an univocal temperature value for both

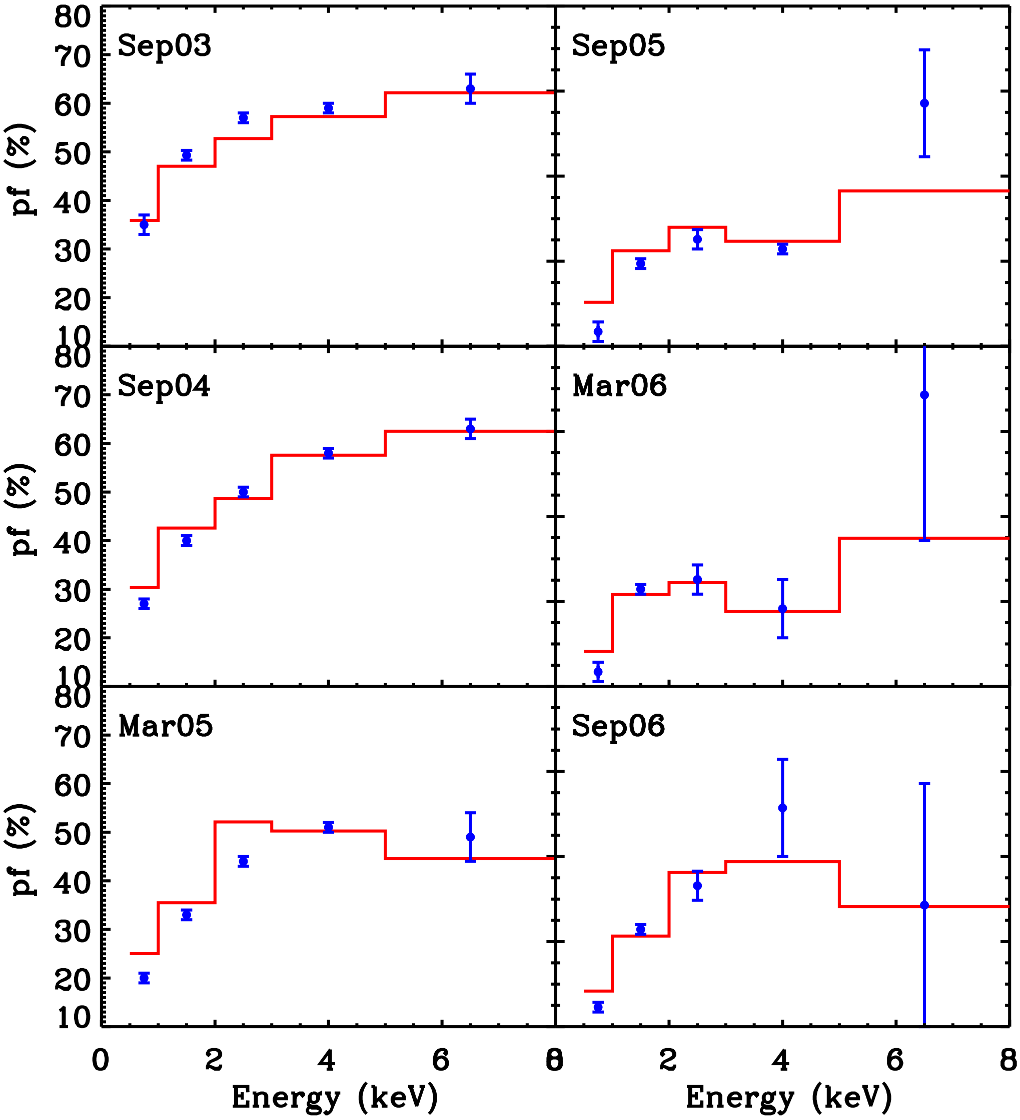

Figure 3.8: *The variation of XTE J1810-197 pulsed fraction with energy at different epochs. The red line refers to the model, blue circles to observations (errors are at* 1σ *level).*

the September 2005 and the 2006 observations. Anyway, as it will be discussed in next section, spectral analysis is more sensible to temperature variations, so that it is possible to infer a temperature value also in these cases (see sect. 3.5 for details).

3.5 Spectra

Having obtained from pulse profile fits a set of parameters and a thermal map able to describe XTE J1810-197 variability, we return to the analysis of source spectra during the outburst. In this section we discuss how the results we derived from the pulse profiles fittings can be applied to the spectral evolution of XTE J1810-197. Moreover a search for univocal temperature values for 2005 and 2006 September observations has been done.

In order to do this the `ntzang` model in XSPEC (NTZ; the model is currently available in the public library) has been used. This tool, however, has been created assuming emission from the entire star surface, and as such, is not suited to be directly applied to the present case. As a compromise, we decided to fit spectra adding together two or three (absorbed) `ntzang` models, each associated to one of the thermal components, at temperatures T_h, T_w and T_c, respectively.

The choice of adding different `ntzang` model, one for each temperature, can be simply explained considering the blackbody fit with XSPEC. In the `bb` case, infact, it is possible to fit spectra with complex thermal maps, by adding an arbitrary number of `bb` components, each of them representing one surface temperature. For example the spectrum produced from a neutron star with two regions at different temperatures T_1 and T_2, is indistinguishable from the spectrum obtained by adding two neutron stars radiating at two different uniform temperatures (again T_1 and T_2), with the appropriate radii. In NTZ case this assumption is true only as an approximation. Infact magnetic field lines are twisted, and thermal photons scatter with electrons moving in the magnetosphere. Since the twist is global thermal emission from a cap or the entire star will give rise to different spectra.

A `ntzang` spectrum for a neutron star with a termal map consisting of two regions at different temperatures ($T_1 = 0.15$ keV and $T_2 = 0.6$ keV) has been simulated and compared with the spectrum obtained adding two single `ntzang` at the same temperatures. The result is shown in Fig 3.9 and confirms that this approximation is acceptable, and remains, at the moment, the best way to describe the radiation coming from a *Magnetar* with a non uniform thermal emission.

For each XTE J1810-197 observation the fit was performed freezing $\Delta\phi$, β, T, χ and ξ at the values derived in sect. 3.4, while the normalization for every model (which is related to the emitting area) was left free to vary, together with N_H, which was

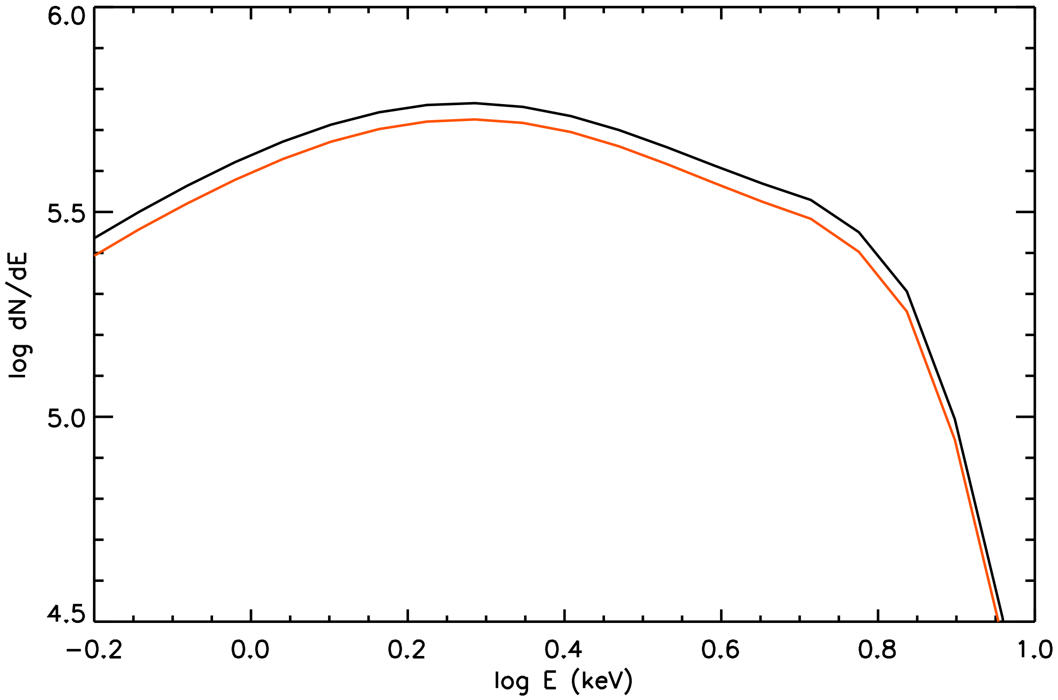

Figure 3.9: *Comparison between the spectrum obtained adding two single* `ntzang` *model (orange) and the spectrum of a neutron star with a thermal map consisting of two regions at different temperatures (black).*

however required to be the same for all the components and for all epochs.
Since for the September 2005 and the September 2006 observations the lightcurve analysis did not return an univocal value for the hotter temperature, it has been chosen to let also this parameters free to vary in both observations. In both cases, infact, reduced χ^2 changes significantly varying the temperature value.
Results for all the observations are shown in Fig. 3.10. The reduced χ^2 for the fits at the various epochs are listed in Tab. 3.18 and N_H is found to be $0.773 \pm 0.005 \times 10^{22}$ cm^{-2}.

It is important to remark that, in assessing the goodness of the fits, it should be kept in mind that only the normalizations of the three components (plus N_H), the hot temperature in the September 2005 observation and the warm temperature in the September 2006 observation are free to vary; all the other model parameters are frozen at the best-fit values obtained from the pulse profile analysis. Under these conditions we regard the agreement as quite satisfactory.

Label	reduced χ^2
Sep 03	1.22
Sep 04	1.93
Mar 05	1.50
Sep 05	1.52
Mar 06	1.34
Sep 06	1.45
Mar 07	1.08
Sep 07	1.29

Table 3.18: *reduced χ^2 values for spectral fitting.*

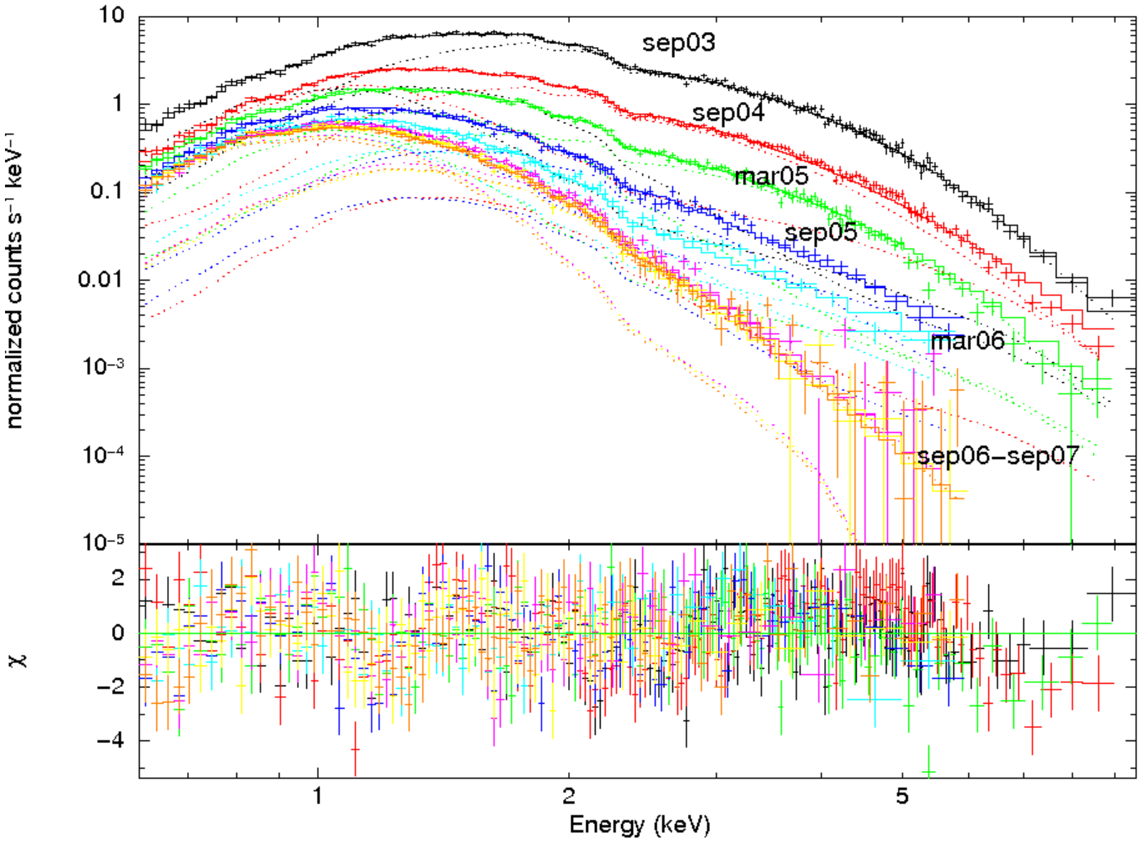

Figure 3.10: *XTE J1810-197 spectra.*

3.6 Discussion

XTE J1810-197 shows a decrease in flux during all the monitoring years, that can be connected with the variability in twist angle, temperature and size of the emitting regions.

As discussed by Beloborodov (2009) we assume, soon after the burst, the formation of a hot region centered on the magnetic axis, whose temperature and size decrease during the outburst phase. Moreover we identify a rapidly increase in the twist angle, followed by an untwist behaviour. For the TAXPs prototype XTE J1810-197 we found a twist angle decay until September 2005, followed by an almost steady state, which we believe to represent the queiscent value for the twist. Beloborodov (2009) also discussed the possibility of a localized twist, which involves only the starquake region. Actually our model does not allow us to verify this hypotesis, since we base our study on the NTZ montecarlo archive, that has been created for a global twist.

Our study of the Transient AXP XTE J1810-197 base itself on one require: the geometrical angles χ and ξ must remain constant during all the outburst phase. For this source we can compare our results with Perna & Gotthelf (2008) ones, who discuss a geometrical model able to describe the outburst behaviour for the source. Unlike their model, in which both χ and ξ angles are in the range $[0; \pi/2]$, in our case $0 \leq \chi \leq \pi$ and $0 \leq \xi \leq \pi/2$. However we found a really good correspondance between the two results. Infact Perna & Gotthelf (2008) found, for ξ, a value of $\sim 23°$, the same value obtained by us; moreover the values obtained for χ angle are $\sim 53°$ for them and $\sim 148°$ for us. Considering the different variability range in the two cases, we can infer that also for the angle between line of sight and spin axis we obtain, within the errors, a quite good agreement.

These authors also derived a thermal map for the source. They obtained, for the hot spot, a temperature always higher than us. Moreover they consider only two emitting regions achieving a cold temperature variable with epochs. As a consequence, only few values are comparable with our results. This different choice for the thermal map weights also on the emitting area size; infact whereas in our study both the hot spot and the warm corona decrease during the outburst phase, in their model only the hot spot decreases, while the warm corona increases in size. However it is possible to make a comparison between the hot spot size in the two cases, finding a correspondance between the two initial sizes and also between the decreasing trend for the two models.

For XTE J1810-197 we obtain a thermal map evolution similar to the one obtained by Bernardini et al. (2009). As in their case the neutron star thermal map is initially divided into three regions at different temperatures. While they are able to distinguish the hot cap until March 2006, our resolution allowes us to do it only until September 2005. Moreover in our case the hot cap temperature decrease is greater than in Bernardini et al. (2009). In both models the presence of a region at a temperature of ~ 0.3 keV is required. Since lightcurve feature changes according to the emitting region position, we are also able to locate it. We found that this region is a corona that surrounds the hot cap. Also the corona decreases in size with time during all the outburst phase. The rest of the AXP surface remains at a temperature comparable to the quiescent one (measured by ROSAT) during all the monitoring years, so we suppose that this region is not involved in the burst. In September 2007 the 99.5% of XTE J1810-197 surface radiates at a temperature of ~ 0.15 keV. The comparison between this observation and the ROSAT quiescent one, reveals that the object is near the quiescent state. We can infer that the TAXP, at the end of the outburst, radiates again at a uniform temperature of ~ 0.15 keV.

Chapter 4

CXOU J164710.2-455216

Having verified that the resonant compton scattering model can provide a reasonable interpretation for the post-outburst timing and spectral evolution of TAXP prototype XTE J1810-197, the model has been applied to CXOU J164710.2-455216, the other transient AXP for which a large enough number of *XMM-Newton* observations covering the 2006 outburst decay are available (see table 4.1 for details).

Label	OBS ID	Epoch	Exposure time (s)
Sep06b	0311792001	2006-09-22	2.6784E+04
Feb07	0410580601	2007-02-17	1.4739E+04
Aug07	0505290201	2007-08-19	3.2889E+04
Feb08	0505290301	2008-02-15	3.2914E+04
Aug08	0555350101	2008-08-20	3.2918E+04
Aug09	0604380101	2009-08-24	4.3621E+04

Table 4.1: *CXOU J164710.2-455216 observations*

CXOU J164710.2-455216 has a peculiar pulse profile, which drastically changed soon after the outburst from a one-peaked to a three-peaked pattern. A direct inspection of the pulse profiles in our archive shows that there are some peculiar cases in which multipeaked curves can be produced. This requires a particular geometrical configuration, with the misalignement between magnetic and spin axis near to $\pi/2$.

The analysis of the pulse profiles of CXOU J164710.2-455216 follows closely that presented in Chap. 3. In particular, after having verified the compatibility between the model and the observations with the principal component analysis, it has been first tried a single temperature and then two-temperature model, encountering the same problems found for XTE J1810-197. Finally, it has been applied a three-zone thermal map and this provided reasonable fits for the lightcurves, at the same time not causing the angles χ and ξ to vary in the same observation for the different energy bands and for different epochs.

4.1 PCA Analysis

As in XTE J1810-197, principal component analysis has been applied to the TAXP CXOU J164710.2-455216. Synthetic lightcurves have been generated for 32 phases in the range $[0, 2\pi]$ and for a 9×9 angular grid, $0° \leq \xi \leq 90°$ (step $10°$), $0° \leq \chi \leq 180°$ (step $20°$), for a total of 136323 models.

Again we have verified, for each observation and in each energy band, if there is a combination of the parameters for which a synthetic pulse profile reproduces the data. A graphic representation similar to XTE 1810 one, is shown in Fig. 4.1. As in the previous case, the minimum of the Euclidean distance $\sum_{i=1}^{32}(Z_i - Z_i^{obs})^2$ between the models and the observed pulse profile has been calculated for every observation and

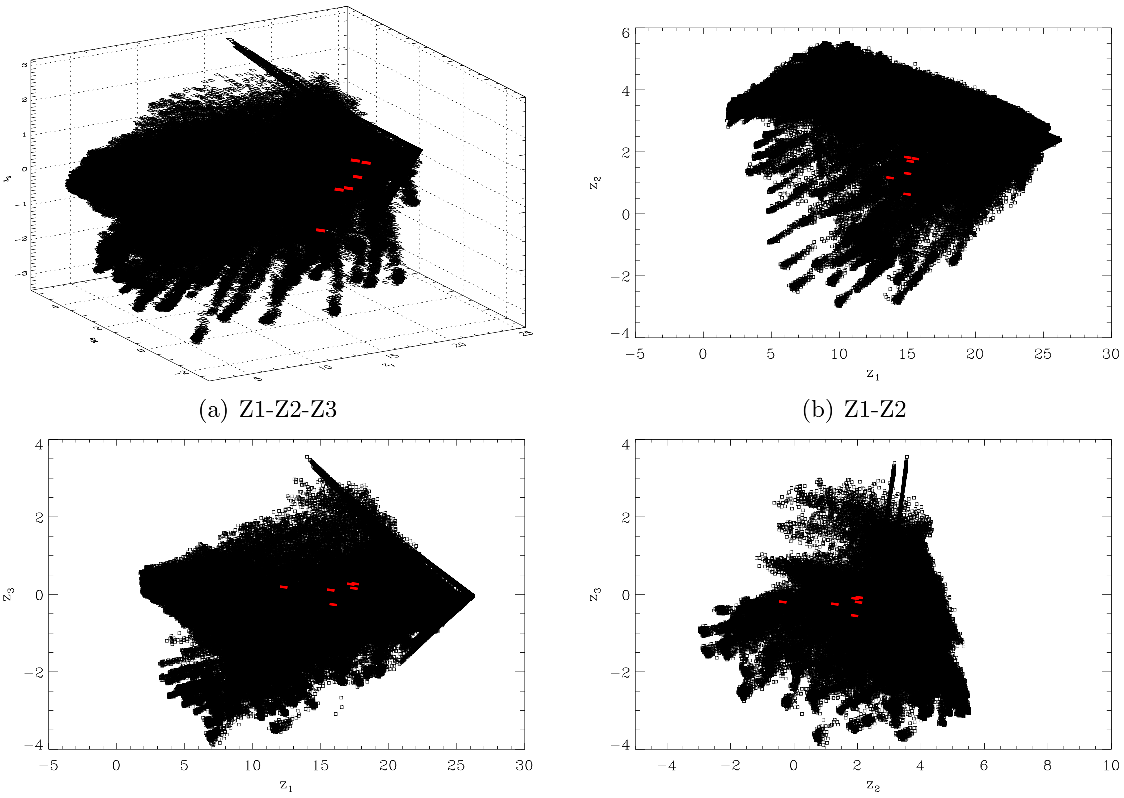

(a) Z1-Z2-Z3

(b) Z1-Z2

(c) Z1-Z3

(d) Z2-Z3

Figure 4.1: *Principal component representation of the simulated lightcurves in our archive (black dots) together with the observed lightcurves of CXOU J164710.2-455216 (red dots). All the pulse profiles refer to the 0.5-10 keV band.*

used as the starting point for minimization analysis.

4.2 Emission from all the surface

As in XTE J1810-197 analysis, for every epoch and every energy band, the model obtained with the pca analysis has been used as starting point for the fit procedure. In this preliminarly analysis we chose the simplest assumption for the thermal distribution, that is all the star is radiating at the same temperature T. Synthetic lightcurves have been computed, using the `mpcurvefit.pro` minimization routine, for the total ($0.5-10$ keV), soft ($0.5 - 2$ keV) and hard ($2 - 10$ keV) energy bands. As in XTE J1810-197 minimization routine involves six free parameters ($\Delta\phi$, β, T, χ, ξ, and the initial phase), and lightcurves have been normalized in the same way (see sect. 3.2). Since lightcurve shape for CXOU J164710.2-455216 is more complex than XTE J1810-197 one, a worst reduced χ^2 is expected. However a quite good agreement has been found. The success in finding a solution able to describe such a complex pulse shape is, even more than in XTE J1810-197, a strong hint that resonant compton scattering model may correctly describe transient AXP phenomena. Results for this first modellization are listed Tab. 4.2, 4.3 and 4.4 and showed in Fig. 4.2.

Label	$\Delta\phi$ (rad)	T (keV)	β	ξ(deg)	χ (deg)
Sep06b	1.15 ± 0.01	0.72 ± 0.01	0.22 ± 0.02	77.6 ± 12.1	27.2 ± 4.8
Feb07	1.04 ± 0.01	0.69 ± 0.01	0.16 ± 0.13	70.9 ± 6.8	36.3 ± 11.8
Aug07	0.96 ± 0.01	0.64 ± 0.01	0.10 ± 0.01	72.4 ± 2.7	35.1 ± 3.4
Feb08	0.86 ± 0.01	0.50 ± 0.01	0.29 ± 0.08	78.9 ± 5.4	26.9 ± 8.1
Aug08	0.61 ± 0.17	0.39 ± 0.01	0.57 ± 0.08	85.3 ± 1.4	32.5 ± 7.8
Aug09	0.57 ± 0.22	0.70 ± 0.50	0.64 ± 0.33	88.9 ± 1.7	24.1 ± 1.0

Table 4.2: *Parameters set for the total band for a uniform temperature distribution*

Label	$\Delta\phi$ (rad)	T (keV)	β	ξ(deg)	χ (deg)
Sep06b	1.17 ± 0.01	0.70 ± 0.01	0.14 ± 0.01	82.3 ± 0.1	22.5 ± 0.2
Feb07	1.07 ± 0.01	0.55 ± 0.01	0.10 ± 0.01	85.4 ± 0.5	22.3 ± 0.2
Aug07	0.96 ± 0.01	0.90 ± 0.01	0.20 ± 0.05	80.3 ± 0.3	24.6 ± 0.1
Feb08	0.89 ± 0.01	0.78 ± 0.01	0.20 ± 0.04	83.5 ± 0.1	24.0 ± 0.6
Aug08	0.74 ± 0.01	0.22 ± 0.01	0.85 ± 0.01	88.1 ± 4.0	8.5 ± 1.2
Aug09	0.55 ± 0.01	0.16 ± 0.14	0.71 ± 0.01	72.4 ± 14.1	38.8 ± 16.9

Table 4.3: *Parameters set for the soft band for a uniform temperature distribution*

1σ errors for all parameters are obtained from the minimization routine. Note that

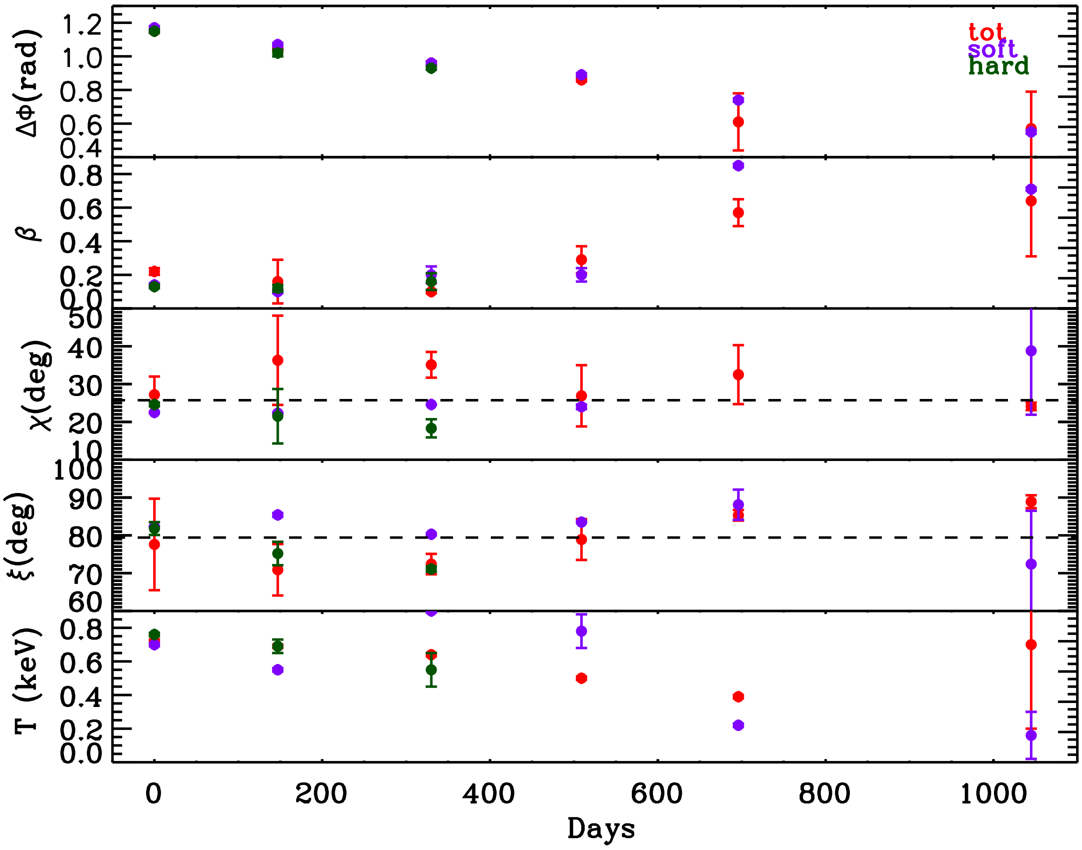

Figure 4.2: *Parameters evolution for CXOU J164710.2-455216 (uniform surface temperature); results refer to the three energy band: red dots are for the total, liliac dots are for the soft and blue dots are for the hard. Time is computed starting from the September 2006 observation.*

Label	$\Delta\phi$ (rad)	T (keV)	β	ξ(deg)	χ (deg)
Sep06b	1.15 ± 0.01	0.76 ± 0.01	0.13 ± 0.01	81.8 ± 1.7	24.6 ± 0.5
Feb07	1.02 ± 0.02	0.69 ± 0.04	0.12 ± 0.02	75.2 ± 3.1	21.5 ± 7.2
Aug07	0.93 ± 0.01	0.55 ± 0.10	0.16 ± 0.05	71.1 ± 0.7	18.3 ± 2.4

Table 4.4: *Parameters set for the hard band for a uniform temperature distribution*

analysis for the hard band stops after August 2007 observation. This is because in 2008 and 2009 observations photons with energy greater than 2 keV are very few and, as a consequence, indetermination in lightcurves is very high.

As showed by Fig. 4.2 also for this source physical parameter values ($\Delta\phi$, T and β) are the same (whitin the errors) for the three energy bands. Moreover temperature and twist angle follow a resonable trend, since both quantities monotonically decrease in time, as expected if the outburst was related to a change in magnetic structure. However also in this case model is not satisfactory, since the geometrical angles χ and ξ changes too much from one observation to the other, and even in the same observation for different energy bands.

4.3 Emission from two regions

Results obtained with the 1 temperature model are not satisfactory so, on the base of XTE J1810-197 analysis, a two temperature model with one hot cap and the rest of the star at a colder temperature, has been tried in order to describe CXOU J164710.2-455216 peculiar behaviour. In this case there are no temperature suggestions coming from the 1 temperature model, since in both total and soft band the last two observations show a great indetermination in temperature values. In order to find to best set of parameters and thermal map able to reproduce CXOU J164710.2-455216 lightcurves, it has been chosen to run the minimization routine several times, fixing at every turn a different value for the cold temperature: $T_c = 0.10, 0.15, 0.20, 0.25, 0.30$, and letting free to vary the hotter one. Moreover analysis for every observation has been repeated for eight values of the cap area:A_h = 0.78%, 1.56%, 3.12%, 6.25%,9.37%, 12.5%, 15.62%, 18.75% (in terms of the total surface). Results for fit parameters and thermal map are listed in Tab. 4.5, 4.6, 4.7, 4.8, 4.9 and 4.10 and showed in Fig. 4.3 and 4.4. Also in this case 1σ errors for all parameters are obtained from the minimization routine.

As in XTE J1810-197, the addition of a second thermal component improves the fit reduced χ^2 (see Tab. 4.17), preserving the good trend for twist angle, electron bulk

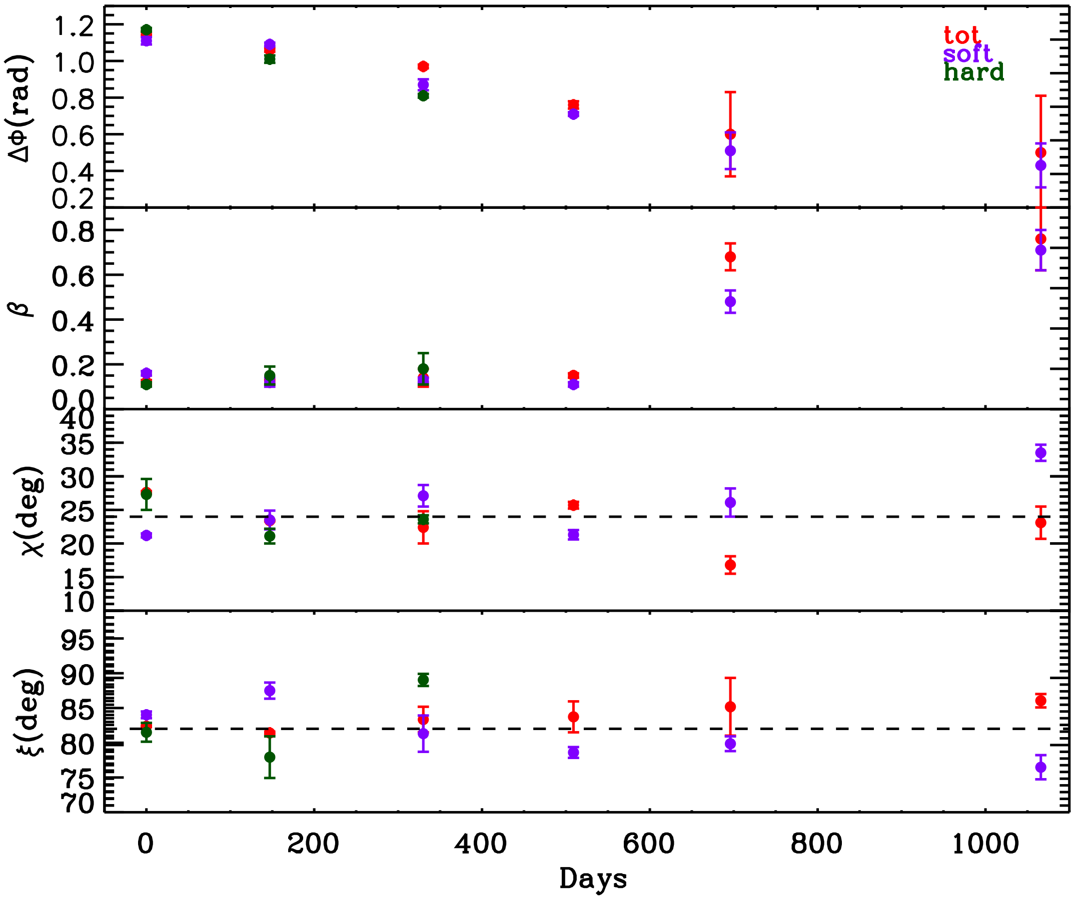

Figure 4.3: *Parameters evolution with time (two temperature model). Results refer to the three energy band: red dots are for the total, liliac dots are for the soft and blue dots are for the hard. Time is in days from the September 2006 observation.*

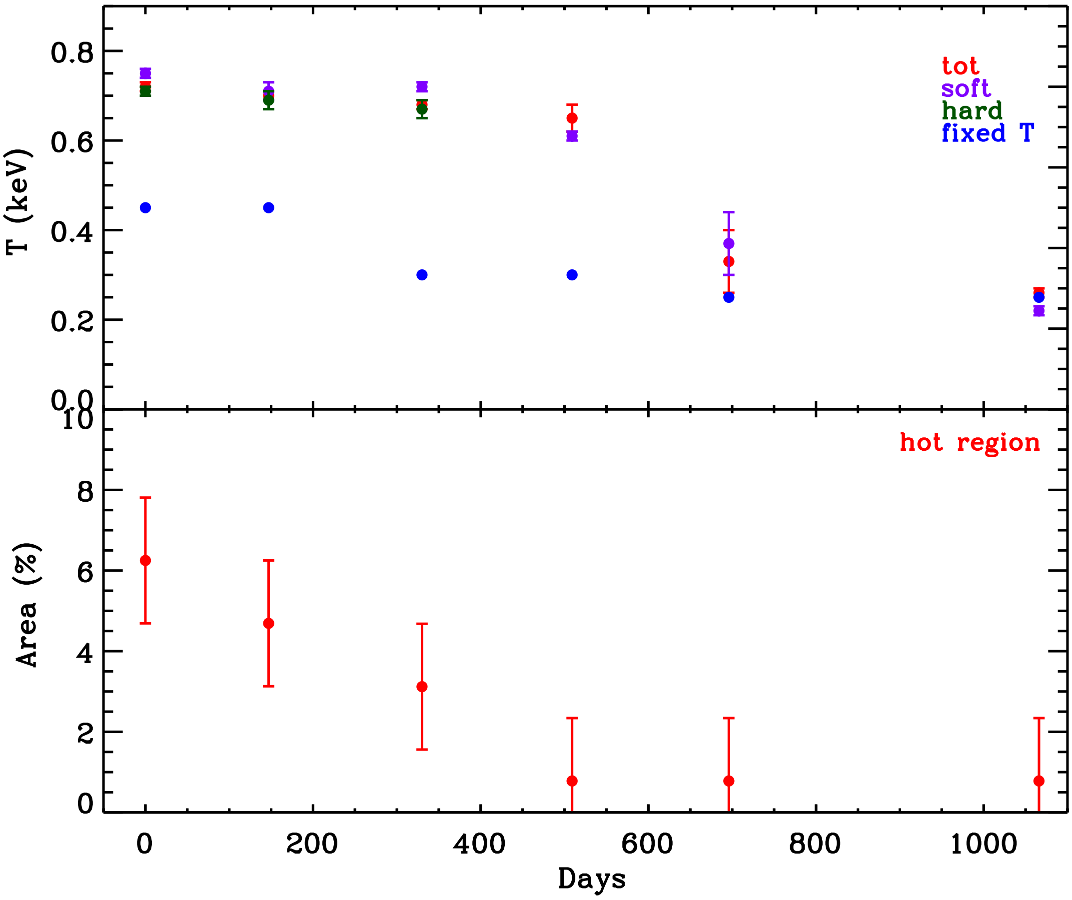

Figure 4.4: *Same as Fig. 4.3 for the thermal map evolution with time.*

Label	$\Delta\phi$ (rad)	β	ξ(deg)	χ (deg)
Sep06b	1.15 ± 0.01	0.12 ± 0.01	82.8 ± 0.1	27.6 ± 0.2
Feb07	1.06 ± 0.01	0.12 ± 0.01	81.8 ± 0.2	23.4 ± 0.1
Aug07	0.97 ± 0.01	0.14 ± 0.04	83.8 ± 1.9	22.4 ± 2.4
Feb08	0.76 ± 0.02	0.15 ± 0.01	84.2 ± 2.3	25.7 ± 0.5
Aug08	0.60 ± 0.23	0.68 ± 0.06	85.7 ± 4.3	16.8 ± 1.3
Aug09	0.50 ± 0.31	0.76 ± 0.14	86.6 ± 1.0	23.1 ± 2.4

Table 4.5: *CXOU J164710.2-455216 parameters set for the total band for a two temperature model*

Label	$T_h(keV)$	$A_h(\%)$	$T_c(keV)$	$A_c(\%)$
Sep06b	0.72 ± 0.01	6.25 ± 1.56	0.45	93.75 ± 1.56
Feb07	0.70 ± 0.01	4.69 ± 1.56	0.45	95.31 ± 1.56
Aug07	0.68 ± 0.01	3.12 ± 1.56	0.30	96.88 ± 1.56
Feb08	0.65 ± 0.03	0.78 ± 1.56	0.30	99.22 ± 1.56
Aug08	0.33 ± 0.07	0.78 ± 1.56	0.25	99.22 ± 1.56
Aug09	0.26 ± 0.01	0.78 ± 1.56	0.25	99.22 ± 1.56

Table 4.6: *CXOU J164710.2-455216 thermal map for the total band for a two temperature model. Where no error is reported, the temperarature was kept fixed.*

Label	$\Delta\phi$ (rad)	β	ξ(deg)	χ (deg)
Sep06b	1.11 ± 0.02	0.16 ± 0.01	84.5 ± 0.5	21.2 ± 0.3
Feb07	1.09 ± 0.01	0.12 ± 0.02	88.1 ± 1.2	23.5 ± 1.4
Aug07	0.87 ± 0.03	0.13 ± 0.01	81.7 ± 2.7	27.1 ± 1.6
Feb08	0.71 ± 0.01	0.11 ± 0.01	78.9 ± 0.8	21.3 ± 0.7
Aug08	0.51 ± 0.10	0.48 ± 0.05	80.2 ± 1.1	26.1 ± 2.1
Aug09	0.43 ± 0.12	0.71 ± 0.09	76.7 ± 1.8	33.5 ± 1.2

Table 4.7: *CXOU J164710.2-455216 parameters set for soft band for a two temperature model.*

Label	$T_h(keV)$	$A_h(\%)$	$T_c(keV)$	$A_c(\%)$
Sep06b	0.75 ± 0.01	6.25 ± 1.56	0.45	93.75 ± 1.56
Feb07	0.71 ± 0.02	4.69 ± 1.56	0.45	95.31 ± 1.56
Aug07	0.72 ± 0.01	3.12 ± 1.56	0.30	96.88 ± 1.56
Feb08	0.61 ± 0.01	0.78 ± 1.56	0.30	99.22 ± 1.56
Aug08	0.37 ± 0.07	0.78 ± 1.56	0.25	99.22 ± 1.56
Aug09	0.22 ± 0.01	0.78 ± 1.56	0.25	99.22 ± 1.56

Table 4.8: *CXOU J164710.2-455216 thermal map for the soft band for a two temperature model. Where no error is reported, the temperarature was kept fixed.*

velocity and surface temperature. However, even if reduced, the geometrical angles (χ and ξ) variations are still too high (both for different epochs and for the same epoch

Label	$\Delta\phi$ (rad)	β	ξ(deg)	χ (deg)
Sep06b	1.17 ± 0.01	0.11 ± 0.01	81.9 ± 1.4	27.3 ± 2.3
Feb07	1.01 ± 0.02	0.15 ± 0.04	78.2 ± 3.1	21.1 ± 1.1
Aug07	0.81 ± 0.01	0.18 ± 0.07	89.7 ± 0.9	23.6 ± 0.6

Table 4.9: *CXOU J164719.2-455216 parameters set for hard band for a two temperature model.*

Label	$T_h(keV)$	$A_h(\%)$	$T_w(keV)$	$A_w(\%)$
Sep06b	0.71 ± 0.01	6.25 ± 1.56	0.45	93.75 ± 1.56
Feb07	0.69 ± 0.02	4.69 ± 1.56	0.45	95.31 ± 1.56
Aug07	0.67 ± 0.02	3.12 ± 1.56	0.30	96.88 ± 1.56

Table 4.10: *CXOU J164710.2-455216 thermal map for the hard band for a two temperature model.*

but in different energy bands) to be satisfactory.

4.4 Emission from three regions

In order to further improve the fit reduced χ^2 and to reduce the variability range for the two geometrical angles χ and ξ, a third termal component has been added to the TAXP CXOU J164710.2-455216 thermal map. As in XTE J1810-197 the thermal map is actually made by a hot cap centered on the magnetic pole at the temperature T_h, a concentric warm corona at T_w and the rest of the neutron star at the colder temperature T_c. The new montecarlo archive discussed in sect. 3.4 has been used for this new analysis. Information from the two temperature modellization are used as a starting point for the analysis. Every fit has been repeated for ten values of the hot cap area $A_h = 0.5\%$, 1%, 2%, 4%, 6%, 8%, 10%, 12%, 14%, 16% (of the total surface) and for 20 values of the warm corona area $A_w = 0.5\%$, 1%, 2%, 4%, 6%, 8%, 10%, 12%, 14%, 16%, 18%, 20%, 22%, 24%, 26%, 28%, 30%, 32%, 34%, 36% (of the total surface). Moreover lightcurves fit have been iterated for two values of the cold temperature $T_c = 0.15, 0.30$ keV and also for two values of the warm temperature $T_w = 0.30, 0.45$ keV. The hotter temperature has let free to vary. In the last two observations, indipendently from hot cap area size, temperature always returns the value of 0.45 keV, which corresponds to the temperature of the warm corona that minimize the fit. We conclude that, at least for our stellar grid resolution, in the last two observations there are only two thermal componenents that contribute to neutron star emission. Opposite to XTE J1810-197, for CXOU J164710.2-455216 the emitting area of the warm corona increases with time until February 2008 observation, and then keeps the same value until August 2009 (our last observation).

Results obtained for this thermal map are reported in Tabs. 4.11, 4.12, 4.13, 4.14, 4.15 and 4.16 and plotted in Figs. 4.5 and 4.6. Parameters and size of the emitting area errors for this model have been calculated as in XTE J1810-197 analysis (see sect. 3.4 fo details) and have the same meaning as in that case.

Epoch	$\Delta\phi(rad)$	β	$\xi(^\circ)$	$\chi\ (^\circ)$
Sep 06b	$1.12^{+0.08}_{-0.14}$	$0.18^{+0.03}_{-0.03}$	$83.5^{+1.0}_{-1.4}$	$20.8^{+0.1}_{-0.5}$
Feb 07	$1.07^{+0.05}_{-0.10}$	$0.19^{+0.02}_{-0.03}$	$80.0^{+2.7}_{-2.1}$	$23.2^{+1.7}_{-1.7}$
Aug 07	$1.00^{+0.18}_{-0.06}$	$0.15^{+0.02}_{-0.05}$	$82.1^{+1.1}_{-1.1}$	$19.2^{+2.7}_{-1.3}$
Feb 08	$0.77^{+0.21}_{-0.12}$	$0.20^{+0.05}_{-0.09}$	$85.7^{+2.7}_{-4.1}$	$20.4^{+7.2}_{-0.7}$
Aug 08	$0.65^{+0.12}_{-0.07}$	$0.70^{+0.05}_{-0.05}$	$80.1^{+2.7}_{-9.7}$	${}^{2}8.4{+}4.9_{-7.3}$
Aug 09	$0.55^{+0.11}_{-0.10}$	$0.79^{+0.06}_{-0.06}$	$87.0^{+9.7}_{-10.9}$	$25.5^{+4.9}_{-10.}$

Table 4.11: *CXOU J164710.2-455216 parameters for the total band for a three temperature model*

Epoch	$T_h(keV)$	$T_w(keV)$	$T_c(keV)$	$A_h(\%)$	$A_w(\%)$
Sep 06b	$0.70^{+0.20}_{-0.11}$	0.45	0.15	$8. \pm 1.$	$22. \pm 1.$
Feb 07	$0.64^{+0.16}_{-0.06}$	0.45	0.15	$6. \pm 1.$	$24. \pm 1.$
Aug 07	$0.63^{+0.18}_{-0.10}$	0.45	0.15	$4. \pm 1.$	$26. \pm 1.$
Feb 08	0.62^{---}_{---}	0.45	0.15	$2. \pm 1.$	$28. \pm 1.$
Aug 08	-	$0.49^{+0.02}_{-0.05}$	0.15	-	$30. \pm 1.$
Aug 09	-	$0.46^{+0.05}_{-0.05}$	0.15	-	$30. \pm 1.$

Table 4.12: *CXOU J164710.2-455216 thermal map parameters for the total band for a three temperature model (hot temperature value for Feb08 observation has been obtained from the spectral analysis)*

Epoch	$\Delta\phi(rad)$	β	$\xi(^\circ)$	χ $(^\circ)$
Sep 06b	$1.17^{+0.01}_{-0.16}$	$0.14^{+0.02}_{-0.04}$	$82.9^{+0.6}_{-1.4}$	$24.3^{+4.2}_{-3.0}$
Feb 07	$1.06^{+0.01}_{-0.13}$	$0.14^{+0.02}_{-0.04}$	$81.2^{+1.6}_{-4.6}$	$25.6^{+1.9}_{-4.5}$
Aug 07	$0.93^{+0.18}_{-0.06}$	$0.12^{+0.01}_{-0.01}$	$81.4^{+1.5}_{-3.5}$	$23.3^{+1.4}_{-2.0}$
Feb 08	$0.81^{+0.34}_{-0.09}$	$0.11^{+0.04}_{-0.01}$	$85.2^{+1.4}_{-3.0}$	$24.1^{+3.1}_{-3.0}$
Aug 08	$0.79^{+0.06}_{-0.14}$	$0.59^{+0.05}_{-0.02}$	$89.6^{+4.7}_{-7.5}$	$18.5^{+3.4}_{-4.6}$
Aug 09	$0.54^{+0.12}_{-0.14}$	$0.75^{+0.10}_{-0.16}$	$81.4^{+13.9}_{-7.5}$	$24.3^{+9.9}_{-20.0}$

Table 4.13: *CXOU J164710.2-455216 parameters for the soft band for a three temperature model*

Epo	$T_h(keV)$	$T_w(keV)$	$T_c(keV)$	$A_h(\%)$	$A_w(\%)$
Sep 06b	$0.74^{+0.15}_{-0.19}$	0.45	0.15	$8. \pm 1.$	$22. \pm 1.$
Feb 07	$0.63^{+0.16}_{-0.18}$	0.45	0.15	$6. \pm 1.$	$24. \pm 1.$
Aug 07	$0.63^{+0.21}_{-0.12}$	0.45	0.15	$4. \pm 1.$	$26. \pm 1.$
Feb 08	0.65^{---}_{---}	0.45	0.15	$2. \pm 1.$	$28. \pm 1.$
Aug 08	-	$0.45^{+0.01}_{-0.02}$	0.15	-	$30. \pm 1.$
Aug 09	-	$0.45^{+0.15}_{-0.11}$	0.15	-	$30. \pm 1.$

Table 4.14: *CXOU J164710.2-455216 thermal map parameters for the soft band for a three temperature model (hot temperature value for Feb 08 observation has been obtained from the spectral analysis)*

Results obtained for the TAXP CXOU J164710.2-455216 can be summarized as follows: according to our model, CXOU J164710.2-4552116 is viewed at an angle $\chi = 23^{+4\circ}_{-3}$ with respect to its spin axis. The spin and the magnetic axes are almost ortogonal, $\xi = 84^{+5\circ}_{-3}$. This is a quite peculiar condition, and it seems to be the only one able to explain, within the present model, the characteristic three-peaked shape of the observed lightcurves. Also in this case we calculated the probability that values for the two geometrical angles χ and ξ were not costant during time, finding a value of 0.92%

Epoch	$\Delta\phi(rad)$	β	$\xi(°)$	χ (°)
Sep 06b	$1.13^{+0.06}_{-0.12}$	$0.23^{+0.05}_{-0.04}$	$88.1^{+0.6}_{-5.6}$	$21.2^{+1.8}_{-1.0}$
Feb 07	$1.05^{+0.08}_{-0.06}$	$0.14^{+0.12}_{-0.03}$	$84.0^{+1.4}_{-2.2}$	$20.0^{+2.2}_{-2.3}$
Aug 07	$1.00^{+0.01}_{-0.02}$	$0.21^{+0.01}_{-0.02}$	$86.7^{+0.6}_{-5.0}$	$27.2^{+0.6}_{-6.2}$

Table 4.15: *CXOU J164710.2-455216 parameters for the hard band for a three temperature model*

Epo	$T_h(keV)$	$T_w(keV)$	$T_c(keV)$	$A_h(\%)$	$A_w(\%)$
Sep 06b	$0.60^{+0.01}_{-0.07}$	0.45	0.15	8. ± 1.	22. ± 1.
Feb 07	$0.62^{+0.02}_{-0.06}$	0.45	0.15	6. ± 1.	24. ± 1.
Aug 07	$0.67^{+0.01}_{-0.01}$	0.45	0.15	4. ± 1.	26. ± 1.

Table 4.16: *CXOU J164710.2-455216 thermal map parameters for the hard band for a three temperature model*

Epoch	1T model reduced χ^2	2T model reduced χ^2	3T model reduced χ^2
TOTAL BAND			
Sep 06b	1.05	0.86	0.31
Feb 07	1.32	0.76	0.65
Aug 07	0.97	0.91	0.44
Feb 08	1.45	1.12	0.63
Aug 08	1.45	1.23	0.79
Aug 09	2.03	1.97	1.52
HARD BAND			
Sep 06b	0.54	0.21	0.18
Feb 07	1.39	0.92	0.77
Aug 07	0.99	0.78	0.61
Feb 08	1.23	0.97	0.69
Aug 08	1.82	1.18	0.77
Aug 09	0.96	0.57	0.42
HARD BAND			
Sep 06b	0.91	0.73	0.57
Feb 07	1.60	1.28	1.07
Aug 07	4.88	4.54	3.60

Table 4.17: *CXOU J164710.2-455216 reduced χ^2 for different thermal maps.*

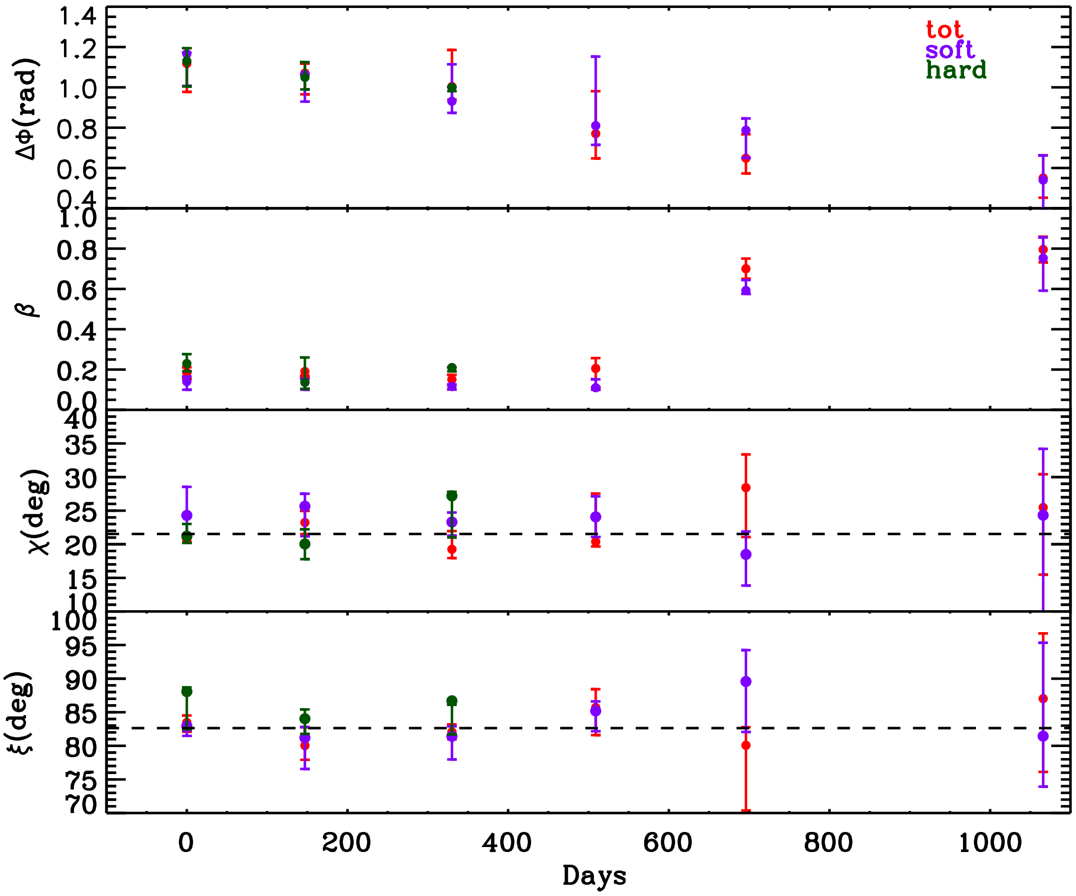

Figure 4.5: *Parameters evolutions for CXOU J164710.2-455216 for the three temperature model(results for the three energy bands are shown). Time is in days from September 2006 observation.*

for ξ and 0.23% for χ.

Soon after the burst the thermal map of CXOU J164710.2-455216 consists of three regions at different temperatures. The hottest region, around the north magnetic pole, has a temperature $T_h \sim 0.7$ keV, and its area is ~ 0.08 of the total. This hot spot decreases in temperature and size as time elapses, until February 2008. In August 2008 the hot spot becomes so small in size and its temperature so close to that of the warm corona, to make impossible to distinguish between the two regions.

The warm corona has a temperature of ~ 0.45 keV, which remains constant during the two years of observations. In this case the corona area increases with time, starting from ~ 0.2 and reaching ~ 0.3 of the NS surface. The third region has a lower tem-

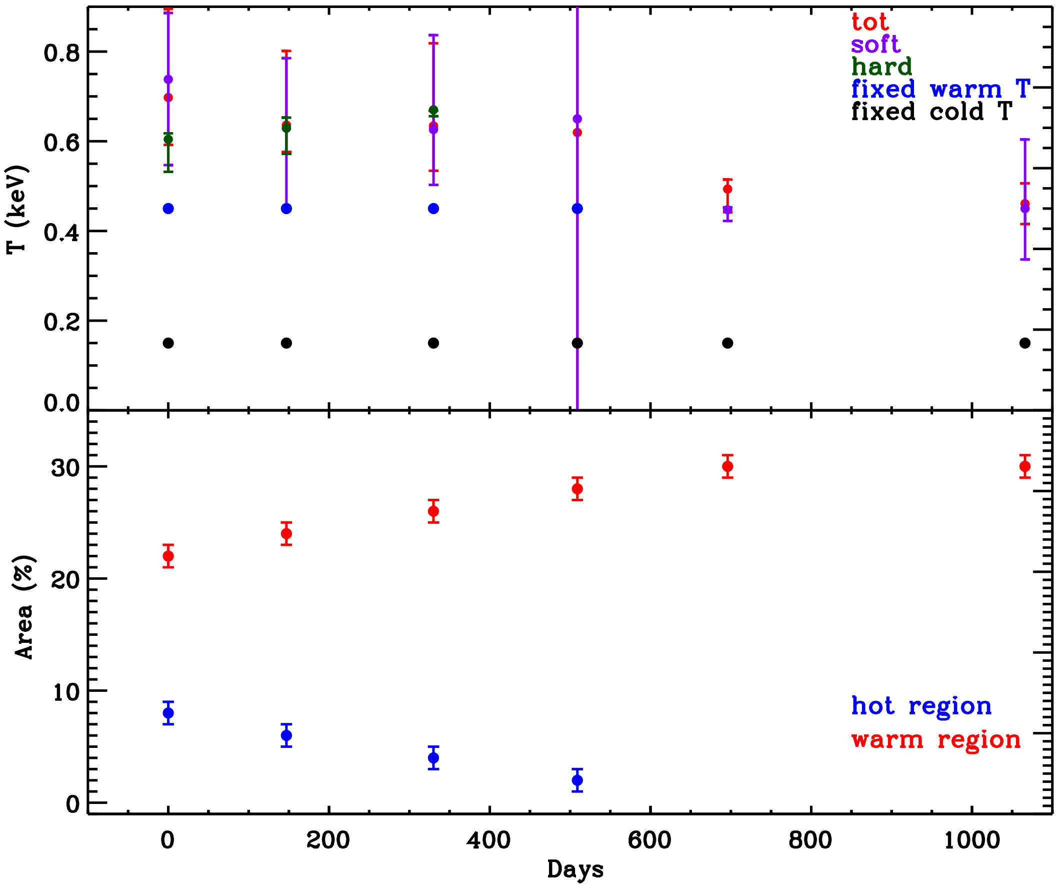

Figure 4.6: *On the top temperature trend (blue and black dots represent the fixed temperatures). On the bottom area of the different emitting regions (for the three energy band). Time is in days from September 2006 observation.*

perature $T_c \sim 0.15$ keV and its area remains constant at ~ 0.7 of the total. The twist angle is ~ 1.12 soon after the burst, then it decreases with time. There are hints that its decay is slower until August 2007, then proceeds faster. The electron velocity is about the same at all epoch ($\beta \sim 0.2$), apart from the last two observations for which β becomes greater. This variation may be related to the change in the pulse shape (from three-peaked to single-peaked) and also to the increase of the pulsed fraction. Comparison between observed and model pulse profiles is shown in Fig. 4.7. Because of the inherent complexity and drastic time evolution of CXOU J164710.2-455216 lightcurves, the agreement is not as good as for XTE J1810-197. Because of the complex shape of the pulse, no pulsed fraction analysis has been attempted for this source.

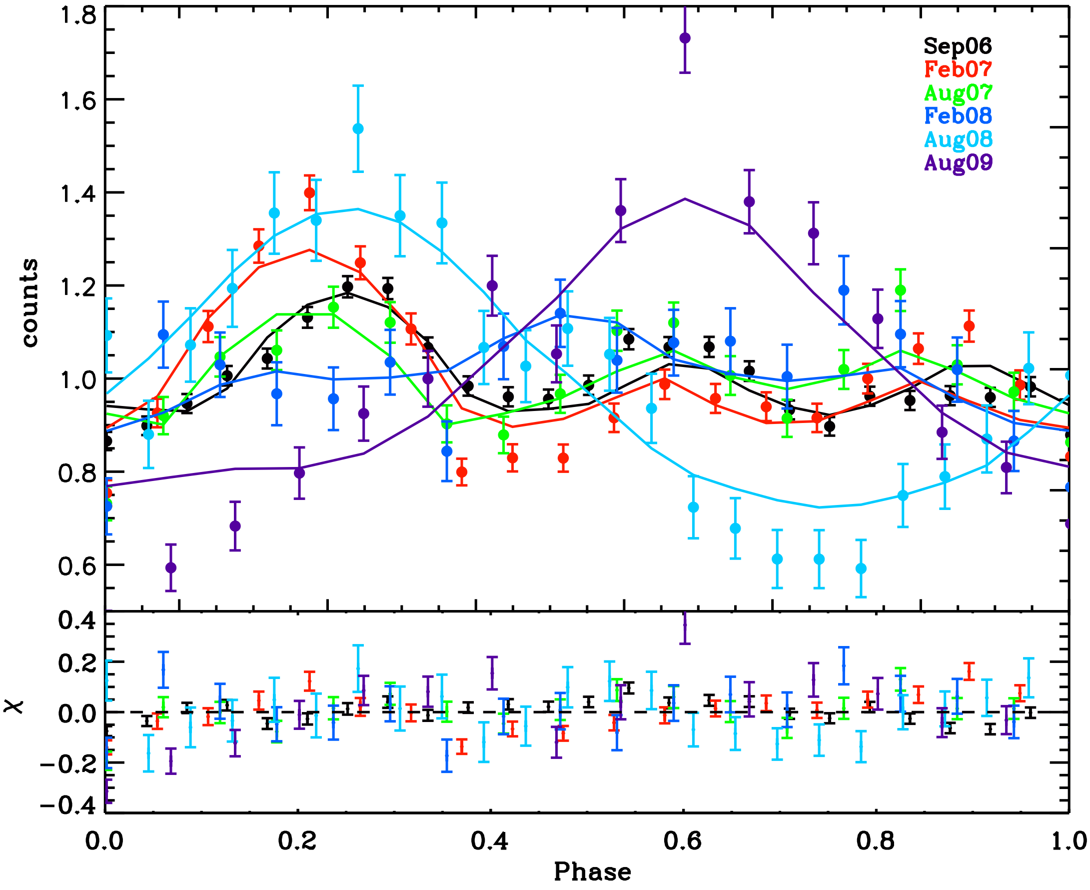

Figure 4.7: *Synthetic and observed pulse profiles for CXOU J164710.2-455216 in total energy band. Iniatial phases are arbitrary.*

As in XTE J1810-197, we made a further check to verify if values obtained from the minimization routine indeed correspond to minima of the reduced χ^2. Again we frozen five of the six parameters to the value obtained with the `mpcurvefit.pro` minimization routine, and calculated the reduced χ^2 for 100 values of the free parameter, around its minimum. The procedure has been repeated for all parameters and all observations on the three energy bands. According to XTE J1810-197, for all parameters but the temperature, results obtained with the `mpcurvefit.pro` routine indeed correspond to the minima of the reduced χ^2 curve (all CXOU J164710.2-455216 reduced χ^2 plots are showed in the appendix B). For the temperature case there is one observation for which the reduced χ^2 curve is very flat in all the energy bands. This is the August 2008 observation, for which the size of the emitting area accounts for just 2% of the total neutron star surface. As in XTE J1810-197, we conclude that the fit is not very sensible to temperature variation for too small emitting areas. As in the previous case it is possible to infer a value for the August 2008 warm temperature using the spectral analysis, which is more sensible to temperature variations with respect to the lightcurve one (see sect. 4.5).

4.5 The Spectra

The spectral analysis discussed in Sect. 3.5 was repeated for CXOU J164710.2-455216. We fitted three `ntzang` components, each representative of an emitting region at different temperature, freezing all parameters apart from the three normalizations and N_H (forced to be the same for all the components and for all epochs). Moreover, since for the February 2008 observation lightcurve analysis has not reported an unambiguous value for the hot temperature, also this parameter is left free to vary here. Results are shown in Fig. 4.8. Considering the approach we used for the fit, the agreement is very good; values for χ^2 are showed in Tab. 4.18. N_H is found to be $2.121\pm0.007\times10^{22}$ cm^{-2}.

4.6 Discussion

The application of our model to the TAXP CXOU J164710.2-455216 reveals an intial behaviour similar to XTE J1810-197 one. Infact, as in the previous case, soon after the burst CXOU J164710.2-455216 thermal map is maken of three regions. The hot cap acts just like in the AXP prototype case. But, contrary to the previous case,

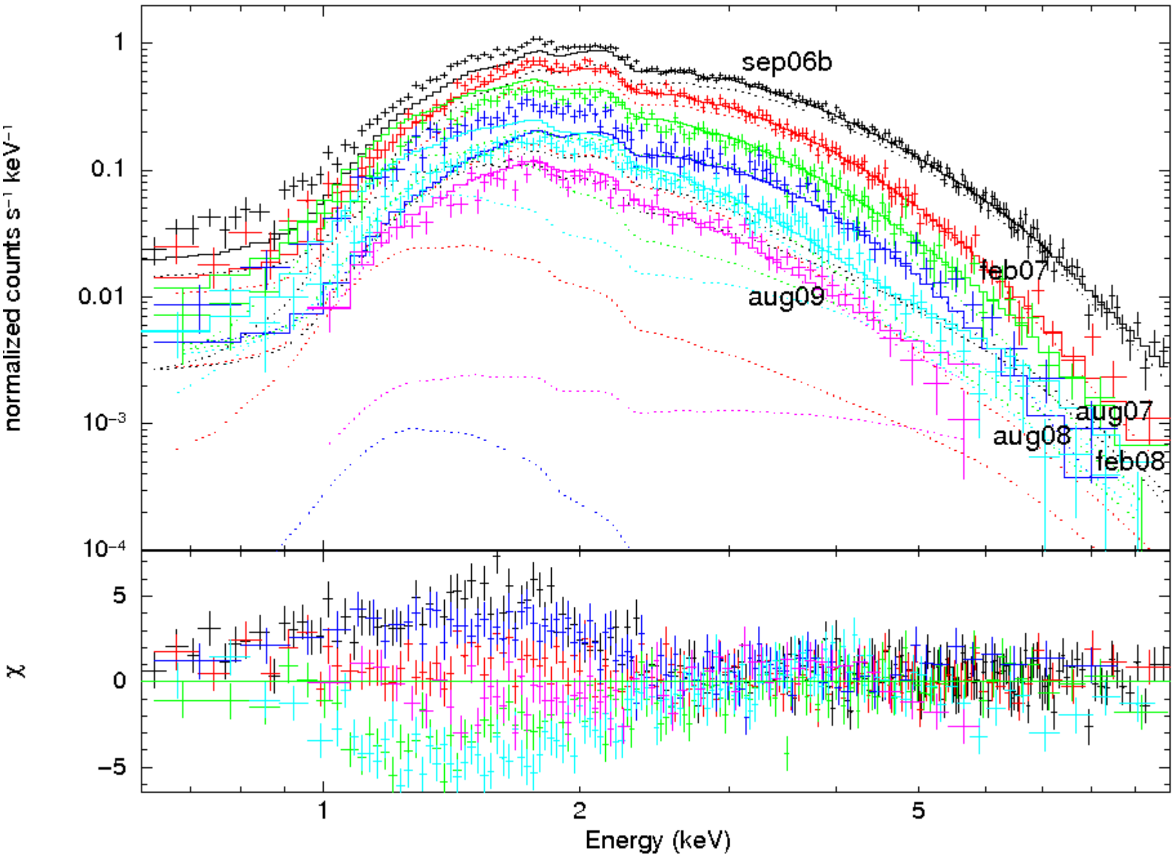

Figure 4.8: *CXOU J164710.2-455216 spectra at different epochs.*

Label	reduced χ^2
Sep 06	1.24
Feb 07	0.83
Aug 07	1.01
Feb 08	1.08
Aug 08	1.23
Aug 09	1.36

Table 4.18: *CXOU J164710.2-455216 reduced* χ^2 *values for spectral fitting.*

the study of the warm corona behaviour during the outburst shows an increase in the emitting area, even if the temperature remains constant at ~ 0.45 keV. A deeper analysis indicates that the sum of these two regions remain costant with time. This means that also the emitting area of the coolest region remain costant during all the outburst. Moreover in August 2008 observation, we are able to identify the hottest region no more. In this last two observations lightcurve feature change back to the pre-burst one. Matching these two informations we can make the hypotesis that CXOU J164710.2-455216 is reaching the quiescent state. We can also argue that this quiescent state is different from the XTE J1810-197 one, since it is constituted by two regions: a hot cap consists of 30% of the surface, and emitting at a temperature of ~ 0.45 keV, plus a coldest region, consists of 70% of the surface, and emitting at a temperature of ~ 0.15 keV.

Chapter 5

Conclusions

Among isolated neutron stars (INSs), a small number of objects, namely the Soft Gamma-ray Repeaters (SGRs) and the Anomalous X-ray Pulsars (AXPs), share a number of common, peculiar properties. These are the very narrow range of the rotational periods (2 - 12 s), the spin down rates $10^{-11} - 10^{-13}$ ss^{-1} and the persistent X-ray luminosities $L_X \sim 10^{34} - 10^{36}$ ergs^{-1}. Though SGRs activity is higher, both groups exhibit unpredictable X/γ ray bursts with peak luminosity $\sim 10^{37} - 10^{41}$ ergs^{-1} and typical duration of $\sim 0.1 - 1$ s. In the last years Transient phenomena have been observed from AXPs (1E 2259, XTE J1810-197, CXOU J164710.2-455216, 1E 1547.0-5408), with X-ray luminosities increase between few tens and few hundreds times their quiescent values.

At variance with radio pulsars, the persistent emission from SGRs and AXPs is $\sim 10 - 100$ times higher than their rotational losses. Moreover they lack a stellar companion, this indicating that the persistent emission for these sources can not be powered by rotation or accretion. Magnetic fields inferred from the periods $P$and periods derivatives $\dot{P}$ are in the range $\sim 10^{14} - 10^{15}$ G, one or two orders of magnitude in excess with respect to the quantum critical magnetic field ($B_{QED} = 4.4 \times 10^{13}$ G), strongly supporting the idea that these are ultra-magnetized neutron stars (*Magnetars*; Duncan & Thompson 1992; Thompson & Duncan 1993), whose persistent X-ray emission is supported by the super-strong magnetic field. There is an increasing number of theoretical and observational evidences that *Magnetars* external magnetic field can contain a toroidal component, causing the magnetosphere to twist up ($\nabla \times \mathbf{B} \neq 0$). Twisted magnetospheres are threated by currents flowing along the closed field lines which efficiently interacts with soft thermal photons via resonant cyclotron scattering (RCS). The RCS model basic idea has been initially discussed by Thompson, Lyutikov, &

Kulkarni (2002), and then approched by Lyutikov, & Gavriil (2006), Fernandez, & Thompson (2007) and Nobili, Turolla, & Zane (2008). Actually the most advanced tool to compute AXPs and SGRs spectra with the RCS model is the Nobili, Turolla, & Zane 2008, or NTZ, 3D montecarlo simulation. This model allows to correctly describe timing and spectral *Magnetar* properties in terms of five parameters: the twist angle $\Delta\phi$, the electron bulk velocity β, the photon temperature T, the misallignement betweeen magnetic and spin axis ξ and the inclination of the line of sight with respect to the spin axis χ. In this thesis the NTZ model has been applied to two transient AXPs (TAXPs) for which a large enough number of *XMM-Newton* observations covering all the outburst decay are available.

The monitoring of the two TAXPs XTE J1810-197 and CXOU J164710.2-455216 over the last years gives the possibility to understand the physical values of outburst evolution for both sources. In both cases soon after the outburst onset the source is well described by a three temperature thermal map: a hot cap, a warm corona around the hot spot and the rest of the neutron star surface at a cooler temperature. The analysis of the lightcurves evolution revealed different thermal map characteristics. In XTE J1810-197 both the hot cap and the warm corona decrease in size so that in the last observation (September 2007) the 99.5% of the neutron star surface emits at a temperature compatible with the quiescent one (measured in the '90s by ROSAT). On the contrary in CXOU J164710.2-455216 the hot cap decreases in temperature and size, while the warm corona remains constant in temperature and increases in size. In the last two observations we examined (August 2008 and August 2009) the object has a thermal map made by a hot cap covering the 30% of the neutron star surface, and the rest of the surface at a cooler temperature. There are hints that this could be the quiescent state for this Transient AXP.

For both sources the twist angle reaches the maximum value soon after the outburst onset and then monothonically decreases with time. The magnetosphere relaxes in a few years. In XTE J1810-197 the twist angle reaches the value of ~ 0.50 rad after two years, and then remains constant. In CXOU J165710.2-455216 the twist angle decrease continues over all the three monitoring years. Most importantly of all for both TAXPs fits produce values of the two geometrical angles ξ and χ which are, at all epochs, compatible within 1σ errors.

The thermal map together with the values for twist angle, electron bulk velocity, geometrical angles which best-fit the observed lightcurves can be also used to describe spectra in $0.1 - 10$ keV band. For both sources the agreement between simulated and observed spectra is good.

This thesis adds further support to the idea that resonant cyclotron scattering model correctly describes timing and spectral properties of Transient AXPs during the post-outburst evolution. Nowdays the model has been successfully applied to the two TAXPs XTE J1810-197 and CXOU J164710.2-455216. A preliminarly application of the model to the post-outburst of SGR 0501 has been done, finding promising results. In the future a systematic application to all post-outburst of Transient *Magnetars* will be done.

Appendix A

Reduced χ^2 plots for XTE J1810-197

Reduced χ^2 plots have been generated in order to verify if values obtained from the minimization routine indeed correspond to minima of the reduced χ^2. To do this five of the six parameters have been frozen to the value obtained with the `mpcurvefit.pro` minimization routine, and the reduced χ^2 is calculated for 100 values of the free parameter, around its minimum. If x_{min} is the value of the parameter obtained from the fit, then the reduced χ^2 curve should exhibit a minimum in correspondance of x_{min}. This procedure has been repeated for all parameters in the three energy bands. An exhaustive discussion about this plots is reported in Sect. 3.4

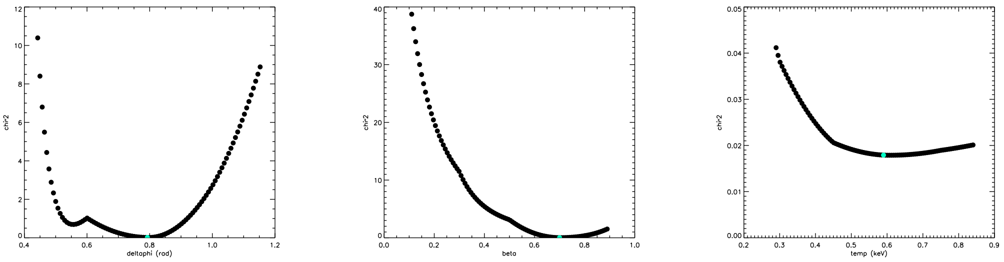

(a) $\Delta\phi$ (b) β (c) T

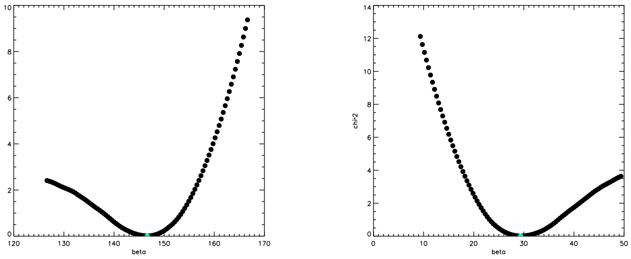

(d) χ (e) ξ

Figure A.1: *XTE J1810-197 September 2003 total band.*

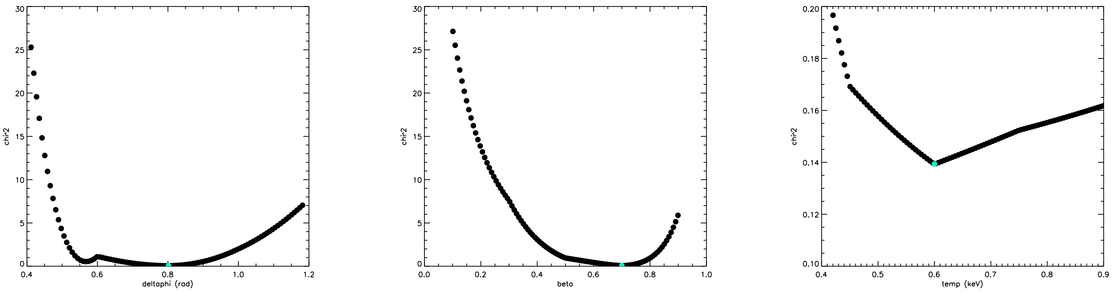

(a) $\Delta\phi$ (b) β (c) T

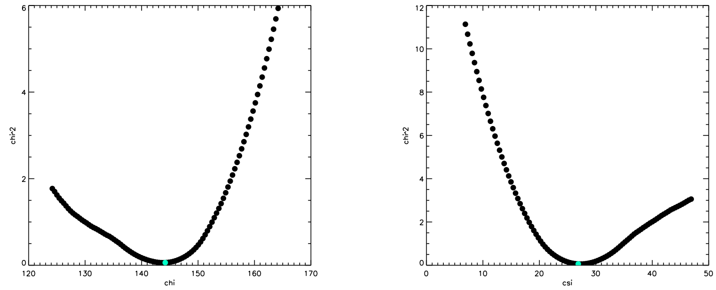

(d) χ (e) ξ

Figure A.2: *XTE J1810-197 September 2003 soft band.*

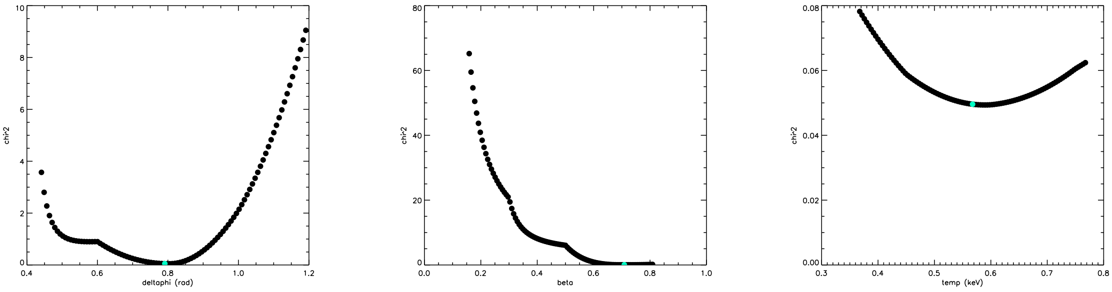

(a) $\Delta\phi$ (b) β (c) T

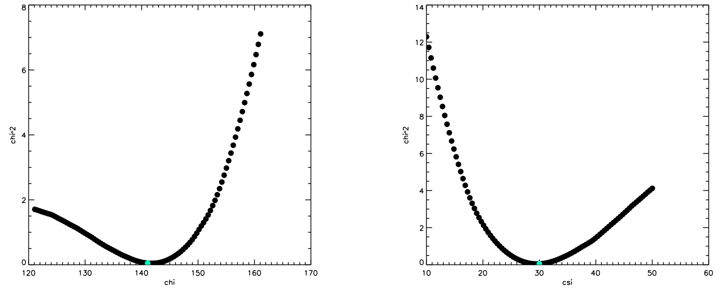

(d) χ (e) ξ

Figure A.3: *XTE J1810-197 September 2003 hard band.*

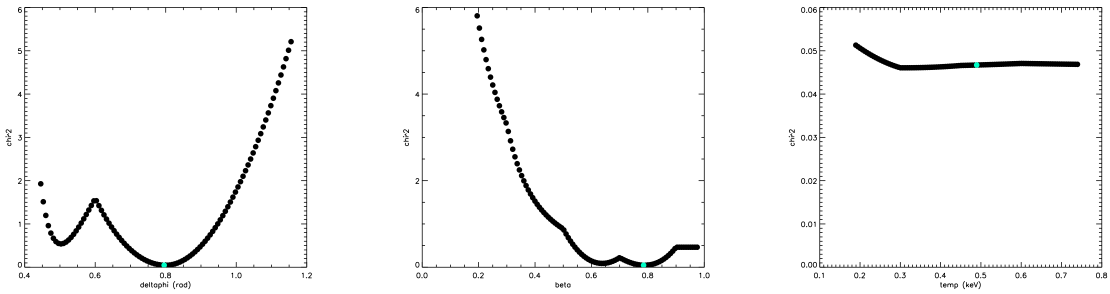

(a) $\Delta\phi$ (b) β (c) T

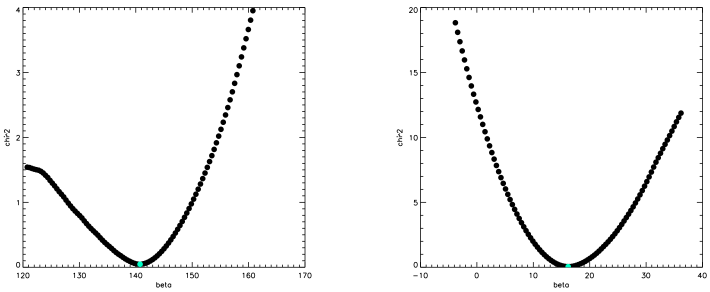

(d) χ (e) ξ

Figure A.4: *XTE J1810-197 September 2004 total band.*

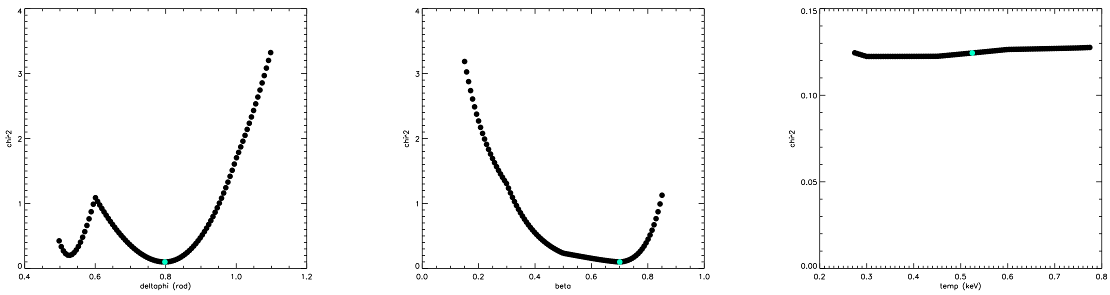

(a) $\Delta\phi$ (b) β (c) T

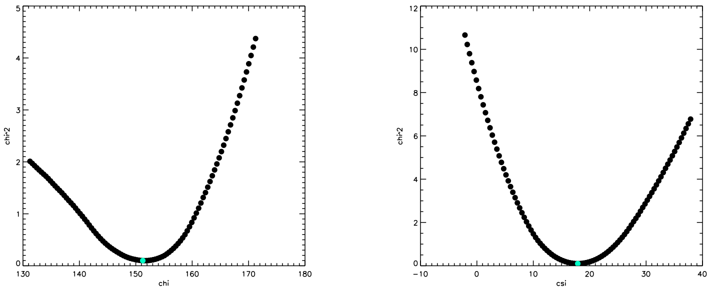

(d) χ (e) ξ

Figure A.5: *XTE J1810-197 September 2004 soft band.*

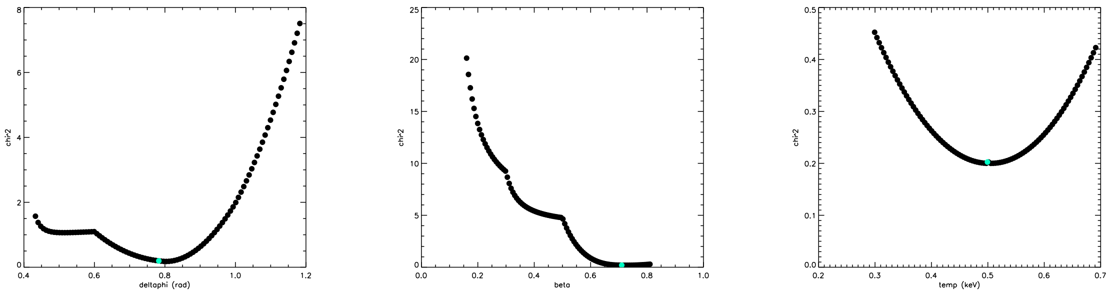

(a) $\Delta\phi$ (b) β (c) T

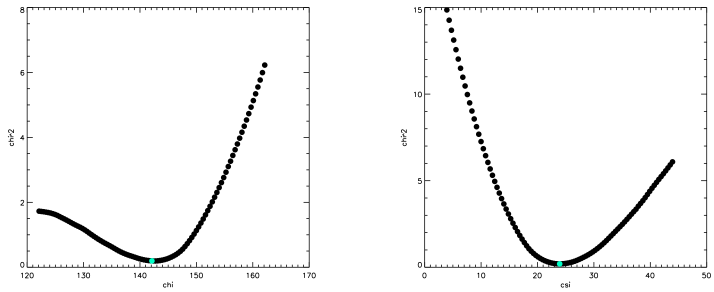

(d) χ (e) ξ

Figure A.6: *XTE J1810-197 September 2004 hard band.*

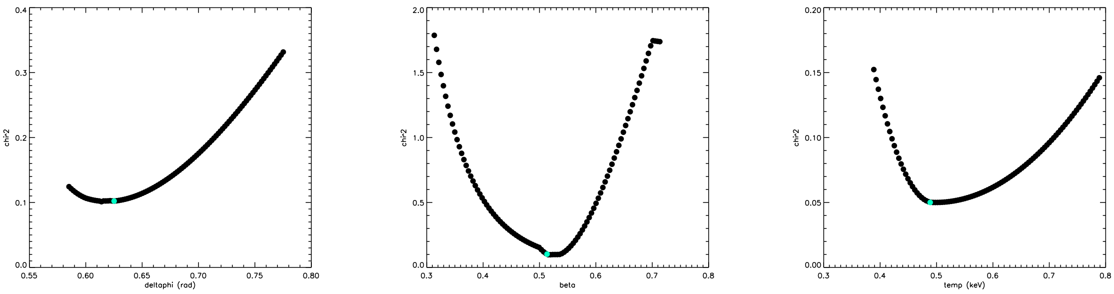

(a) $\Delta\phi$ (b) β (c) T

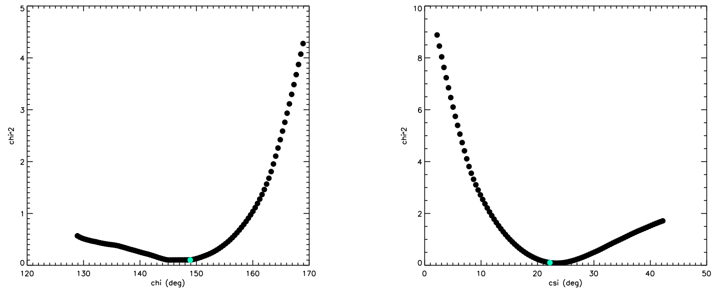

(d) χ (e) ξ

Figure A.7: *XTE J1810-197 March 2005 total band.*

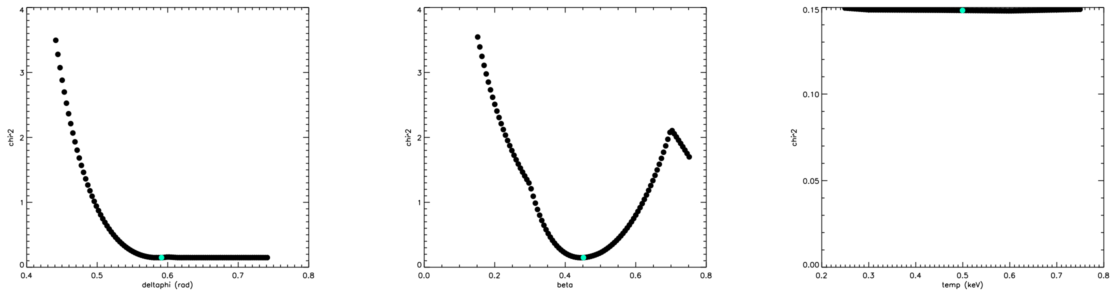

(a) $\Delta\phi$ (b) β (c) T

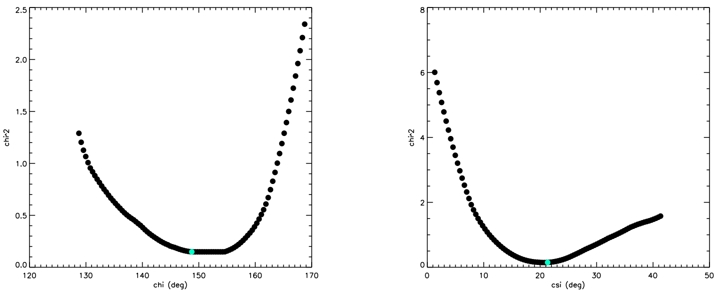

(d) χ (e) ξ

Figure A.8: *XTE J1810-197 March 2005 soft band.*

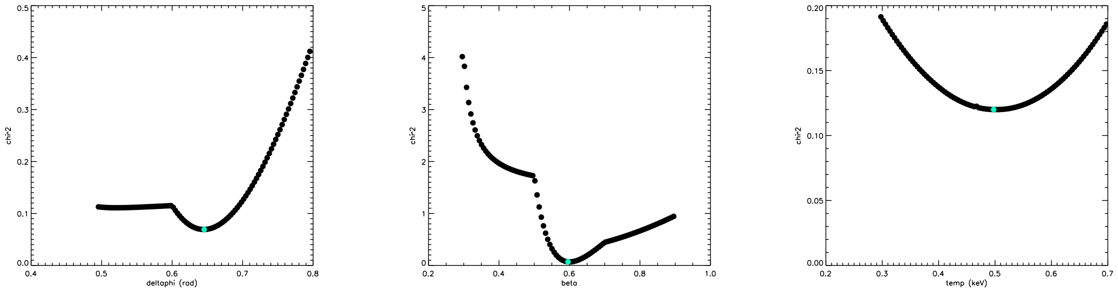

(a) $\Delta\phi$ (b) β (c) T

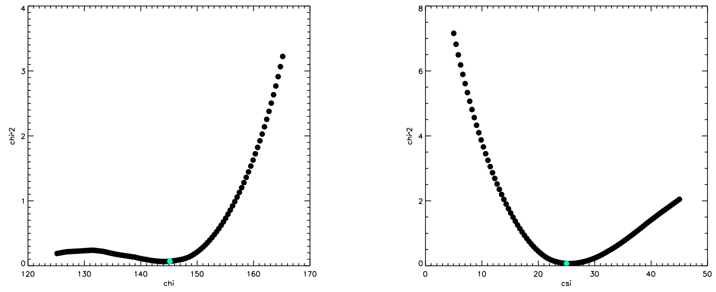

(d) χ (e) ξ

Figure A.9: *XTE J1810-197 March 2005 hard band.*

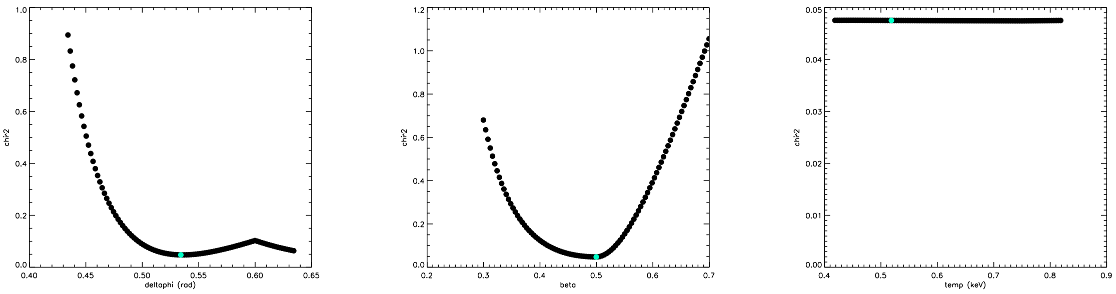

(a) $\Delta\phi$ (b) β (c) T

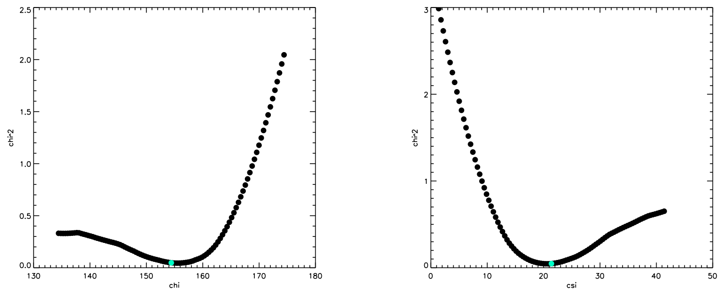

(d) χ (e) ξ

Figure A.10: *XTE J1810-197 September 2005 total band.*

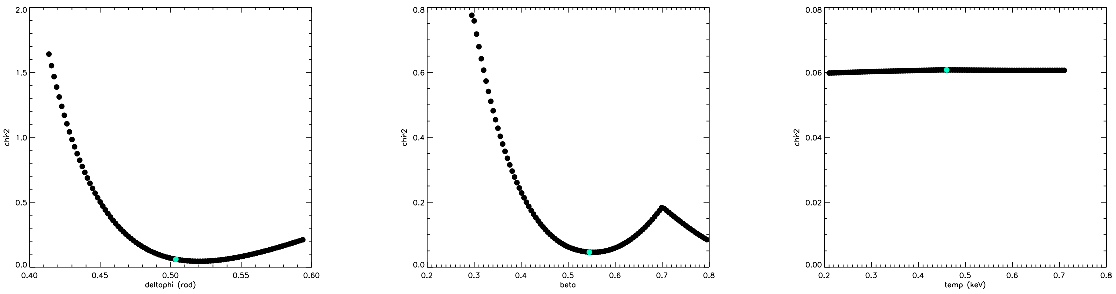

(a) $\Delta\phi$ (b) β (c) T

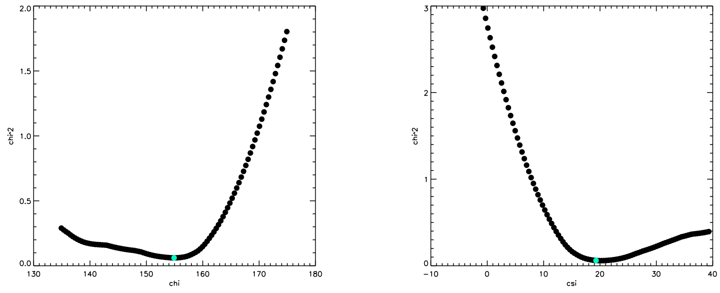

(d) χ (e) ξ

Figure A.11: *XTE J1810-197 September 2005 soft band.*

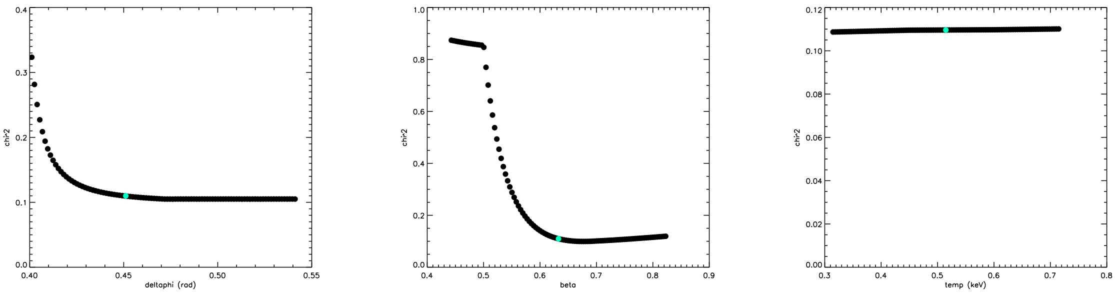

(a) $\Delta\phi$ (b) β (c) T

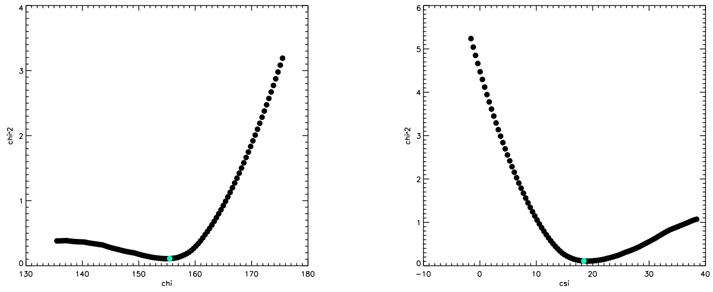

(d) χ (e) ξ

Figure A.12: *XTE J1810-197 September 2005 hard band.*

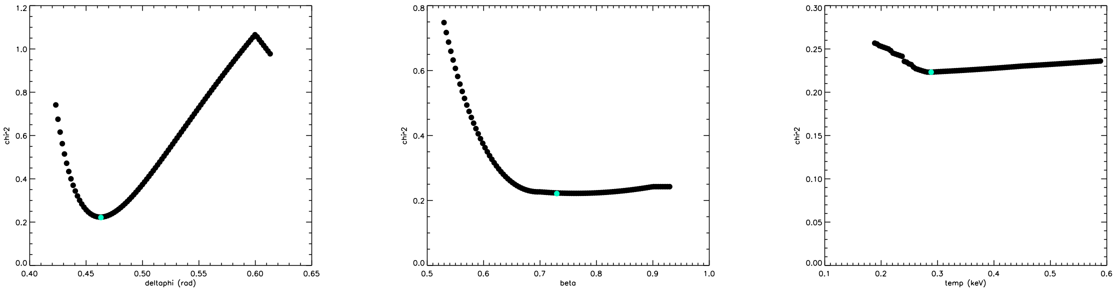

(a) $\Delta\phi$ (b) β (c) T

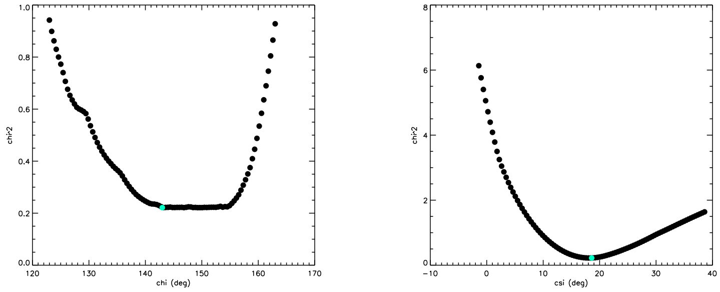

(d) χ (e) ξ

Figure A.13: *XTE J1810-197 March 2006 total band.*

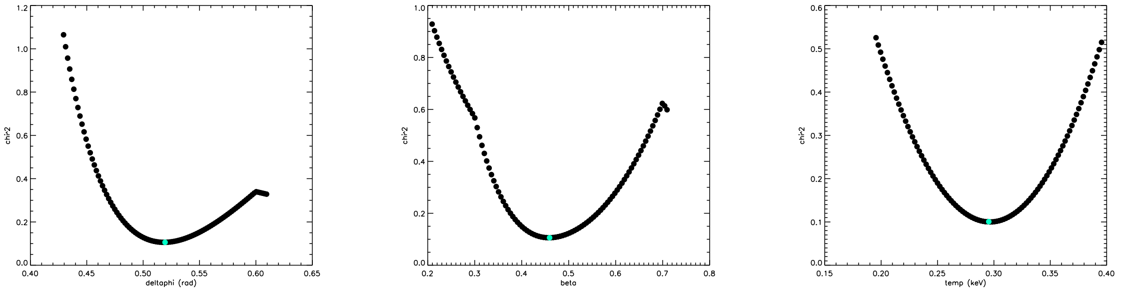

(a) $\Delta\phi$ (b) β (c) T

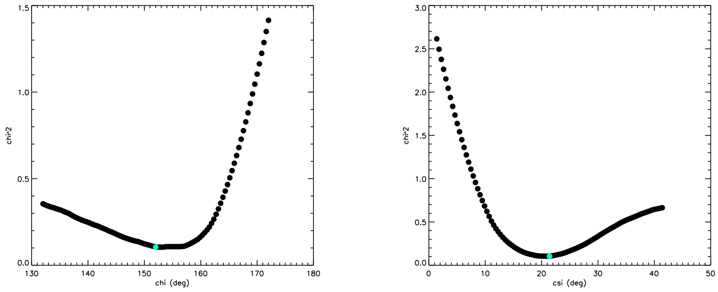

(d) χ (e) ξ

Figure A.14: *XTE J1810-197 March 2006 soft band.*

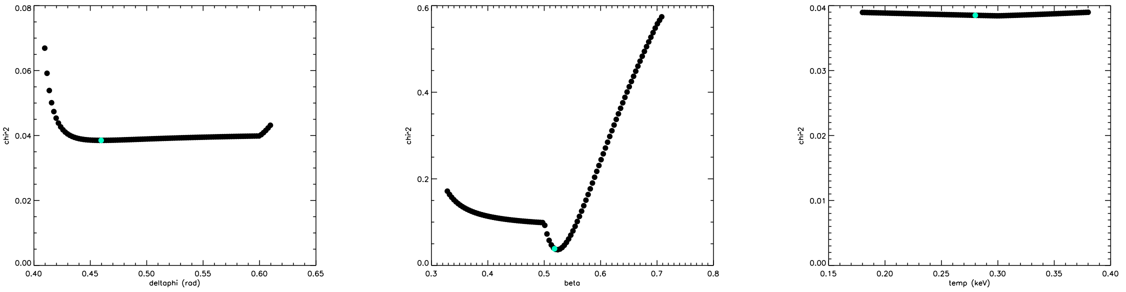

(a) $\Delta\phi$ (b) β (c) T

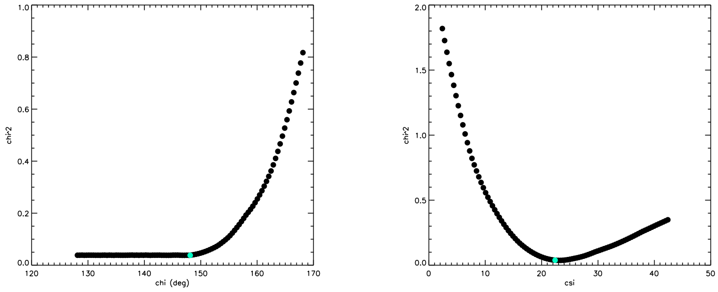

(d) χ (e) ξ

Figure A.15: *XTE J1810-197 March 2006 hard band.*

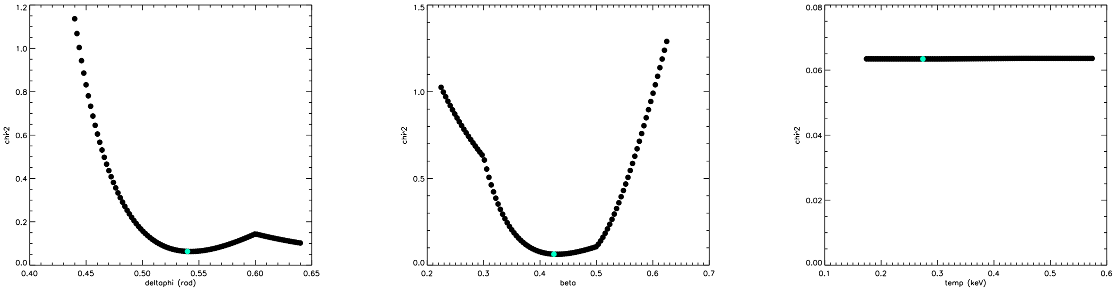

(a) $\Delta\phi$ (b) β (c) T

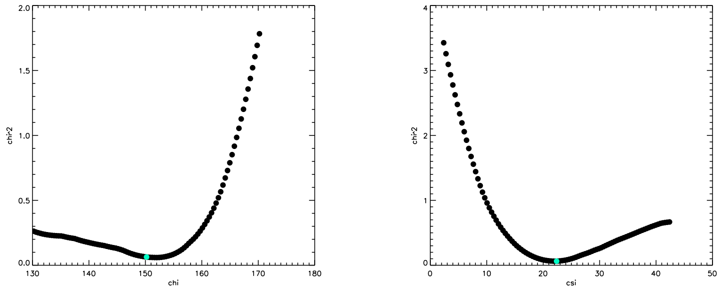

(d) χ (e) ξ

Figure A.16: *XTE J1810-197 September 2006 total band.*

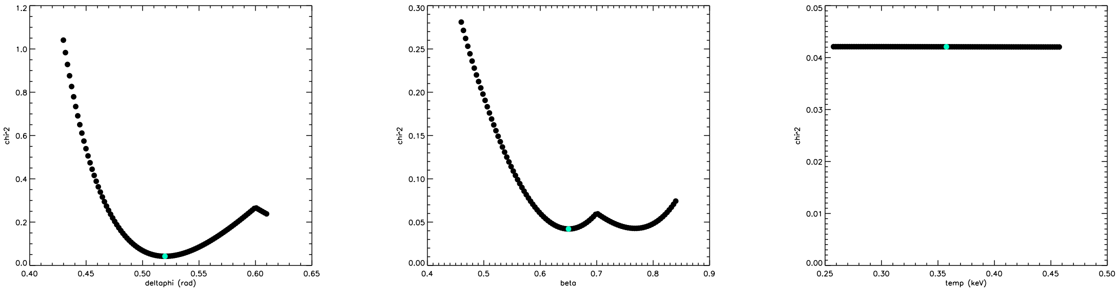

(a) $\Delta\phi$ (b) β (c) T

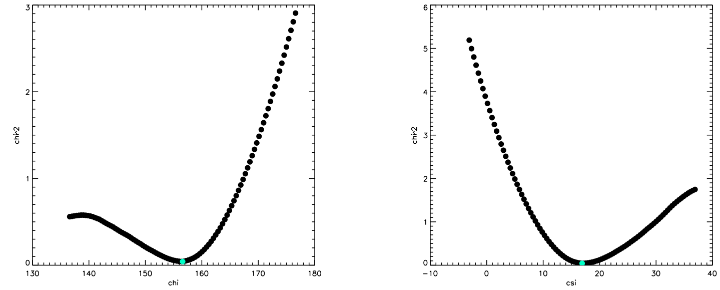

(d) χ (e) ξ

Figure A.17: *XTE J1810-197 September 2006 soft band.*

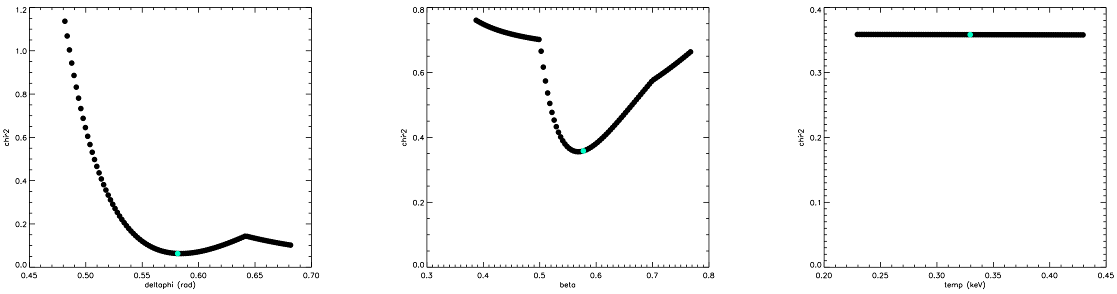

(a) $\Delta\phi$ (b) β (c) T

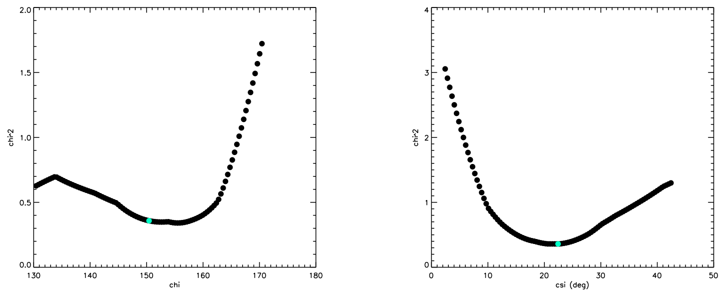

(d) χ (e) ξ

Figure A.18: *XTE J1810-197 September 2006 hard band.*

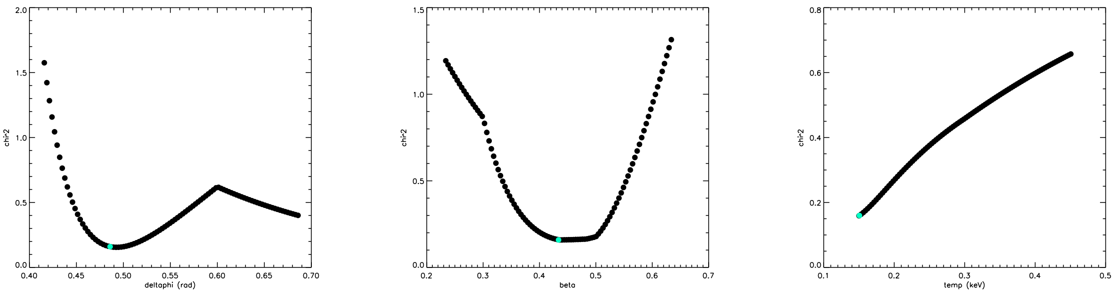

(a) $\Delta\phi$ (b) β (c) T

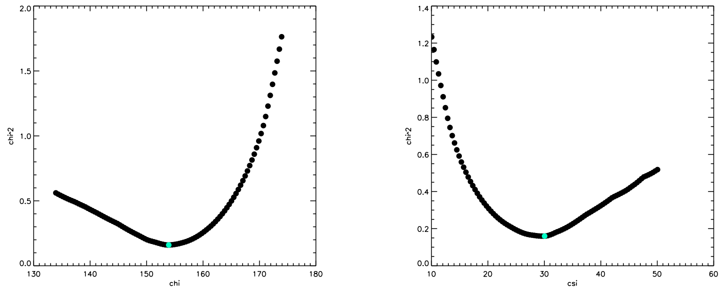

(d) χ (e) ξ

Figure A.19: *XTE J1810-197 March 2007 total band.*

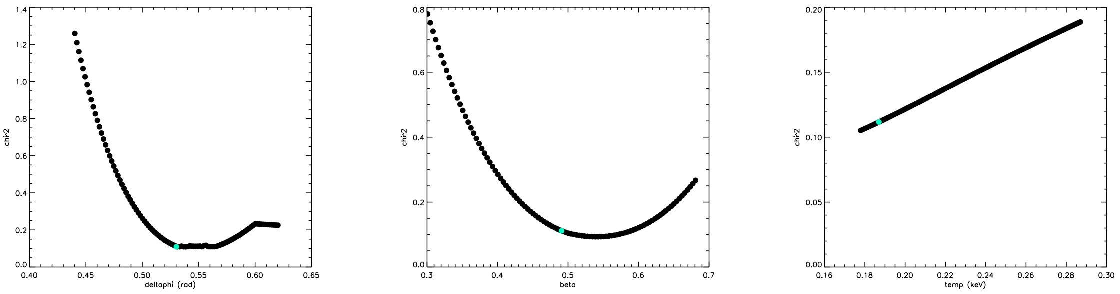

(a) $\Delta\phi$ (b) β (c) T

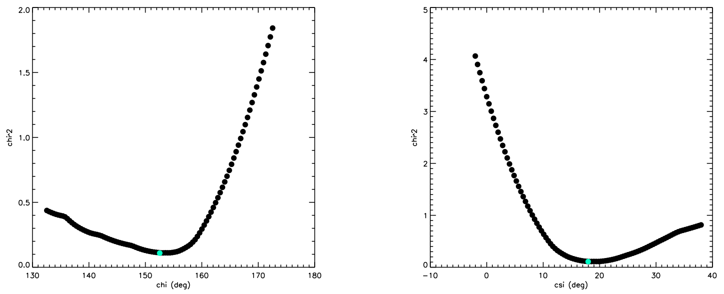

(d) χ (e) ξ

Figure A.20: *XTE J1810-197 March 2007 soft band.*

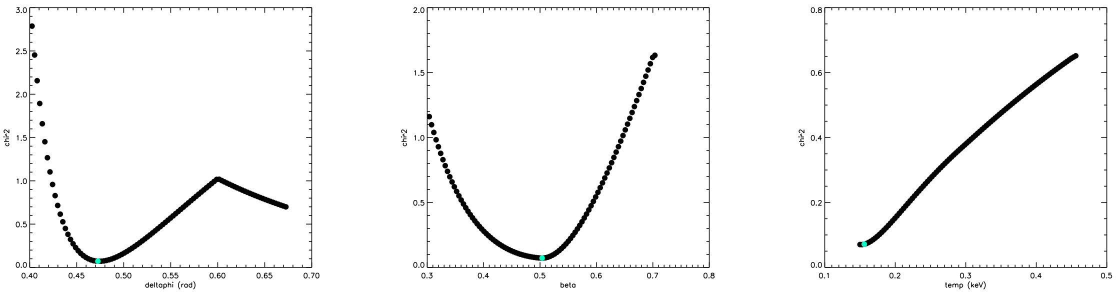

(a) $\Delta\phi$ (b) β (c) T

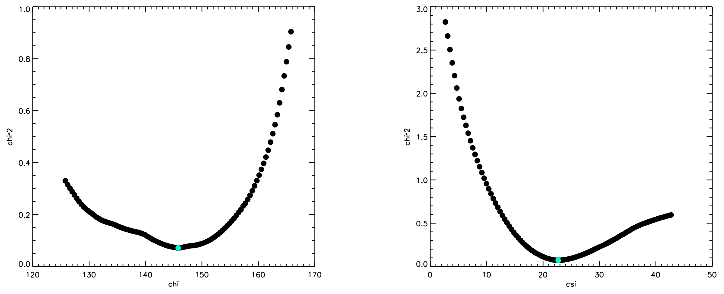

(d) χ (e) ξ

Figure A.21: *XTE J1810-197 September 2007 total band.*

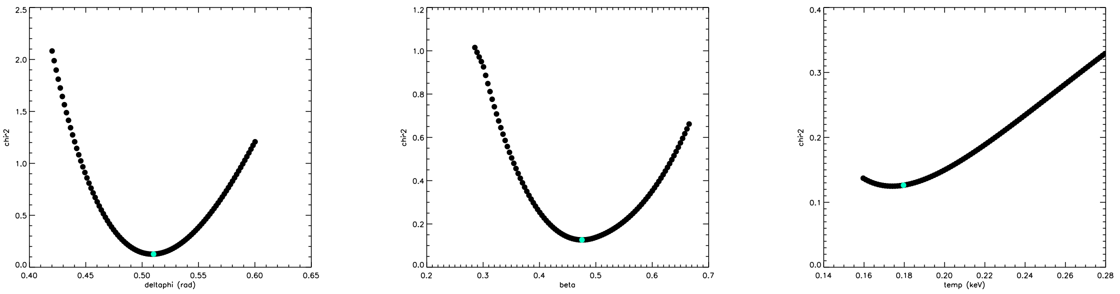

(a) $\Delta\phi$ (b) β (c) T

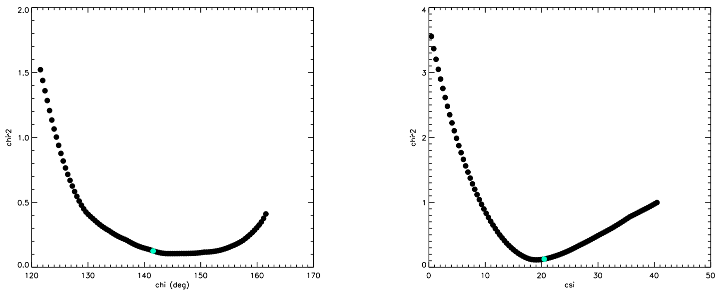

(d) χ (e) ξ

Figure A.22: *XTE J1810-197 September 2007 soft band.*

Appendix B

Reduced χ^2 plots for CXOU J164710.2-455216

Reduced χ^2 plots have been generated in order to verify if values obtained from the minimization routine indeed correspond to minima of the reduced χ^2. To do this five of the six parameters have been frozen to the value obtained with the `mpcurvefit.pro` minimization routine, and the reduced χ^2 is calculated for 100 values of the free parameter, around its minimum. If x_{min} is the value of the parameter obtained from the fit, then the reduced χ^2 curve should exhibit a minimum in correspondance of x_{min}. This procedure has been repeated for all parameters in the three energy bands. An exhaustive discussion about this plots is reported in Sect. 4.4

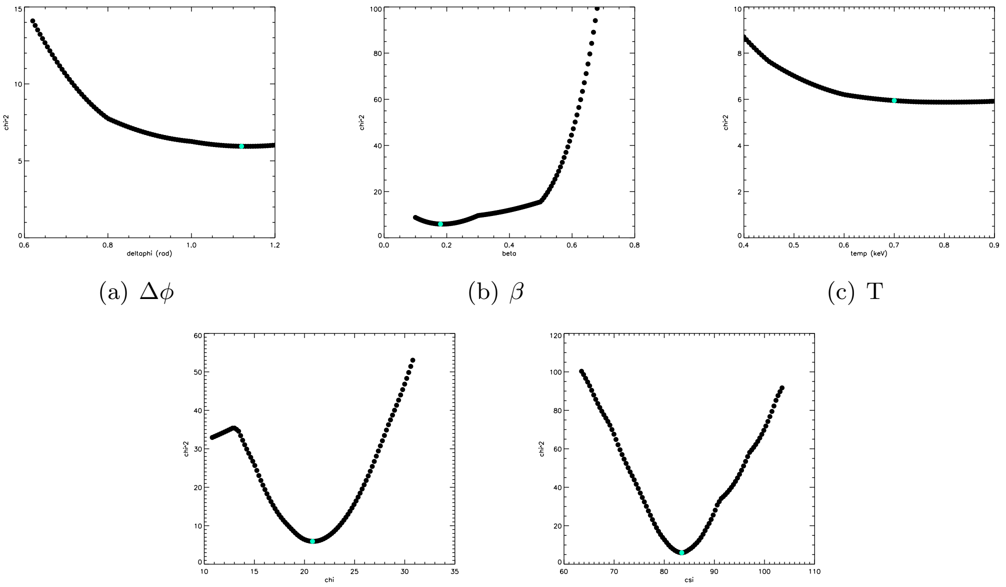

(a) $\Delta\phi$ (b) β (c) T

(d) χ (e) ξ

Figure B.1: *CXOU J164710.2-455216 September 2006 total band.*

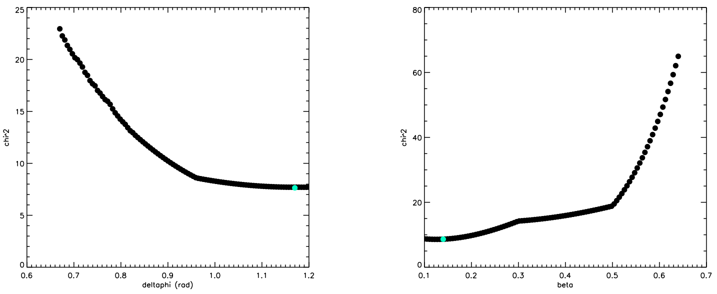

(a) $\Delta\phi$ (b) β (c) T

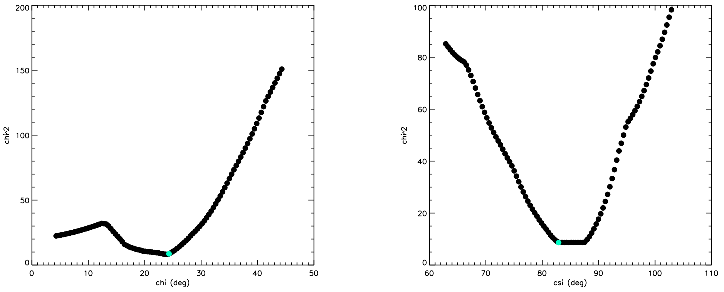

(d) χ (e) ξ

Figure B.2: *CXOU J164710.2-455216 September 2006 soft band.*

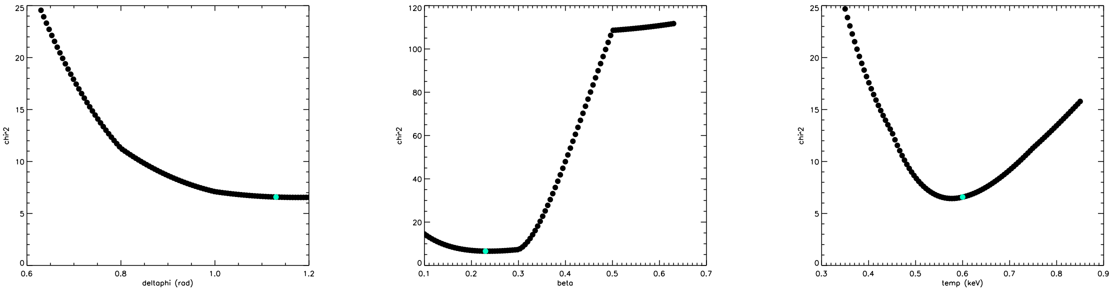

(a) $\Delta\phi$ (b) β (c) T

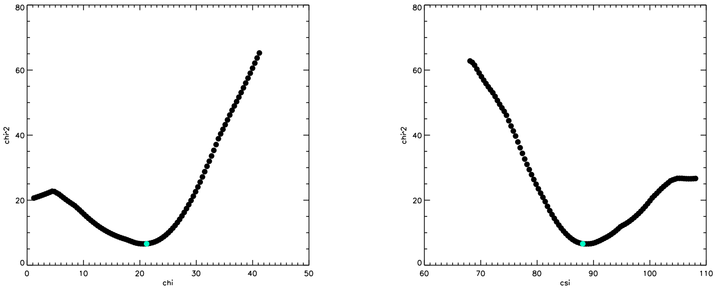

(d) χ (e) ξ

Figure B.3: *CXOU J164710.2-455216 September 2006 hard band.*

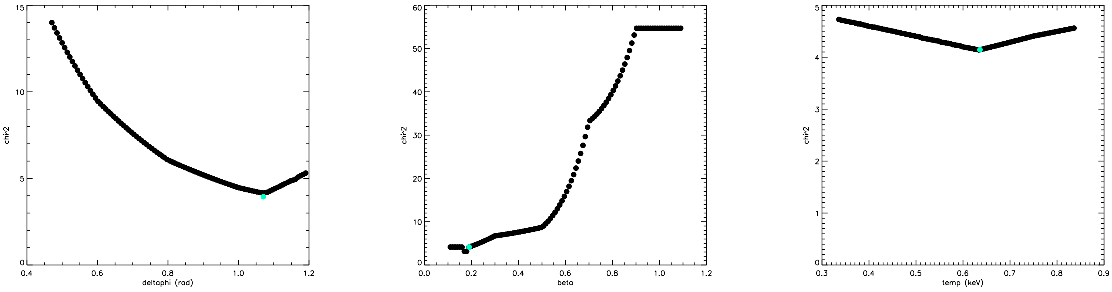

(a) $\Delta\phi$ (b) β (c) T

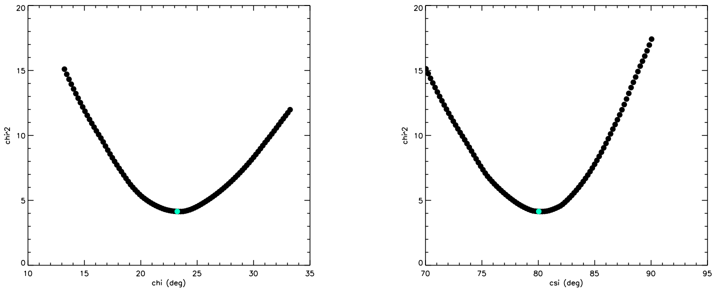

(d) χ (e) ξ

Figure B.4: *CXOU J164710.2-455216 February 2007 total band.*

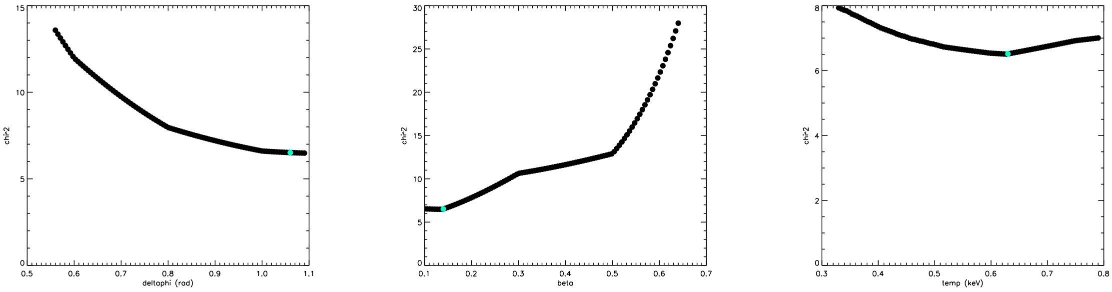

(a) $\Delta\phi$ (b) β (c) T

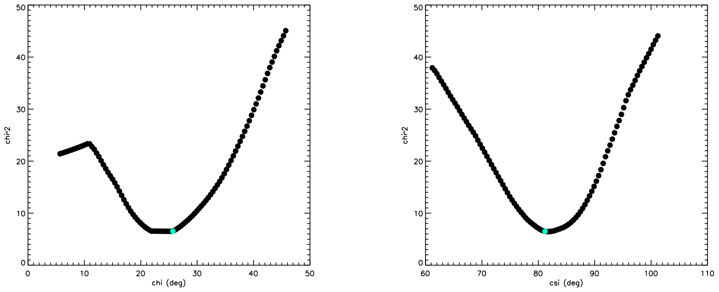

(d) χ (e) ξ

Figure B.5: *CXOU J164710.2-455216 February 2007 soft band.*

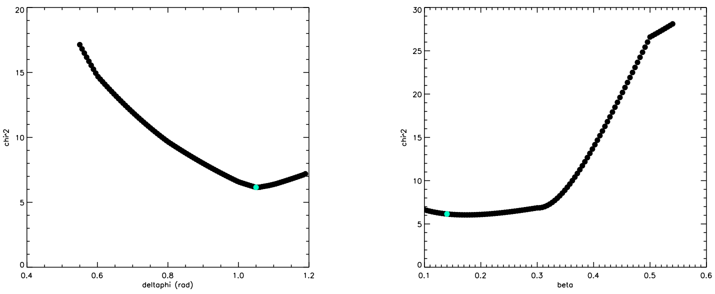

(a) $\Delta\phi$ (b) β (c) T

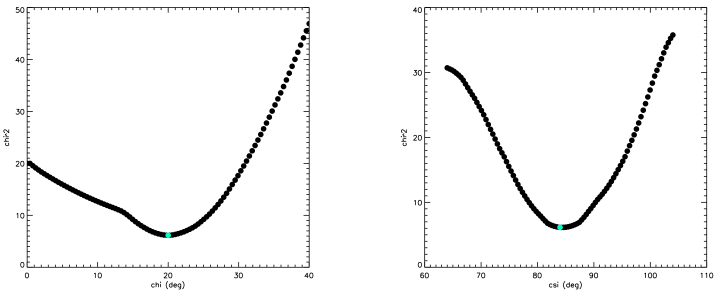

(d) χ (e) ξ

Figure B.6: *CXOU J164710.2-455216 February 2007 hard band.*

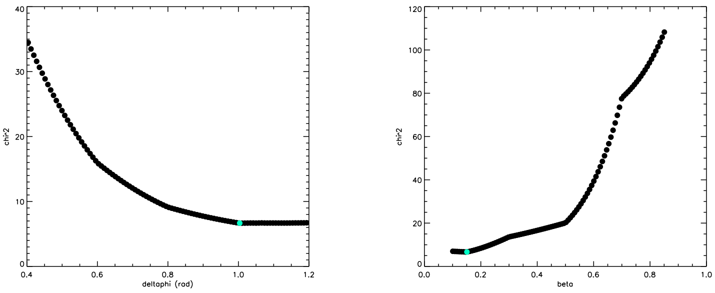

(a) $\Delta\phi$ (b) β (c) T

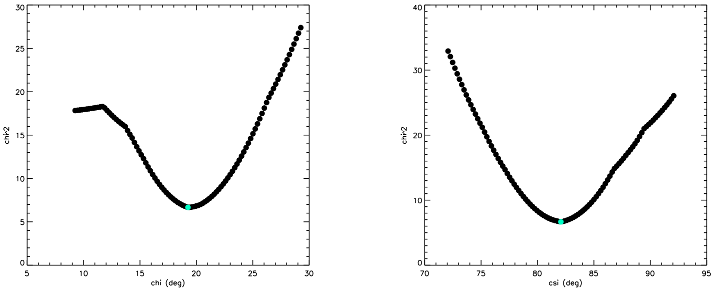

(d) χ (e) ξ

Figure B.7: *CXOU J164710.2-455216 August 2007 total band.*

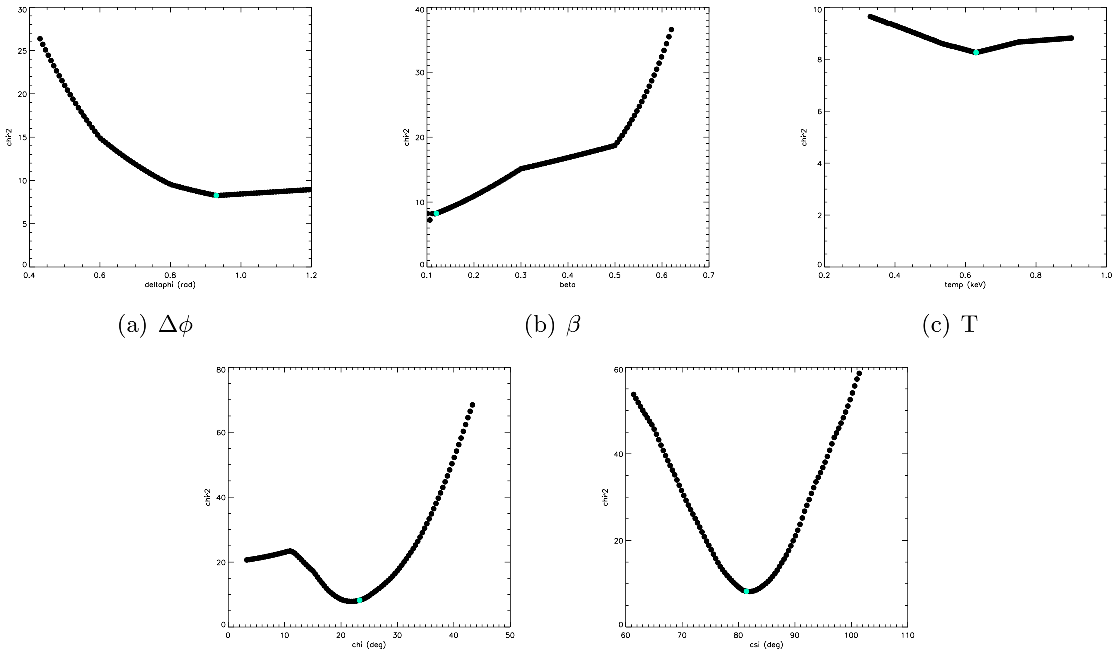

(a) $\Delta\phi$ (b) β (c) T

(d) χ (e) ξ

Figure B.8: *CXOU J164710.2-455216 August 2007 soft band.*

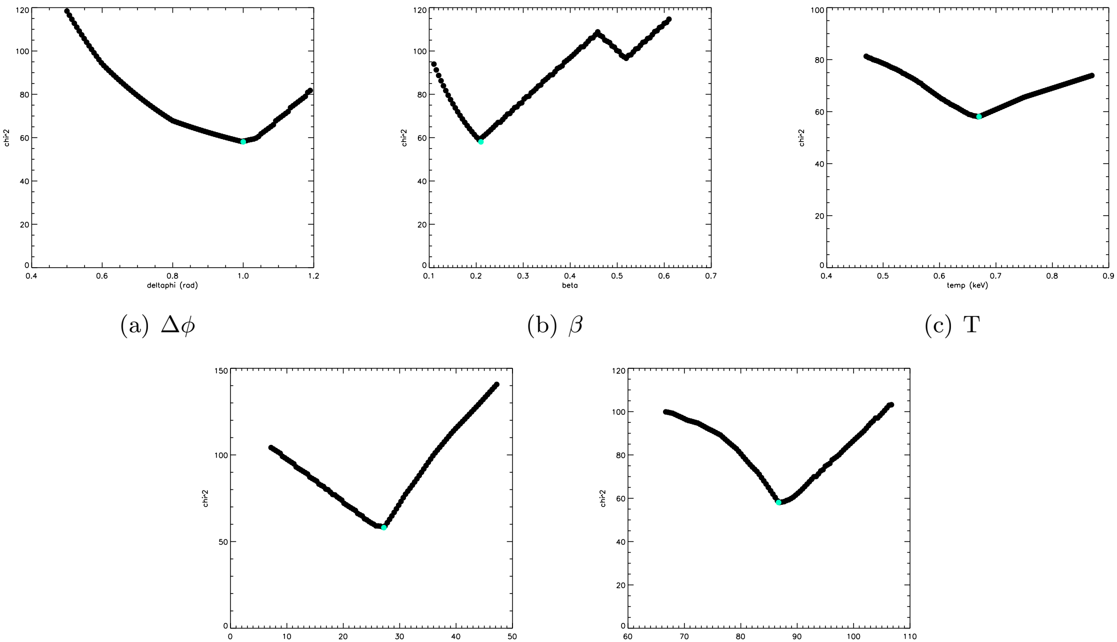

(a) $\Delta\phi$ (b) β (c) T

(d) χ (e) ξ

Figure B.9: *CXOU J164710.2-455216 August 2007 hard band.*

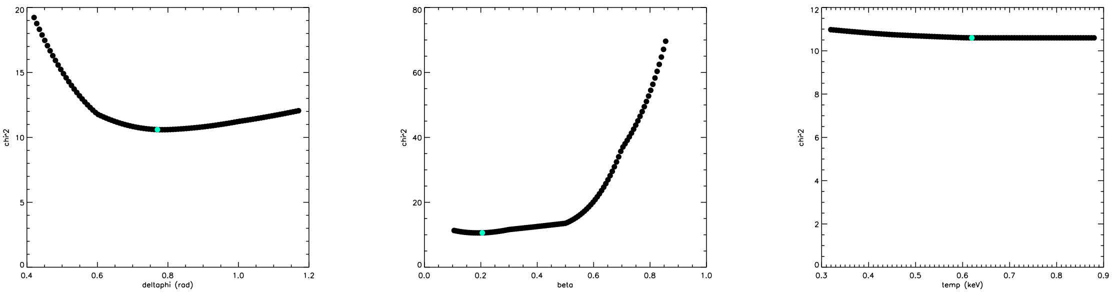

(a) $\Delta\phi$ (b) β (c) T

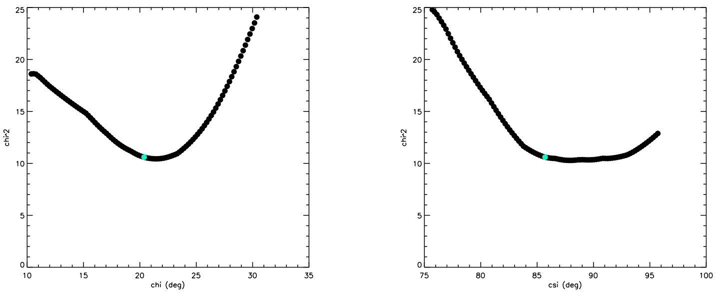

(d) χ (e) ξ

Figure B.10: *CXOU J164710.2-455216 February 2008 total band.*

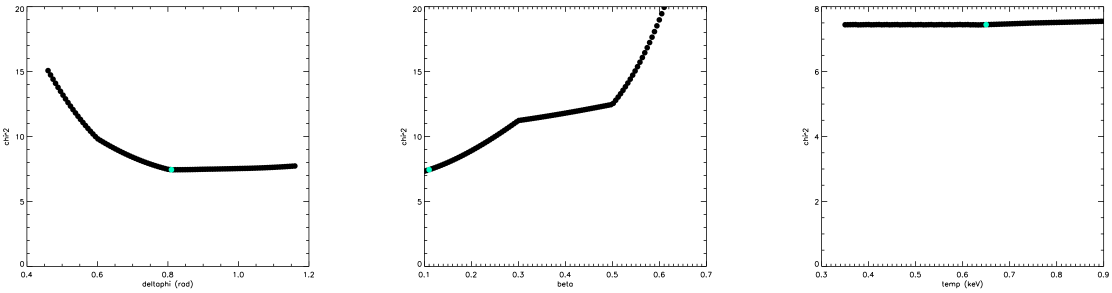

(a) $\Delta\phi$ (b) β (c) T

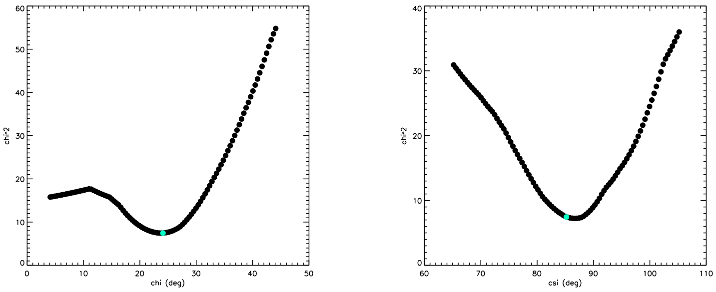

(d) χ (e) ξ

Figure B.11: *CXOU J164710.2-455216 February 2008 soft band.*

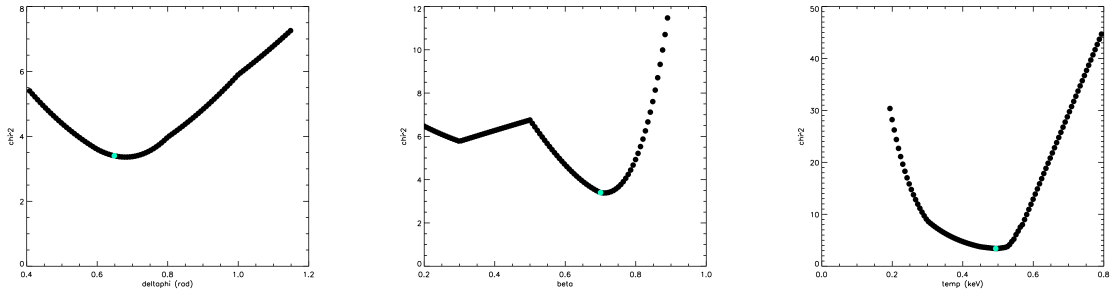

(a) $\Delta\phi$ (b) β (c) T

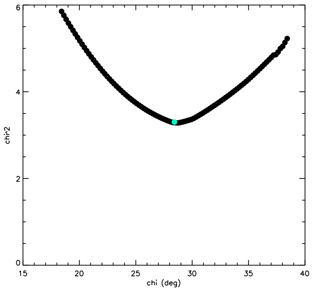

(d) χ (e) ξ

Figure B.12: *CXOU J164710.2-455216 August 2008 total band.*

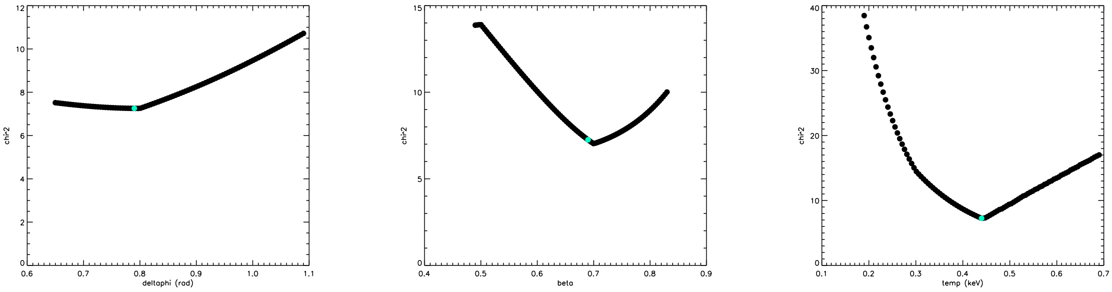

(a) $\Delta\phi$ (b) β (c) T

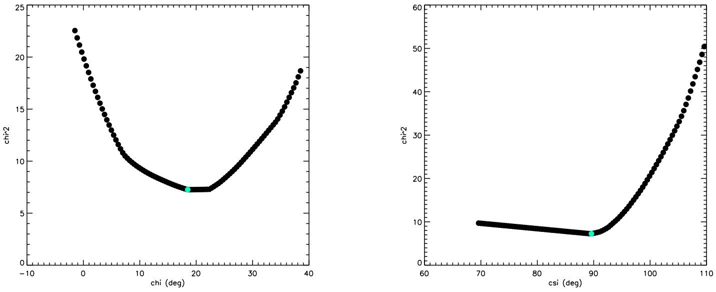

(d) χ (e) ξ

Figure B.13: *CXOU J164710.2-455216 August 2008 soft band.*

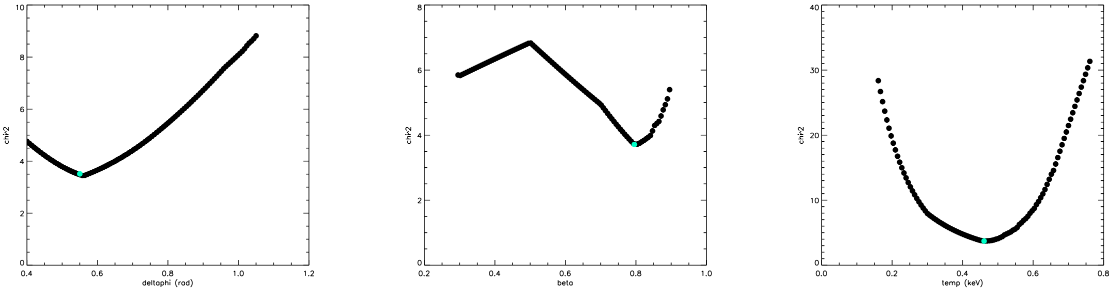

(a) $\Delta\phi$ (b) β (c) T

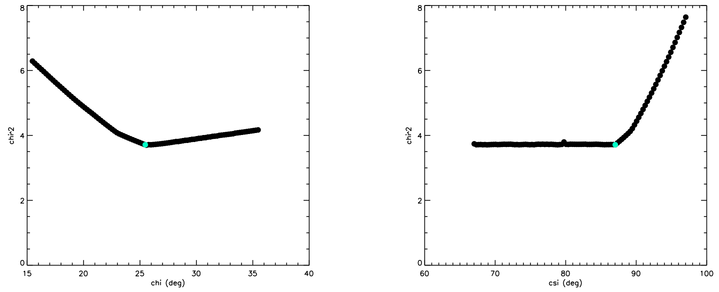

(d) χ (e) ξ

Figure B.14: *CXOU J164710.2-455216 August 2009 total band.*

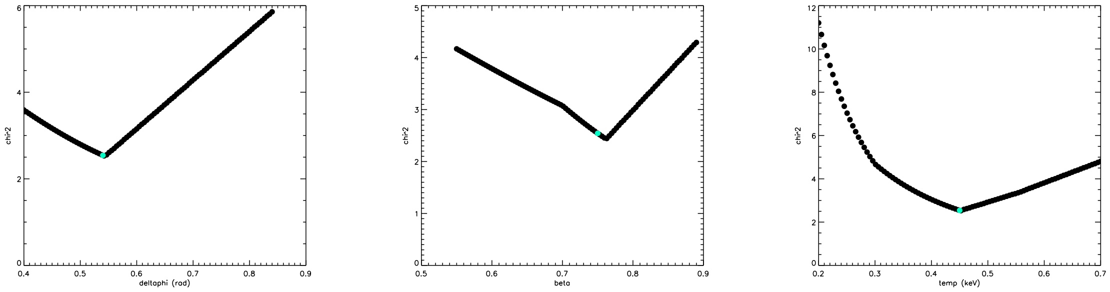

(a) $\Delta\phi$ (b) β (c) T

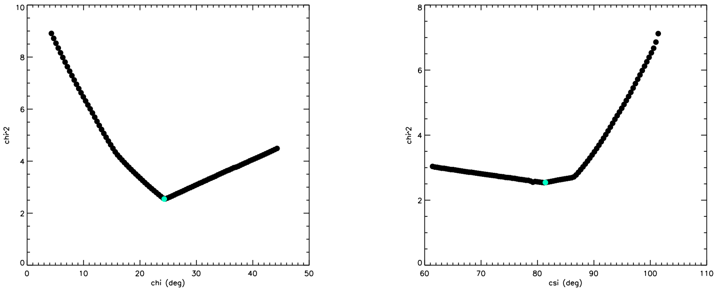

(d) χ (e) ξ

Figure B.15: *CXOU J164710.2-455216 August 2009 soft band.*

List of Figures

List of Tables

Bibliography

Albano, A., et al. 2010, submitted

Baade, W., & Zwicky, F., 1934, Proceedings of the National Accademy of Sciences of the United States of America, Volume 20, Issue 5, pp. 254

Beloborodov, A.M. 2009, ApJ, 703, 1044

Bernardini, F., et al. 2009, A&A, 498, 195

Burgay, M., et al. 2006, ATel, 903

Burwitz, V., et. al, 2003, A&A, 399, 1109

Camilo, F., et al. 2006, Nature, 442, 892

Camilo, F., et al. 2007a, ApJ, 669, 561

Campana, S., & Israel G.L. 2006, ATel, 893

Canuto, V., Lodenqyai, J., & Ruderman, M., 1971, Phys.Rev. D, 3, 2303

den Hartog, P.R., et al., 2006, A&A, 451, 587

Deneva, J.S., et al., 2008, ApJ submitted

de Vries, C.P. et al. 2004, A&A, 415, L31

Duncan R.C., & Thompson C. 1992, ApJ, 392, 9

Fahlman, G.G., & Gregory, P.C. 1981, Nature, 293, 202

Fernandez R., & Thompson C. 2007, ApJ, 660, 615

Gil, J.A., et al., 2004, A&A, 282, 45

Goldreich, P., Julian, W.H., 1969, ApJ, 157, 869

Gotthelf, E.V., et al. 2004, ApJ, 605, 368

Gotthelf, E.V., & Halpern, J.P. 2005, ApJ, 632, 1075

Gotthelf, E.V., & Halpern, J.P. 2007, Ap&SS, 308, 79

Gotthelf, E.V., & Halpern, J.P. 2008, AIPC, 983, 320

Göts, D.et al., 2006, A&A 449, 31

Greiveldinger, C., et al., 1996, ApJ, 465, 35

Haberl, F., et al. 2003, A&A, 403, L19

Haberl, F., et al. 2004a, A&A, 424, 635

Haberl, F., et al. 2006, A&A, 451, 17

Haberl, F., 2007, Isolated neutron stars: from the Interior to the surface, conference proceedengs.

Halpern, J.P., & Wang, F.Y.-H., 1997, ApJ, 477, 905

Halpern, J.P., et al. 2005, ApJ, 632, 29

Hewish, A., Bell, S.J., et al., 1968, Nature, 217, 709

Kaplan, D.L., et al. 2002, ApJ, 579, 29

Kaplan, D.L., et al. 2003, ApJ, 588, 33

Kaplan, D.L. & van Kerkwijk, M.H., 2005, ApJ, 628, 45

Kaplan, D.L. & van Kerkwijk, M.H., 2005, ApJ, 635, 65

Kaplan, D.L, et al., 2007, ApJ, 660, 1428

Kaplan, D.L. & van Kerkwijk, M.H., 2008, ApJ, 673, 163

Kaplan, D.L. & van Kerkwijk, M.H., 2009, ApJ, 692, 62

Kaplan, D.L. & van Kerkwijk, M.H., 2009, ApJ, 705, 798

Keane, E.F., et al., 2009, MNRAS submitted

Kaspi, V.M., et al., 2000, ApJ, 537, 31

Kaspi, V.M., et al., 2003, ApJ, 588, 93

Kondratiev09, V.I., et al., 2009, ApJ, 702, 692

Krimm, H., et al. 2006, GCN Circular 5581

Kuiper, L., Hermsen, W., & Mendez, M., 2004, ApJ, 613, 1173

Kulkarni, S.R., & van Kerkwijk, M.H., 1998, ApJ, 507, 49

Ibrahim, A.I., et al. 2004, ApJ, 609, 21

Israel, G.L., et al. 2004, ApJ, 603, 97

Israel, G.L., & Campana S. 2006, ATel, 896

Israel, G.L., et al. 2007, ApJ, 664, 448

Lattimer, J.M., Prakash, M., 2004, Science, 304, 536

Li, X.D., et al., 2006, ApJ, 646, 139

Lynden-Bell, D., & Boily, C., 1994, MNRAS, 267, 146

Lyutikov M., & Gavriil F.P. 2006, MNRAS, 368, 690

Malofeev, V.M., et al., 2006, Isolated Neutron Stars:From the surface to the interior, conference proceedings

Malofeev, V.M., et al., 2006, The Astronomer's Telegram, 798, 1

Mazets, E.P., Golentskii, S.V., Ilinskii, V.N., Aptekar, R.L., & Guryan, I.A. 1979, Nature, 282, 587

Mclaughlin, M.A. et al 2006, Nature, 439,817

Mclaughlin, M.A. et al 2007, ApJ, 670, 1307

Mereghetti, S., et al. 2005a, A&A, 433, 9

Mereghetti, S., et al. 2005b, ApJ, 624, 105

Mereghetti, S. 2008, A&A Review, 15, 225

Mereghetti, S., et al. 2009, ApJ, 696, 74

Molkov, S.V., 2004, Astronomy Letters, 30, 534

Morrison, R., & McCammon, D. 1983, ApJ, 270, 119

Motch, C. & Haberl, F., 1998, A&A, 333, 59

Motch, C., Zavlin, V.E. & Haberl, F., 2003, A&A, 408, 323

Motch, C., et al, 2005, A&A, 429, 257

Muno, M.P., et al. 2006, ApJ, 636, 41

Muno, M.P., et al, 2006, ATel, 902, 1M

Muno, M.P., et al, 2007, MNRAS, 378, L44

Nobili R., Turolla R., & Zane S. 2008, MNRAS, 386, 1527

Pacini, F., 1967, Nature, 216, 567

Pavlov, G.G. et al., 2002, in Neutron stars and Supernova Remnant, ASP Conf.Ser.271, pg. 274

Pavlov, G.G. et al., 2004, in Young Neutron Stars and Their Enveironments, ASP pg. 239

Perna, R., & Gotthelf, E.V. 2008, ApJ, 681, 522

Pons, J.A. et al. 2002, ApJ, 564,981

Posselt, B. et al., 2006, Isolated Neutron Stars:From the surface to the interior, conference proceedings

Rea, N., et al. 2004a, ApJ, 609, 21

Rea, N., et al. 2004b, A&A 425, 5

Rea, N., Zane, S., Turolla, R., & Lyutikov, M. 2008, ApJ, 686,1245

Rea, N., et al. 2009, ApJ, 703, 41

Reynolds, S.P., et al., 2006, ApJ, 639, 71

Schwope, A.D., et al., Isolated Neutron Stars: From the Interior to the Surface, Conference proceedings

Schwope, A.D., et al. 2009, A&A, 499,267

Thompson, C., Duncan, R., 1992, ApJ, 392, 9

Thompson, C., & Duncan, R.C. 1993, ApJ, 408,194

Thompson, C., & Duncan, R.C. 1995, MNRAS, 275, 255

Thompson, C., Duncan, R., 1996, ApJ, 473, 322

Thompson, C., Duncan, R., 2001, ApJ, 561, 980

Thompson, C., Lyutikov, M., & Kulkarni, S.R. 2002, ApJ, 274, 332

Treves, A., Turolla, R., Zane, S., & Colpi, M. 2000, PASP, 112, 297

Trümper, J. E. et al., 2004, Nuclear Physics B Proceedings Supplements, 132, 560

Van Kerkwjik, M.H. & Kaplan, D.L., 2006, Isolated Neutron Stars:From the surface to the interior, conference proceedings

Van Kerkwjik, M.H. & Kaplan, D.L., 2007, Ap&SS, 308, 191

Vink, J. et al. 2004, ApJ, 609, 75

Vink, J. et al. 2005, The Astronomer's Telegram, 650

Walter, F.M., Matthews, L.D., 1997, Nature, 389, 358

Walter, F.M., 2001, ApJ, 549, 443

Woods, P., et al., 1999, ApJ, 519, 139

Woods, P. & Thompson, C., 2004, "Compact Stellar X-ray Sources", eds. W.H.G. Lewin and M. van der Klis

Woods, P., et al., 2005, ApJ, 629, 985

Zane, S., et al. 2001, ApJ, 560, 384

Zane, S., & Turolla, R., 2006, MNRAS, 366, 727

Zane, S., et al. 2006, A&A, 457, 619

Zane, S., et al., 2008, ApJ, 682, 487

Zane, S., Rea, N., Turolla, R., & Nobili, L. 2009, MNRAS, 398, 1403

Zavlin, V.E. Pavlov, G.G., 2002, Neutron Stars, Pulsars, and Supernova Remnants, Eds. W.Becker, H. Lesch and J. Trümper, MPE-Report 278,263

Zhang, B. et al, 2006, MNRAS, 374, 1103